CHAPTER 14

Dynamic Deformation and Failure

MARC ANDRÉ MEYERS
University of California, San Diego

14.1 INTRODUCTION

The word *dynamic* appears in the title of this chapter, but does not necessarily imply high strain rates; there is a generality to the constitutive descriptions that will be given. They really apply to plastic deformation in general, if we incorporate the effects of strain rate. The reader will find a much more detailed account of dynamic deformation and failure in Kolsky [1], Freund [2], Bai and Dodd [3], and Meyers [4], among other sources. This chapter will expand on some of the points that were briefly discussed in Professor Argon's chapter (Chapter 7). The reader is also referred to the classic monograph by Kocks et al. [5], which presents the foundations of the thermodynamics and kinetics of slip.

As the rate of material deformation increases, the following effects play an increasingly important role:

1. *Mass Inertia.* This leads to the propagation of elastic, plastic, and shock waves.
2. *Thermal Inertia.* The thermal diffusion distance decreases as the time for deformation decreases, leading to pronounced temperature inhomogeneities within the material. This can lead to shear localization, which is treated in Section 14.6.
3. *Thermal Activation and Viscosity.* The response of dislocations, the primary carriers of plastic deformation, to applied tractions is determined by their ability to overcome obstacles. At lower velocities, lattice obstacles such as other atoms (Peierls–Nabarro barriers) interstitials, substitution-

Mechanics and Materials: Fundamentals and Linkages
Edited by Marc A. Meyers, Ronald W. Armstrong, and Helmut Kirchner
ISBN 0-471-24317-5

als, and forest dislocations, act as barriers. At higher propagation velocities, phonon and electron viscosity may determine the response instead. Relativistic effects on dislocations become important when their velocity approaches that of elastic waves.

The flow stress is thus dependent on temperature and strain rate. Alternative deformation mechanisms (such as twinning and phase transformations) can also play an important role.

We will not deal extensively with mass inertia in this chapter. It suffices to state Newton's conservation of momentum equation for an element of mass:

$$\frac{\partial \sigma_{ij}}{\partial x_j} = \rho \frac{\partial^2 u_i}{\partial t^2} \tag{14.1}$$

where σ_{ij} is the stress tensor and u_i is the displacement vector.

The solution of this differential equation depends on the boundary conditions and on the material constitutive response. The chapter by Rice (Chapter 3) provides some additional information. Solutions for elastic waves are given below for a uniaxial stress case [Eqs. (14.2) and (14.3)] and for the uniaxial strain case [Eq. (14.4)]; v_ℓ and v_s are longitudinal and shear wave velocities, respectively:

$$v_\ell = \left(\frac{\mathrm{E}}{\rho}\right)^{1/2} \tag{14.2}$$

$$v_s = \left(\frac{\mu}{\rho}\right)^{1/2} \tag{14.3}$$

$$v_\ell = \left(\frac{\lambda + 2\mu}{\rho}\right)^{1/2} \tag{14.4}$$

The velocities of plastic disturbances are given in terms of the slope of the stress–strain curve at the specified strain:

$$v_{p\ell} = \left(\frac{d\sigma/d\epsilon}{\rho}\right)^{1/2} \tag{14.5}$$

Shock waves, which have amplitudes significantly exceeding the flow stress and exist in a state of uniaxial strain, have propagation velocities approximately equal to elastic longitudinal wave velocity [Eq. (14.4)]. The effects of shock waves in metals are discussed in Section 14.5. The infinite complexity of the morphological characteristics of deformation and failure can be rationalized by

the interaction of these effects with the structural characteristics of materials. Prominent structural characteristics are:

Bonding: metallic, covalent, ionic
Atomic structure: crystalline, amorphous, quasi-crystalline, polymeric, and so on.
Microstructure: grain size, grain boundary structure, phase transformations, heat-treatment effects, compositional effects, and so forth.
Mesostructure: hierarchical structures, composites, synergistic systems

It is known that plastic deformation and strength of materials are a function of temperature. Figure 14.1*a* shows a plot for tantalum with temperature on the abscissa and yield stress on the ordinate [6]. As the temperature increases, there is a decrease in yield stress leading to a plateau. Similarly, as the strain rate is increased, the flow stress of tantalum increases (Fig. 14.1*b*). Tantalum is body-centered cubic (BCC); face-centered cubic (FCC) metals in general exhibit a more gradual strain rate and temperature dependence. Figure 14.1*c*, *d* shows the effects for copper, a typical FCC metal. The yield stress (at a plastic strain of 0.001) shows very low temperature dependence. The strain-rate dependence up to 10^3 s^{-1} is not significant. At this point, new deformation mechanisms and/or obstacles become operative and a marked change is observed. This will be discussed later. Researchers have tried for many years to find equations that describe this overall behavior, and to understand, from the fundamental behavior of dislocations, how this occurs. Figure 14.2 is an example of a Weertman–Ashby map. Shear strain rate is plotted on the ordinate, and homologous temperature is on the abscissa. There are several regions labeled where different phenomena are controlling plastic deformation. In Chapter 13, Professor Weertman covers high- and low-temperature creep in great detail. This chapter will focus on obstacle-controlled and drag-controlled plasticity, as well as mechanical twinning. At even higher strain rates, there are relativistic effects on dislocations, and this will also be discussed. We will not consider processes where diffusion plays a significant role.

The basic objective of researchers in the mechanical behavior of materials has been to develop an equation of the form

$$\sigma = f\left(\epsilon, \frac{d\epsilon}{dt}, T\right) \tag{14.6}$$

This equation of state (unfortunately, or fortunately for researchers!) is not possible since these are irreversible processes that are path-dependent. One has to have an equation of the form

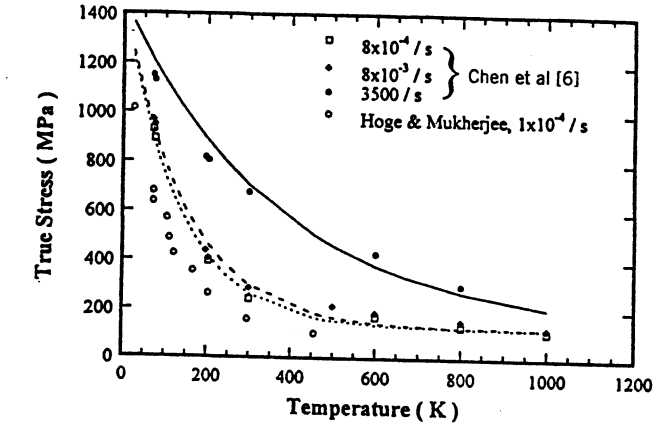

(a)

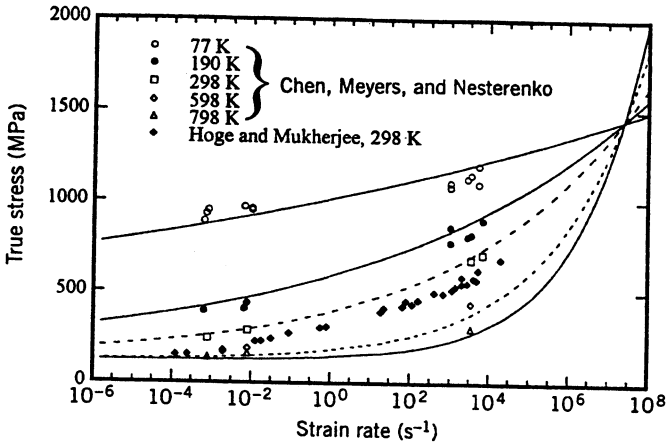

(*b*)

Figure 14.1 Variation of yield stress with (*a*) temperature for tantalum; (*b*) strain rate for tantalum (From Y. J. Chen et al. [6] and K. G. Hoge and A. K. Mukherjee, J. Matls. Sci. *12* (1977) 1666.) (*c*) temperature for copper; (*d*) strain rate for copper (from P. S. Follansbee and U. F. Kocks, Acta Met. *36* (1988) 81, p. 82.)

$$\sigma = f\left(\epsilon, \frac{d\epsilon}{dt}, T, \text{deformation history}\right) \tag{14.7}$$

The addition of deformation history represents a whole range of phenomena (including gradient terms). Throughout this chapter tensors and other complex entities will not be used. Equivalent (or effective) stresses and equivalent (or effective) strains are often used and are given by the following equation:

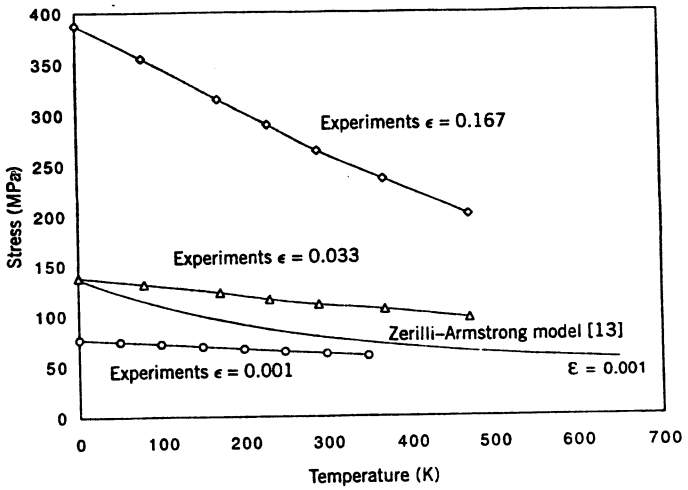

(c)

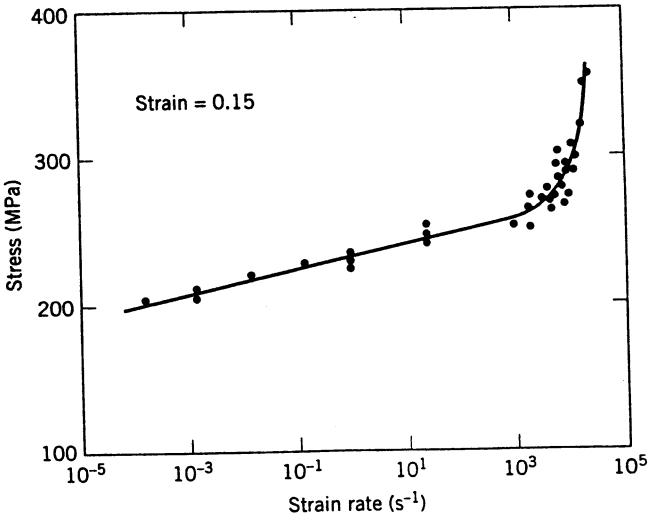

(d)

Figure 14.1 (*Continued.*)

$$\sigma_{\text{eff}} = \frac{\sqrt{2}}{2}\left[(\sigma_1 - \sigma_2)^2 + (\sigma_2 - \sigma_3)^2 + (\sigma_1 - \sigma_3)^2\right]^{1/2} \tag{14.8}$$

The equation is somewhat of a summation of the shear stresses to which a body is subjected; the terms $(\sigma_1 - \sigma_2)/2$, $(\sigma_2 - \sigma_3)/2$, and $(\sigma_1 - \sigma_3)/2$ represent shear

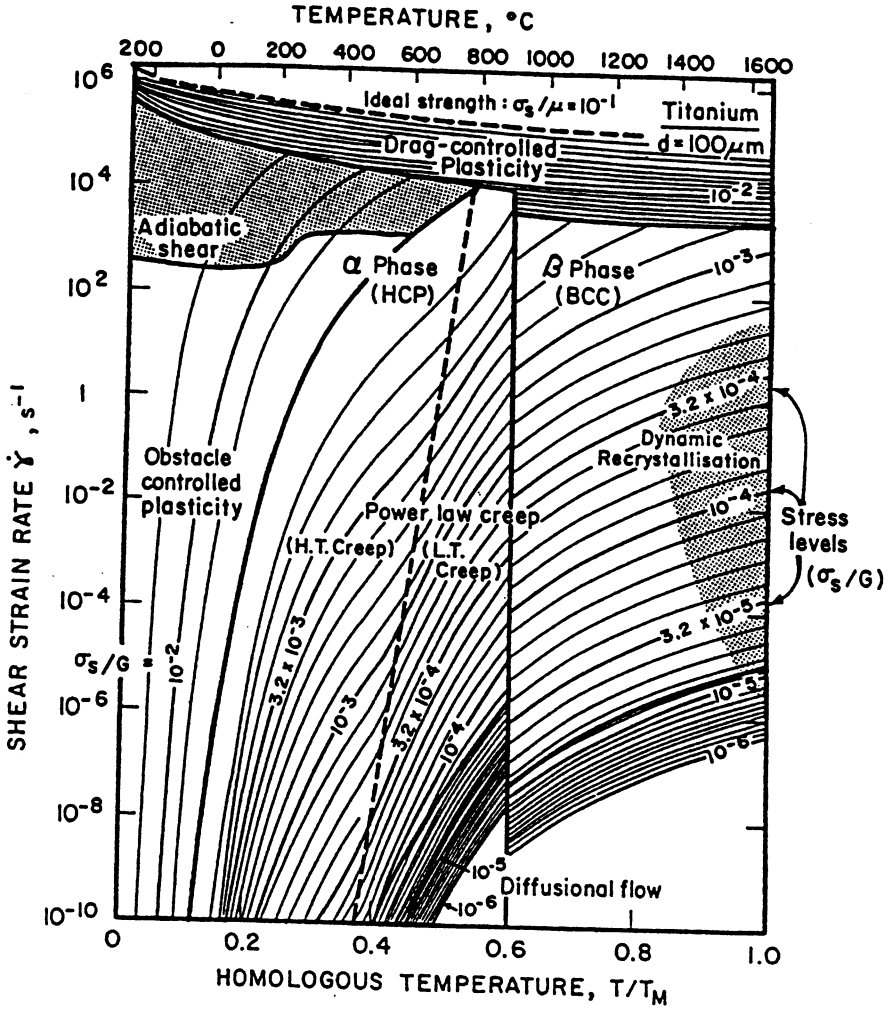

Figure 14.2 Weertman–Ashby map for titanium. (Adapted from H. J. Frost and M. F. Ashby, *Deformation Mechanism Maps*, Pergamon Press, New York, 1982, Fig. 17.4.)

stresses on three orthogonal planes. The effective shear strain to which a body is subjected is, similarly, given by

$$\epsilon_{\text{eff}} = \frac{\sqrt{2}}{3}\left[(\epsilon_1 - \epsilon_2)^2 + (\epsilon_2 - \epsilon_3)^2 + (\epsilon_1 - \epsilon_3)^2\right]^{1/2} \tag{14.9}$$

As a first approximation, the use of σ_{eff} and ϵ_{eff} enables us to reduce the complex stress–strain state to two scalars.

14.2 EMPIRICAL (ENGINEERING) CONSTITUTIVE EQUATIONS

There are many engineering correlations, that have been proposed by different investigators. These equations are very important because they are actually used in computer codes to represent material behavior. The Johnson–Cook [7] equation is the most popular, and it should be emphasized that it is a simple curve-fitting procedure. The flow stress is

$$\sigma = (\sigma_0 + B\epsilon^n)\left[1 + C\ln\frac{\dot{\epsilon}}{\dot{\epsilon}_0}\right]\left[1 - \left(\frac{T - T_r}{T_m - T_r}\right)^m\right] \tag{14.10}$$

where T_r is the reference temperature and T_m is the temperature at the melting point. In this equation the first term is the work hardening, the second term is the effect of strain rate on the flow stress, and the third term represents the effect of temperature on the flow stress. The application of the Johnson–Cook equation to iron and copper at different temperatures and strain rates is illustrated in Figure 14.3. Variants of the Johnson–Cook equation have also been used. For instance, Meyers et al. [6,8] used the following forms:

$$\sigma = (\sigma_0 + B\epsilon^n)\left[1 + C\log_{10}\frac{\dot{\epsilon}}{\dot{\epsilon}_0}\right]\left(\frac{T}{T_r}\right)^{-\lambda} \tag{14.11}$$

$$\sigma = (\sigma_0 + B\epsilon^n)\left[1 + C\log_{10}\frac{\dot{\epsilon}}{\dot{\epsilon}_0}\right]e^{-\lambda(T - T_r)} \tag{14.12}$$

These forms are easier to integrate to calculate temperature rises. In some cases, we may want to introduce a discontinuity in the yield–flow stress, to accommodate some marked change in mechanism, such as recrystallization and phase transformation. The equation may take the following form, that was suggested by Andrade et al. [9]:

$$\sigma = (\sigma_0 + B\epsilon^n)\left(1 + C\log\frac{\dot{\epsilon}}{\dot{\epsilon}_0}\right)\left[1 - \left(\frac{T - T_r}{T_m - T_r}\right)^m\right]H(T) \tag{14.13}$$

$$H(T) = \frac{1}{1 - \{1 - [(\sigma_f)_{\text{rec}}/(\sigma_f)_{\text{def}}]\}u(T)} \tag{14.14}$$

where $u(T)$ is a step function of temperature defined as

$$u(T) = \begin{cases} 0 & \text{for } T < T_c \\ 1 & \text{for } T > T_c \end{cases}$$

response. However, they do not address the more fundamental questions: How does plastic deformation take place, and how are the micromechanical processes connected to global plastic response? This will be addressed in Section 14.3.

14.3 PHYSICALLY BASED CONSTITUTIVE EQUATIONS

A material responds to external tractions by one or more of the following mechanisms:

- Dislocation generation and motion (see Chapter 9 by Veyssière)
- Mechanical twinning
- Phase transformations (mainly displacive)
- Fracture (microcracking, failure, delamination)
- Viscous glide of polymer chains and shear zones in glasses (see Chapter 7 by Argon)

We will first concentrate on dislocations, by far the most important carriers of plastic deformation in metals. In Section 14.4, we will describe mechanical twinning, which can be very important in some cases.

The most important entity responsible for plastic deformation is the dislocation. In order to have a physically based constitutive equation, it is necessary to go to the dislocation, see how it behaves, and incorporate the dislocation into a larger framework of continuum plasticity, which is then embedded into a constitutive model. As a dislocation moves, it produces a unit shear displacement b (Fig. 14.5). An assemblage of these dislocations that move on parallel planes produce a shear strain that is given by the tangent of the deflection θ (Fig. 14.5*b*). The mathematical representation of this process is very simple, and an important equation called the Orowan equation, ensues:

$$\gamma = \tan\,\theta = \frac{Nb}{\ell} = \frac{Nb\ell}{\ell^2} \tag{14.18}$$

where N = the number of dislocations
b = Burgers vector
ℓ = distance traveled by each dislocation
ρ = dislocation density

Using the fact that

$$\frac{N}{\ell^2} = \rho \tag{14.19}$$

the shear strain equation becomes

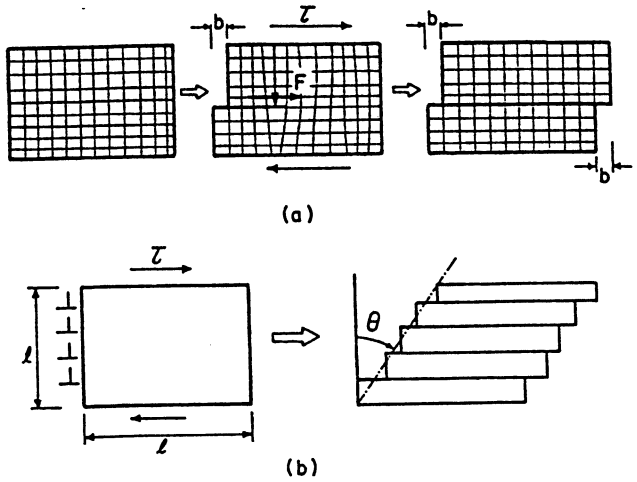

Figure 14.5 Shear produced by passage of (*a*) one dislocation; (*b*) dislocation array.

$$\gamma = \rho b l \tag{14.20}$$

The Orowan equation is one of the most important equations in micromechanics. This equation connects the movement of a dislocation l to a plastic shear strain γ that the material undergoes. In a very simple paper, Orowan [12] proposed a seminal idea that enables microstructurally based constitutive equations. In Section 14.3.1, we will see how dislocations respond to applied stresses. In Section 14.3.2 the Zerilli and Armstrong equations [13] will be given as well as an equation proposed by Klepaczko [14] and the MTS model proposed by Follansbee and Kocks [15a]. These equations share the same foundation of dislocation dynamics and are based on the seminal work of H. Becker [15b] and A. Seeger [15c]. Most of this section will be devoted to explaining how to arrive at the above-mentioned equations, which all contain a number of constants. Each of these equations has five or six parameters, and one cannot avoid this complication. These parameters will be explained in terms of fundamental dislocation motion. Nevertheless, they have to be experimentally obtained and, from an "engineering" point of view, they do not represent a dramatic advance over the simpler empirical equations given in Section 14.2.

14.3.1 Dislocation Dynamics

To start at the beginning, one must look at dislocation dynamics. Figure 14.6 presents the classic lithium fluoride results of Johnston and Gilman [16], where the applied shear stress is on the abscissa and dislocation velocity is on the ordinate. These experiments showed for the first time that as shear stress is increased from the yield stress, the dislocation velocity also increases. At the

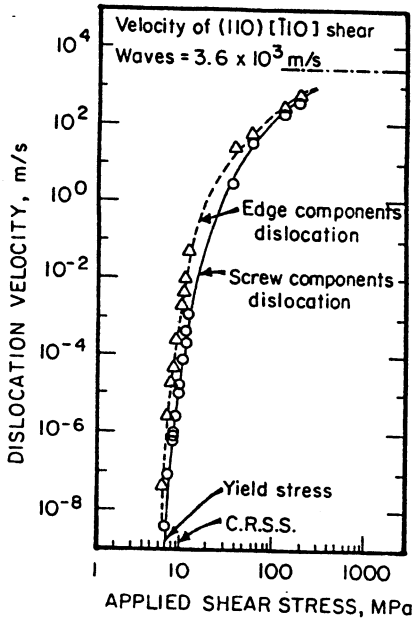

Figure 14.6 Velocity of dislocations as a function of applied stress for lithium fluoride. (Adapted from W. J. Johnston and J. J. Gilman [16], p. 132.)

top of the plot is a horizontal line representing the velocity of shear waves, which is approximately 3600 m/s [see Eq. (14.3)]. The data follow a curve that could be extrapolated to intersect the shear wave velocity at an infinite stress. After the work by Johnston and Gilman, numerous investigators studied different materials and found the same trend in their data (Fig. 14.7). This plot can then be separated into regions of low, intermediate, and high velocity. The low/intermediate cutoff is between 10^{-4} and 10^{-2} m/s, and the intermediate/high cutoff is between 10^{0} and 10^{2} m/s. It is thought that there are different mechanisms that control the movement of dislocations in the different regions. In the low-velocity region thermal activation is the dominating mechanism. The intermediate region is drag controlled, and in the high-velocity region relativistic effects play a role. These three regions will be explained in Sections 14.3.1.1, 14.3.1.2, and 14.3.1.3, respectively.

The first equation of dislocation dynamics proposed by Johnston and Gilman [16], has the form

$$v \propto \tau^m e^{-Q/kT} \tag{14.21}$$

Q is an activation energy term that provides the temperature dependence. After Johnston and Gilman, other people tried to propose different equations. Stein and Low [17] found their data to fit the equation

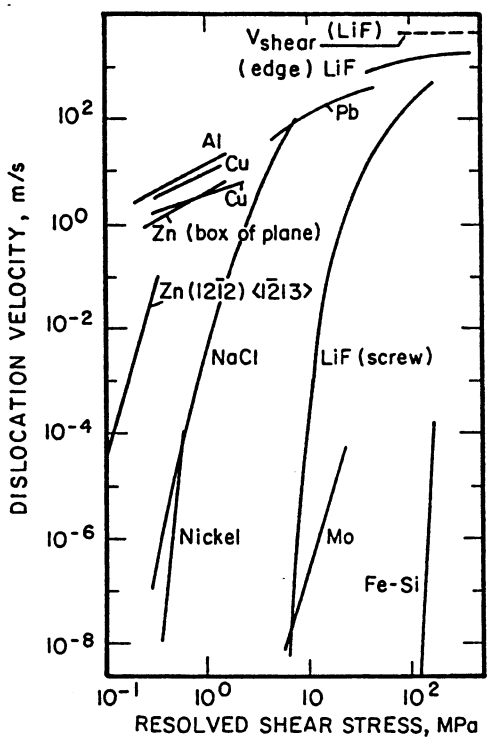

Figure 14.7 Velocity dependencies of applied stress for a number of metals.

$$v = v_0 \exp\left(-\frac{A}{\tau}\right) \tag{14.22}$$

Rohde and Pitt [18] from Utah used the following expression for iron:

$$v = \frac{kT}{h} K \exp\left(-\frac{\Delta H}{kT}\right) \exp\left[\frac{B(\tau_a - \tau_\ell)}{kT}\right] \tag{14.23}$$

which is based on Eyring's concepts of reaction rate and has both thermal and stress exponential dependencies. Then Gilman came back in his book on micromechanics [19] and stated correctly that his earlier equation predicted an infinite velocity when the stress was infinite; he proposed the following modification:

$$v = v_s^*(1 - e^{-\tau/s}) + v_d^* e^{-D/\tau} \tag{14.24}$$

This equation has a limit as the stress goes to infinity. The velocity is equal to

$$v = v_s^* + v_d^* \tag{14.25}$$

which is a more correct expression.

From the individual dislocation motion, it is possible to proceed to the Orowan equation. If one differentiates Eq. (14.20) with respect to time, the equation becomes (assuming, questionably, a constant dislocation density)

$$\dot{\gamma} = \rho b v \tag{14.26}$$

where v is the dislocation velocity. Gilman touches on these equations in Chapter 6 and discusses these aspects. If a three-dimensional analysis is used, a sum has to be taken over the different slip systems, considering their relative orientations (**m**, slip direction, and **n**, normal to slip plane) with respect to the stress axis. The plastic strain rate tensor is

$$\dot{\epsilon}^p = \sum_{k=1}^{n} \dot{\gamma}_k^p (\mathbf{m}^k \otimes \mathbf{n}^k), \tag{14.27}$$

This enters into the realm of crystal plasticity, which is discussed by Anand (Chapter 8).

A simplifying assumption regarding dislocation dynamics can be made so that there are three regions of dislocation behavior (Fig. 14.8). There is a danger of oversimplification, but it must be done in order to treat these phenomena in a somewhat systematic way. The plot is of mean dislocation velocity versus stress, and in the lower velocity region, velocity is governed by thermal activation. Drag governs velocity in the intermediate region (it should be noted that the slope between the intermediate- and high-velocity regions is equal to one). At very high velocities relativistic effects come into play, as if there were a barrier that these dislocations could not overcome (the sonic barrier).

14.3.1.1 Statistical Mechanics of Dislocation Motion†

In 1889 Arrhenius observed that there is an "activated state" intermediate between reactants and products. He suggested that the reaction rate was controlled by a rate constant k' given by

$$k' = A \exp\left(\frac{-\Delta E_e}{kT}\right) \tag{14.28}$$

where A is a frequency factor and ΔE_e is an activation energy for the process. This equation was based on van't Hoff's equation describing the effect of tem-

† From J. Wark, unpublished results.

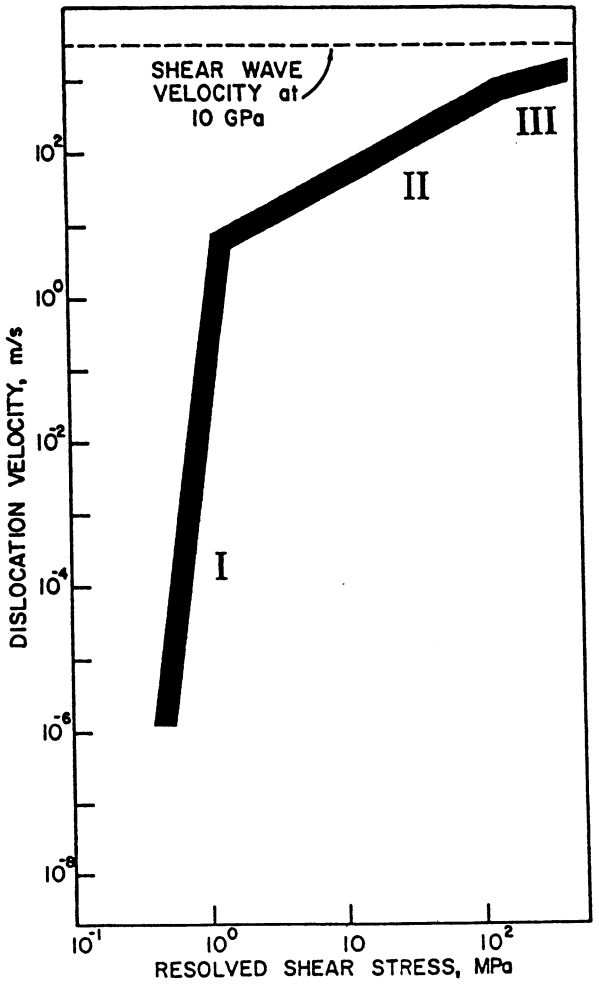

Figure 14.8 Schematic representation of three regions of dislocation behavior: I—thermal activation; II—viscous glide; III—relativistic effects.

perature on the equilibrium constant for reactions. However, the rigorous proof for this equation is rooted in statistical mechanics and in Boltzmann statistics. The movement of a dislocation requires it to pass through an "activated state." Quantum-mechanical calculations are required to calculate the exact shape of the potential-energy barriers. We will present here, in a simplified manner, how these concepts are derived. The Boltzmann law of energy distribution is the most important equation of statistical mechanics. The basic premise is that energy is quantized and that the smallest quantity is $h\nu$, where h is Planck's constant and ν is the frequency of vibration of the oscillator.

We consider N dislocations which are arrested by obstacles. Each dislocation

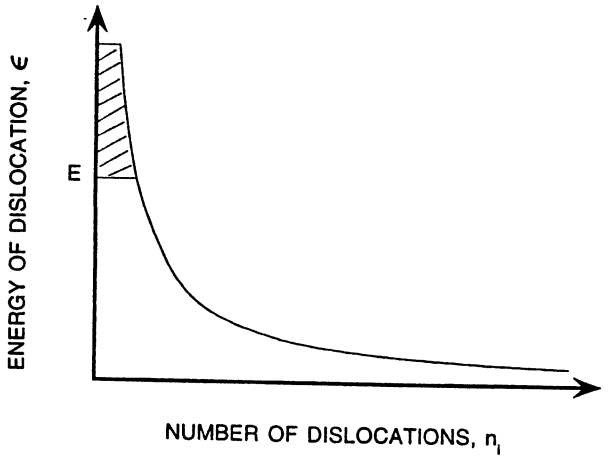

Figure 14.9 Boltzmann's distribution of energy states.

has a different energy level, and the energy levels are quantized. It can be shown that the distribution of n_i dislocations, at energy levels ϵ_i, is an exponential function that is represented in Figure 14.9 and is given by

$$n_i = Ae^{-\beta\epsilon_i} \tag{14.29}$$

This is the Boltzmann distribution. The terms A and β are parameters that express the distribution. We consider each dislocation as distinguishable.

The probability that a dislocation has an energy equal to or greater than E (the hatched region in Fig. 14.9) is given by

$$p_E = \frac{A\displaystyle\int_E^\infty e^{-\beta\epsilon_i}}{A\displaystyle\int_0^\infty e^{-\beta\epsilon_i}} = e^{-\beta E} \tag{14.30}$$

We now introduce the fundamental postulate of statistical mechanics (it is so important that Boltzmann had it engraved on his tombstone):

$$S = k \ln W \tag{14.31}$$

where S is the entropy, k is Boltzmann's constant, and W is the number of ways in which N dislocations can be arranged:

$$\frac{S}{k} = \ln \frac{N!}{n_1!n_2!n_3!n_4!\cdots} = \ln \frac{N!}{\Pi n_i!} \tag{14.32}$$

Using Stirling's approximation:

$$\ln \frac{N!}{\Pi n_i!} = \ln N! - \sum \ln n_i! = N \ln N - N - \sum n_i \ln n_i + \sum n_i \quad (14.33)$$

Since $N = \sum n_i$

$$\ln W = \frac{S}{k} = N \ln N - \sum n_i \ln n_i \quad (14.34)$$

But

$$n_i = Ae^{-\beta \epsilon_i} \quad (14.35)$$

$$N = \sum n_i = A \sum_i e^{-\beta \epsilon_i} \quad (14.36)$$

$$\ln n_i = \ln A + \ln e^{-\beta \epsilon_i}$$

$$n_i \ln n_i = Ae^{-\beta \epsilon_i}(\ln A - \beta \epsilon_i) \quad (14.37)$$

$$S = k\left[N \ln N - \sum n_i(\ln A - \beta \epsilon_i\right]$$

$$= k\left(N \ln N - N \ln A + \beta \sum n_i \epsilon_i\right) \quad (14.38)$$

Furthermore

$$\sum n_i \epsilon_i = U \quad (14.39)$$

$$S = k[N(\ln N - \ln A) + \beta U]$$

$$= k\left[N\left(\ln A - \ln A + \ln \sum_i e^{-\beta \epsilon_i}\right) + \beta U\right]$$

$$= k\left[N \ln \sum_i e^{-\beta \epsilon_i} + \beta U\right] \quad (14.40)$$

We will now establish the value of k. From the first law of thermodynamics

$$dU = T\,dS - P\,dV \tag{14.41}$$

$$\left(\frac{\partial U}{\partial S}\right)_V = T \tag{14.42}$$

$$\left(\frac{\partial S}{\partial U}\right)_V = \frac{1}{T} \tag{14.43}$$

We can make

$$\left(\frac{\partial S}{\partial U}\right)_V = \left(\frac{\partial S}{\partial \beta}\right)\left(\frac{\partial \beta}{\partial U}\right) = \frac{1}{T} \tag{14.44}$$

$$\frac{\partial S}{\partial \beta} = k\left(\frac{-N\sum_i \epsilon_i e^{-\beta\epsilon_i}}{\sum_i e^{-\beta\epsilon_i}} + \sum n_i\epsilon_i - \beta\sum_i n_i\epsilon_i^2\right) \tag{14.45}$$

$$\frac{\partial U}{\partial \beta} = -\sum_i n_i\epsilon_i^2 \tag{14.46}$$

Inserting (14.45) and (14.46) into (14.44)

$$\frac{\partial S}{\partial U} = k\left(-U + U - \beta\sum_i n_i\epsilon_i^2\right)\frac{1}{-\sum_i n_i\epsilon_i^2} = k\beta = \frac{1}{T} \tag{14.47}$$

Hence $\beta = 1/kT$.

Substituting this into Eq. (14.30), we obtain

$$p_E = Ae^{-E/kT} \tag{14.48}$$

The probability that a dislocation has an energy greater than E is equal to this expression. We assume that the dislocation will overcome the obstacle when its energy exceeds the height of the obstacle, E. With this expression under our belt and well understood, we can now proceed. We usually use ΔG to represent the Gibbs free energy.

14.3.1.2 Thermally Activated Motion of Dislocations

First thermal activation will be discussed. Equation (14.49) (derived in Section 14.3.1.1) is embedded in many of the important phenomena in materials science:

$$p = \exp\left(-\frac{\Delta G}{\kappa T}\right) \tag{14.49}$$

where p is the probability that a dislocation will overcome a barrier, k is Boltzmann's constant, and ΔG is the activation energy for the process. All the modern constitutive equations are really based on this expression. Basically, it says that, given a barrier of a height ΔG, the probability that an entity (in our case, a dislocation) will jump over the barrier is p. As the temperature goes up, the probability increases because thermal energy will provide the "kick" that allows the entity to jump over the barrier. The frequency of successful jumps is related to the probability by ($p = \nu_1/\nu_0$)

$$\nu_1 = \nu_0 \exp\left(-\frac{\Delta G}{\kappa T}\right) \tag{14.50}$$

Kocks et al. [5] authored a classic paper or thermally activated dislocation motion. They have the following expression for the frequency of vibration of a dislocation of length ℓ:

$$\nu_0 = \frac{\nu b}{4\ell} \tag{14.51}$$

where ν is the frequency of vibration of an atom. One can see that it is similar to the vibration of a string, where frequency depends on string length. Atoms vibrate at about 10^{13} per second (s^{-1}). Since the dislocation is longer, it will vibrate at a much lower frequency, and the actual frequency depends on the length of the dislocation. For $\ell = 250b$, a reasonable value for deformed metals, $\nu \approx 10^{10}\ s^{-1}$. The dislocation spacing ℓ_s can be related to the density ρ:

$$\ell_s \cong \rho^{-(1/2)} \tag{14.52}$$

The average time a dislocation takes to move from one barrier to another can be divided into a waiting time and a running time. A dislocation encounters many different types of barriers (Fig. 14.10). There are smaller barriers such as vacancies, substitutional atoms, and small-angle grain boundaries. There are also big barriers like precipitates, inclusions, voids, and other dislocations. These barriers are usually divided into two classes. The smallest one of the barriers is the atom itself because as the dislocation moves, individual atoms switch positions. These are called *Peierls–Nabarro barriers*, which are shown in Figure 14.11. The dislocation in Figure 14.11 (1) will move to the next location, in Figure 14.11 (3), but in order to do that it has to overcome the barrier in Figure 14.11 (2). The plot shows force versus distance for the movement of a dislocation. The

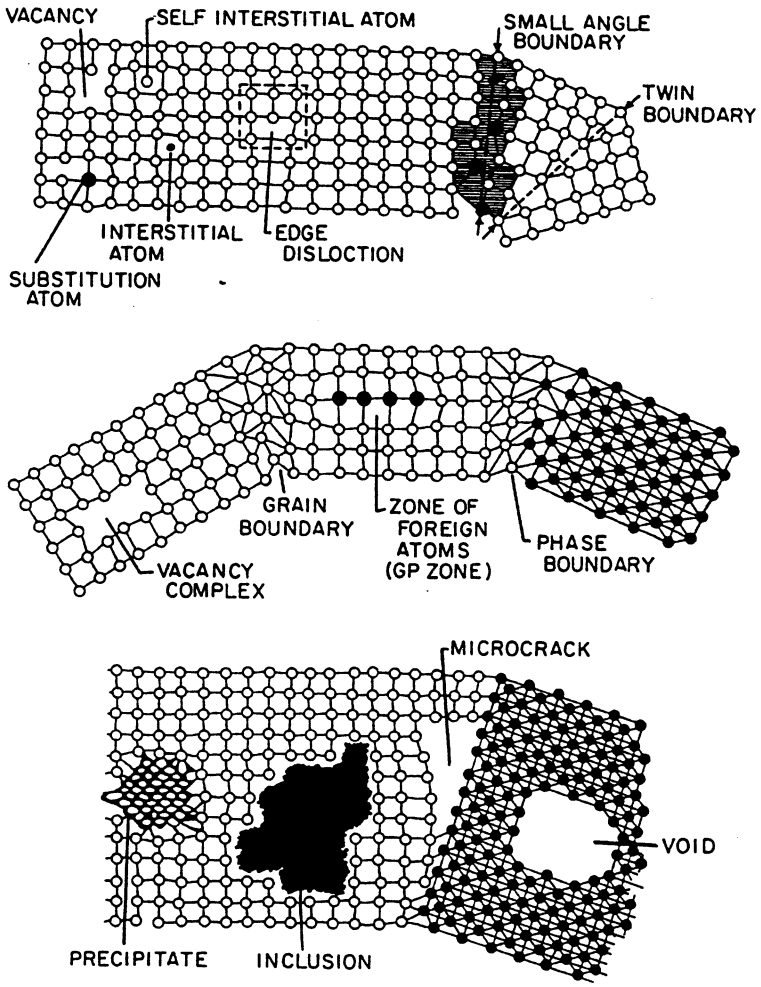

Figure 14.10 Schematic representation of lattice obstacles to dislocation motion. (Adapted from O. Vöhringer, private classnotes.)

force that must be applied on a dislocation first goes up and then goes down. The value of the peak is the Peierls–Nabarro stress, and it is more complicated than it looks. The dislocation does not move forward as a rigid rod; rather, a kink having dimensions of b is formed, and the two sides move parallel to the dislocation line. This is called the Seeger kink-pair mechanism and is shown in schematic fashion in Figure 14.12. The individual kink velocity is v_k, whereas the forward velocity of the dislocation is v_D. In Chapter 6 Gilman describes how the Peierls–Nabarro stress varies from material to material.

The biggest barrier would be an inclusion or a void. And again we are going to make a number of assumptions. One intermediate barrier (a dislocation) is

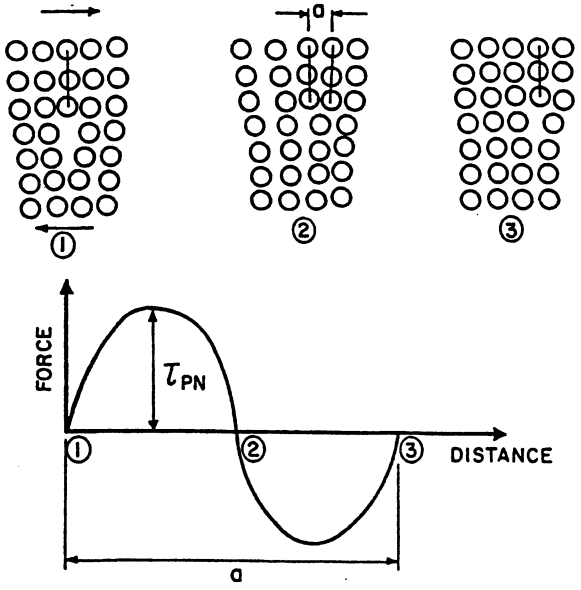

Figure 14.11 Periodic Peierls–Nabarro stress encountered by dislocation.

shown in Figure 14.13. This is called a "forest" because the barrier dislocations are standing up and the moving dislocation is slicing right through the "tree" dislocations. As it cuts through them, it creates kinks and jogs that slow it down. All of these barriers can be put into an analytical framework and defined by an equation that relates the strain rate to the stress. We shall do this next.

When a dislocation is traveling as shown in Figure 14.13, it will run very fast until it hits the first forest barrier. It runs again, hits the next barrier, and

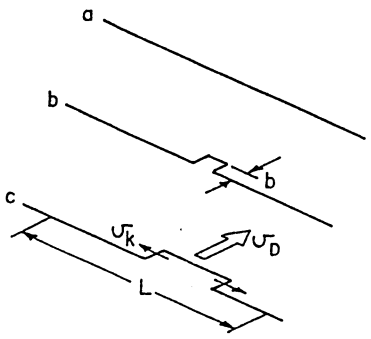

Figure 14.12 Overcoming of Peierls barrier by Seeger kink-pair mechanism: (*a*) original straight dislocation; (*b*) dislocation with two kinks: (*c*) kinks moving apart at velocity v_k.

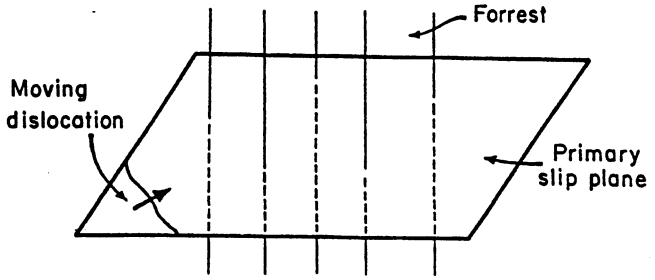

Figure 14.13 "Forest" of dislocations that act as barriers to moving dislocation.

so on. Figure 14.14 is a plot of time versus distance at a certain stress level for such a scenario. At the stress level σ_1 the dislocation will run, and then come to a barrier. Many attempts will be made before it makes it over and then the process continues. An average dislocation velocity is obtained based on this stop and start sequence. If the stress is increased, the dislocation is aided in its jump and the waiting time t_w is decreased. This is indicated by σ_2 in Figure 14.14.

The equations that express these ideas start with

$$\Delta t = t_r + t_w \tag{14.53}$$

where t_r is the running time and t_w is the waiting time. One can neglect the running time by saying the dislocation runs $t_r \ll t_w$. The analogy is La Jolla (CA) traffic. The waiting time at the traffic lights greatly exceeds the driving time, and the total travel time can be approximated as the average time at lights multiplied by the number of lights. The equation for the waiting time is

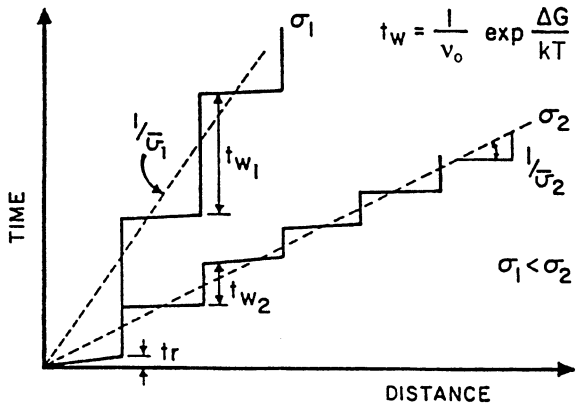

Figure 14.14 Schematic representation of dislocation motion at two stress levels; notice stop–go sequence.

$$t_w = \frac{1}{\nu_1} \tag{14.54}$$

and by substituting Eq. (14.50) for ν_1 the waiting time becomes

$$t_w = \frac{1}{\nu_0} \exp\left(\frac{\Delta G}{\kappa T}\right) \tag{14.55}$$

The Orowan equation [Eq. (14.26) with an orientation factor M] can now be applied to relate the strain to the movement of the dislocations. The result is

$$\frac{d\gamma}{dt} = \frac{\Delta\gamma}{\Delta t} = \frac{1}{M} \rho b \frac{\Delta \ell}{\Delta t} \tag{14.56}$$

When Eq. (14.55) is substituted, the strain rate becomes

$$\frac{d\gamma}{dt} = \frac{\nu_0 \rho b \, \Delta \ell}{M} \exp\left[-\frac{\Delta G}{\kappa T}\right] \tag{14.57}$$

where ν_0 = frequency of vibration of the dislocation
ρ = dislocation density
b = Burgers vector
$\Delta \ell$ = distance between dislocation barriers
M = orientation parameter

The terms before the exponential term can be grouped together and called $\dot{\gamma}_0$:

$$\dot{\gamma} = \dot{\gamma}_0 \exp\left[-\frac{\Delta G}{\kappa T}\right] \tag{14.58}$$

By solving for ΔG, one can obtain the equation

$$\Delta G = kT \ln \frac{\dot{\gamma}_0}{\dot{\gamma}} \tag{14.59a}$$

We have to introduce the stress now. It comes in through the height of the barriers. Figure 14.15 shows a schematic view of these obstacles. As the dislocation moves along the abscissa axis, it passes over schematic little protruding barriers as it climbs up the large one. The obstacles can be divided into long-range obstacles (big hill) and short-range obstacles (little "pimples"). This is

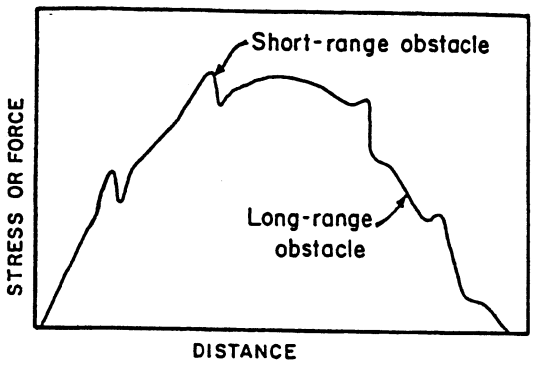

Figure 14.15 Different barriers encountered by dislocation as it moves.

a simplification of reality in order to make analysis easier. The stress can be separated into two components: a temperature-independent stress, σ_G; and a temperature-dependent, or effective stress, σ^* [not to be confused with σ_{eff} in Eq. (14.8)].†

$$\sigma = \sigma_G + \sigma^* \tag{14.59b}$$

Figure 14.16 shows a general barrier configuration. These are short-range barriers because thermal activation can aid dislocations in overcoming them. The barrier is shown at various temperatures; as the temperature increases, thermal energy (the hatched portion) is increasingly provided and the effective barrier height decreases. The total energy of the barrier is the area under the barrier curve; at T_0 it is ΔG_0. As the temperature increases, the thermal energy increases so that the effective energy barrier at T_1 is

$$\Delta G = \Delta G_0 - \Delta G_1 \tag{14.60}$$

Now, how can this be expressed analytically? By integrating over the total barrier height, an expression is obtained for the energy. The barrier height, ΔG, is equal to

$$\Delta G = \Delta G_0 - \int_{F_i}^{F_0} \lambda(F)\, dF \tag{14.61}$$

in which ΔG_0 is the activation energy at 0 K and $\lambda(F)$ is the barrier width; F_i has values of F_1, F_2, and F_3, at T_1, T_2, and T_3, respectively. This equation can

† This concept was introduced by Seeger [15c]; a detailed thermodynamic theory was developed by Conrad and Wiedersich [15d].

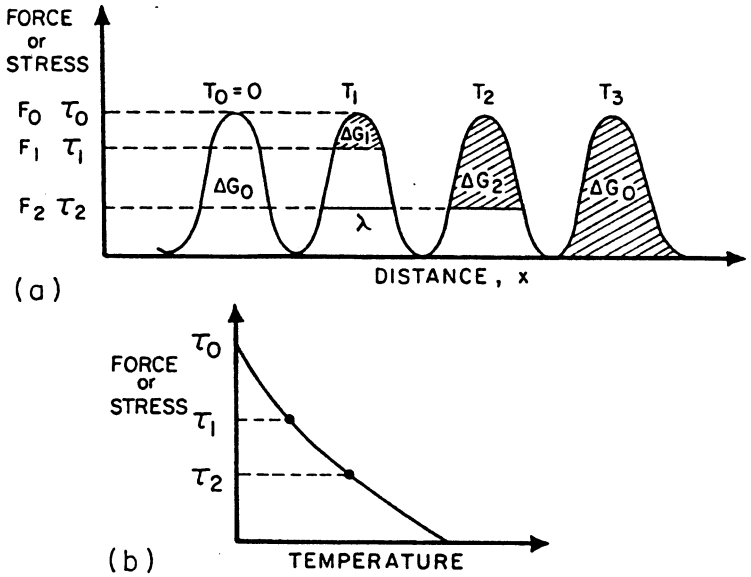

Figure 14.16 (*a*) Representation of thermal assistance to the overcoming of obstacles; (*b*) Effect of temperature on stress required to move dislocations.

be set equal Eq. (14.59a) to get

$$kT \ln \frac{\dot{\gamma}_0}{\dot{\gamma}} = \Delta G_0 - \int_{F_i}^{F_0} \lambda(F)\, dF \tag{14.62}$$

The height of the hatched area is $F_0 - F_i$, which is a function of T. At T_1, $F^* = F_0 - F_1$. In this equation F refers to the forces acting on the dislocation. These forces per unit length can be expressed in terms of the applied stress, by using the Peach–Kochler equation (see Chapter 9 by Veyssière):

$$F = \tau b \tag{14.63}$$

in which τ is the shear stress and b is the Burgers vector. This equation can be inserted into Eq. (14.62) to obtain a relation between stress, strain rate, and temperature. The procedure for this begins with the force equation. To this force equation a length term must be added

$$F = \tau b \ell^* \tag{14.64}$$

and the ℓ^* is equal to the distance between barriers. Figure 14.17 explains the reason for adding this extra term to the equation. These barriers can be consid-

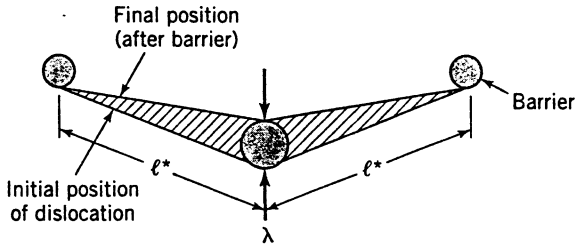

Figure 14.17 Dislocation overcoming obstacles; two positions shown.

ered a forest of dislocations or point defects and the force acts along the entire dislocation line. Substituting Eq. (14.64) we have

$$\int_{F_i}^{F_0} \lambda(F)\, dF = \int_{\tau_i}^{\tau_0} \lambda(\tau) b\ell^*\, d\tau = b\ell^* \int_{\tau_i}^{\tau_0} \lambda(\tau) d\tau \tag{14.65}$$

where F_i and τ_i represent the values at the bottom of the hatched area in Figure 14.16. The only part that has not been defined so far is λ. It depends on the type of barrier that is assumed. Figure 14.18a shows three different types of barriers that could be assumed; each leads to a different corresponding constitutive equation. We can also define $\tau^* = \tau_0 - \tau_i$. For a rectangular barrier, λ is constant so the integral becomes

$$b\ell^*\lambda \int_{\tau_i}^{\tau_0} d\tau = b\ell^*\lambda(\tau_0 - \tau_i) = V\tau^* \tag{14.66}$$

The variable V is the activation volume of the barrier, defined as

$$V = Ab \tag{14.67}$$

where A is the activation area. It is the area swept by a dislocation from the time it enters the obstacle to the position where it is past the obstacle (see Fig. 14.17, hatched area). This area is thus related to the width of the obstacle λ and the distance between the obstacles ℓ^*. As an approximation

$$A \approx \lambda \ell^* \tag{14.68}$$

Figure 14.18*a* shows that the base stress level is τ_G; so τ^* can be written as $(\tau - \tau_G)$ and $\sigma^* = \sigma - \sigma_G$. This can be substituted back into Eqs. (14.62), (14.66), and (14.65) to get

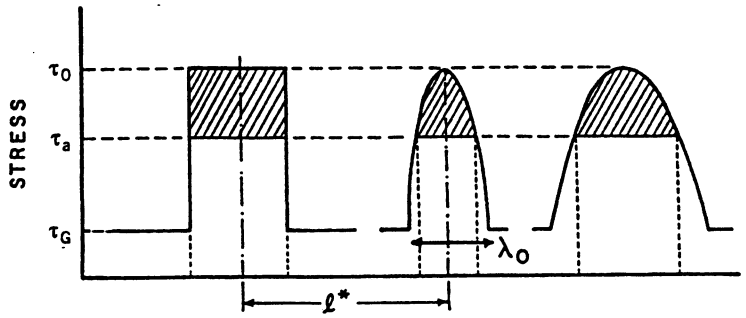

(*a*)

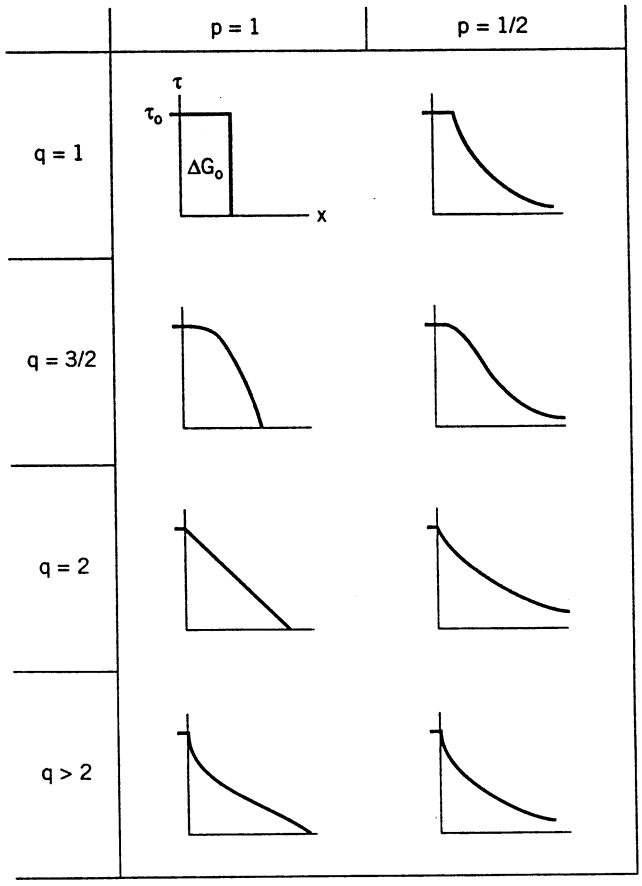

(*b*)

Figure 14.18 (*a*) Different idealized shapes of obstacles. (*b*) different obstacle shapes and corresponding values of p and q (Adapted from Kocks et al. [5]).

$$kT \ln \frac{\dot{\gamma}_0}{\dot{\gamma}} = \Delta G_0 - V(\tau - \tau_G) \tag{14.69}$$

The constitutive equation can be obtained by solving for σ to obtain

$$\tau = \tau_G + \frac{\Delta G_0}{V} + \frac{kT}{V} \ln \frac{\dot{\gamma}}{\dot{\gamma}_0} \tag{14.70}$$

In Eq. (14.70) the stress has been represented as a function of temperature and strain rate based only on fundamental parameters. This was the original form proposed by Seeger [15c]; it predicts a linear decrease of σ with T, because of the rectangular barriers. He later used a more general, exponential barrier form [164, 165]. In 1968, Ono [166] compared different shapes of the barrier: square, triangle, parabola, exponential, sine.

Remember that there are different barrier shapes that can be considered and one would assume that different shapes would give different constitutive equations. Kocks et al. [5] proposed a generalized equation for these shapes with two parameters, p and q. They said that their equation could fit any shape. Their equation is of the form (note that we switched from shear stresses to normal stresses for convenience):

$$\Delta G = \Delta G_0 \left[1 - \left(\frac{\sigma}{\sigma_0} \right)^p \right]^q \tag{14.71}$$

Professor Argon mentions these equations briefly in Chapter 7; hence they should look familiar to the attentive student. The generalized constitutive equation has the form (note that we switched from shear strains to longitudinal strains)

$$kT \ln \frac{\dot{\epsilon}_0}{\dot{\epsilon}} = \Delta G_0 \left[1 - \left(\frac{\sigma}{\sigma_0} \right)^p \right]^q \tag{14.72}$$

based on the physical processes of slip occurring in the material. Figure 14.18*b* shows the various shapes of barriers considered by Kocks et al. [5] and the respective values of p and q. These values also determine the yield stress versus temperature behavior. Follansbee and Kocks [15] found the best fit, for BCC materials, for $p = \frac{1}{2}$ and $q = \frac{3}{2}$. Ono [166] and Kocks et al. [5] state that this is the best fit for most cases. Meyer [20] presents a tabulation of the best values for p and q.

It is possible to make a qualitative illustration of the strain-rate and temperature dependence of the flow stress of a metal by considering both long-range (athermal) and short-range (thermal) barriers, and an effective and athermal

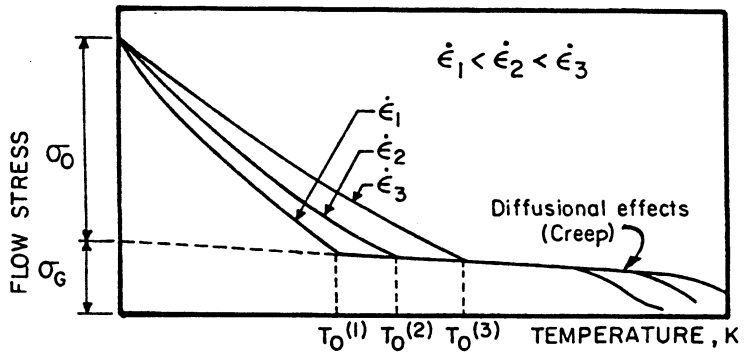

Figure 14.19 Thermal (σ_0) and athermal (σ_G) components of stress and their effect on temperature and strain-rate dependence of flow stress.

component of flow stress, given by Eq. (14.38). The athermal portion of the flow stress shows a very small temperature dependence, equal to that of the elastic constants (e.g., G); this is seen in Figure 14.19. The effective stress, governed by an equation like Equation (14.72), shows a much more drastic dependence.

14.3.1.3 Drag-Controlled Dislocation Motion

As the velocity of dislocation increases, different mechanisms slow down its motion. At the intermediate velocities of Figure 14.8, a region exists that has a slope of one on the log–log plot. This is called the *drag regime*, where Newtonian viscous behavior is assumed, and can be expressed as

$$F = Bv \tag{14.73}$$

Then F is transformed into τb and

$$\tau b = Bv \tag{14.74}$$

Using the Orowan equation (Eq. 14.26), with an orientation factor M_i

$$\tau b = \frac{BM\dot{\gamma}}{\rho b} \tag{14.75}$$

and the values

$$\tau = \frac{\sigma}{2} \quad \text{and} \quad \gamma = 2\epsilon \tag{14.76}$$

the constitutive equation is found to be

$$\sigma = \frac{4BM}{\rho b^2}\,\dot{\epsilon} \tag{14.77}$$

The viscosity coefficient B has been characterized in different forms, and a common one is

$$B = \frac{B_0}{1 - (v^2/v_s^2)} \tag{14.78}$$

Hirth and Lothe [33] use the form

$$B = \frac{bw}{10v_\ell} \tag{14.79}$$

where v_ℓ is the velocity of an elastic wave and $w = 3kT/a^3$. Depending on the temperature, there are two different drag mechanisms that can affect a system. Parameswaran and Weertman [21] performed experiments in which they measured the damping constant B as a function of temperature for aluminum (Fig. 14.20). At very low temperatures, electron viscosity seems to be doing the damping. At higher temperatures, phonons are prominent because the vibration amplitude of the atoms becomes very important and phonon damping is the prominent mechanism.

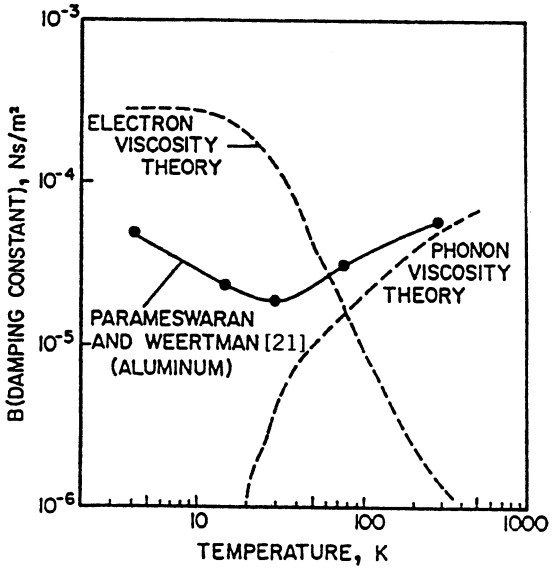

Figure 14.20 Contributions of electrons and phonons to total viscosity. [Adapted from Parameswaran, N. Urabe, and J. Weertman, J. A. P. *43* (1972), 2982.]

14.3.1.4 *Relativistic Effects*

Relativistic effects, originally proposed by Frank [167], occur when the sound velocity is approached. No derivations will be carried out here, but the result for the total dislocation energy is†

$$U_T = U_p + U_k = \frac{U_0}{\beta} \tag{14.80}$$

and both the potential energy and the kinetic energy increase with the velocity of the dislocation. The potential-energy term looks like

$$U_p = \frac{Gb^2}{4\pi} \ln\left(\frac{R}{r_0}\right) \frac{1+\beta^2}{2\beta} \tag{14.81}$$

which is taken from the work of Weertman [22]. In this expression β is equal to

$$\beta = \left(1 - \frac{v^2}{v_s^2}\right)^{1/2} \tag{14.82}$$

As the shear wave velocity is approached (v_s is the shear wave velocity), β approaches zero, and the total energy goes to infinity. The stress σ_{23} around an edge dislocation is shown in Figure 14.21. Figure 14.21*a* represents σ_{23} at rest. As the dislocation accelerates, the stress field is compressed, and the energy of the dislocation goes to infinity. Figure 14.21*b* shows the stress field for v/v_s = 0.5; Figure 14.21*c* shows v/v_s = 0.995. This explains why the dislocation does not want to travel at the sound velocity. The energy of the dislocation between 0.8 and 0.9 goes up as we approach v_s. This is seen in Figure 14.22; of the shear wave velocity, the effects are very unimportant, but between 0.8 and 0.9, it kicks up. We need an infinite amount of energy to drive a dislocation at those velocities. This represents the region of relativistic effects. There have been suggestions by Weertman [22] of supersonic ($v > v_l$) and transonic ($v_s < v < v_l$) dislocations.

14.3.2 The Zerilli–Armstrong Equation

Zerilli and Armstrong [13,23] proposed two microstructurally based constitutive equations that show an excellent match with experimental results. They based their model on the framework of thermally activated dislocation motion described in Section 14.3.1. They analyzed the temperature and strain-rate response of typical FCC and BCC metals and noticed a significant difference between these materials. The BCC metals exhibit a much higher temperature and strain-rate sensitivity than the FCC metals (see Fig. 14.1).

† A very comprehensive treatment is given by Weertman and Weertman [170].

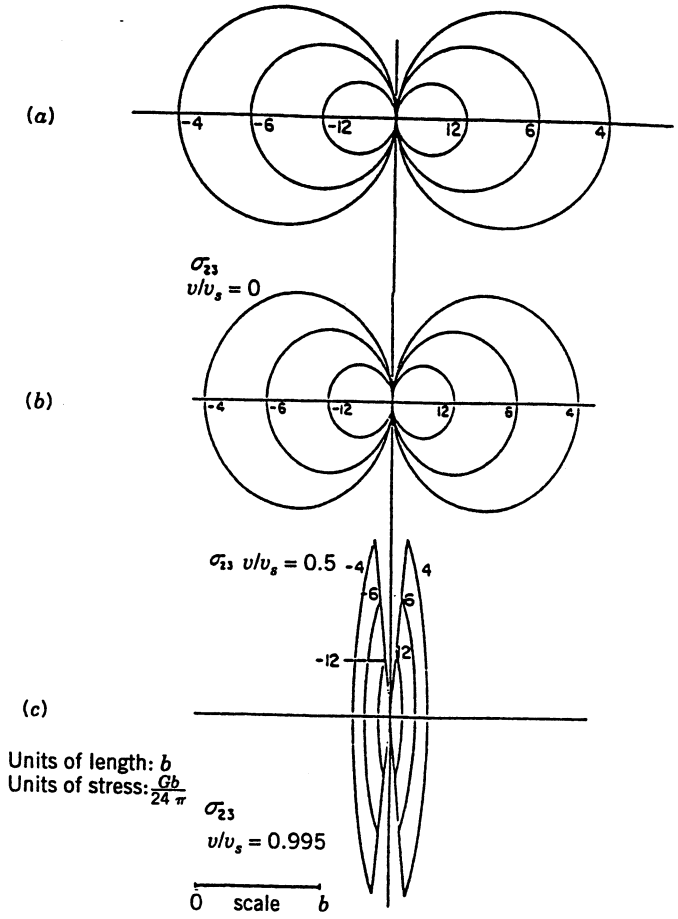

Figure 14.21 Effect of velocity on stress field (of σ_{23}) of edge dislocation; (*a*) $v/v_s = 0$; (*b*) $v/v_s = 0.5$; (*c*) $v/v_s = 0.995$.

Zerilli and Armstrong [13,23] noticed that the activation area (which represents the area swept by the dislocation from the beginning of the obstacle to the end of the obstacle) varies in FCC materials in some fashion, while for BCC materials it is constant. What does this mean? In BCC metals, the Peierls–Nabarro stresses determine the flow stress. For FCC materials, the forest dislocations are the rate controlling mechanism. The dislocation density increases with plastic deformation and therefore the activation area (related to the spacing between forest dislocations) decreases. They separated the behavior of FCC materials from the behavior of BCC materials, and were able to come to rather simple constitutive equations that incorporate these differences. Typical BCC metals are iron, tungsten, molybdenum, nobium, and tantalum, which have strong temperature and strain-rate dependence. Typical FCC metals are

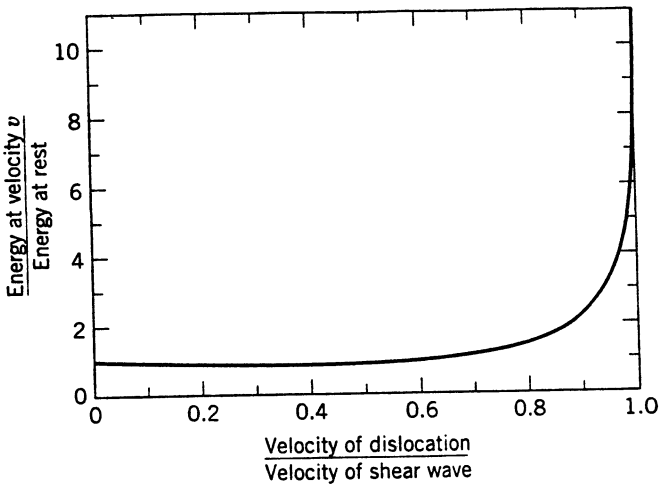

Figure 14.22 Effect of velocity on dislocation self-energy.

copper, gold, and aluminum, which have a low temperature dependence of the flow stress, and a low strain-rate dependence. The activation area is given by [see Eq. (14.68)]

$$A_A = \lambda \ell^* \tag{14.83}$$

We know that the barriers are the dislocations, for FCC metals. If we have dislocations barriers with spacing ℓ^*, they are related to the dislocation density by [24] [see Eq. (14.52)]

$$\rho \cong \frac{1}{\ell^{*2}} \tag{14.84}$$

From the Orowan equation [see Eq. (14.20)]

$$\epsilon = \frac{1}{M} \rho b \ell$$

If l is assumed constant (a rather drastic hypothesis), then

$$\rho = \frac{M\epsilon}{b\ell}$$

Hence

$$A = \lambda \ell^* = \lambda \left(\frac{b\ell}{M} \right)^{1/2} \epsilon^{-1/2}$$

We end up with this constitutive equation for FCC metals:

$$\sigma^* = C_2 \epsilon^{1/2} \exp(-C_3 T + C_4 T \ln \dot{\epsilon}) \tag{14.85}$$

Equation 14.85 contains terms that account for work hardening, temperature, and strain-rate effects. This is only for the thermal portion of the flow stress. The total flow stress is equal to the thermal portion, which is given above, plus the athermal portion, and the grain size effect (Hall–Petch equation, where D is the grain size):

$$\sigma = \sigma_G + \sigma^* + kD^{-1/2} \tag{14.86}$$

For the BCC, Zerilli and Armstrong [13] assumed that the activation area was constant because the area swept by overcoming the Peierls–Nabarro barriers is independent of strain. The distance between the atoms does not change. Then one arrives at this equation, for BCC metals:

$$\sigma^* = C_1 \exp(-C_3 T + C_4 T \ln \dot{\epsilon}) \tag{14.87}$$

and

$$\sigma = \sigma_G + C_1 \exp(-C_3 T + C_4 T \ln \dot{\epsilon}) + C_5 \epsilon^n + kD^{-1/2}$$

Figure 14.23 shows Zerilli–Armstrong predictions for copper and iron, prototypical FCC and BCC metals, respectively. The higher strain-rate and temperature dependence of the BCC structure are evident in the plots. These plots were generated from parameters provided by Zerilli and Armstrong [13]. It should be noted that we still need to experimentally obtain C_1, C_2, C_3, C_4, and C_5. Hence, the constitutive equation is still rooted in experiments. Notable differences between $J - C$ and $Z - A$ are:

1. $J - C$ assumes a linear increase in flow stress with the logarithm of strain rate. We have direct and ample experimental evidence showing that this is not correct; at strain rates of 10^3 s^{-1} and above (especially for BCC metals) substantial deviations occur.
2. The different effects (work hardening, strain-rate hardening, and thermal softening) are multiplied by each other in $J - C$, whereas they are additive in $Z - A$. BCC metals, where the stress–strain curves are translated upward and downard by temperature and strain rate changes are better represented by the $Z - A$ constitutive equation.

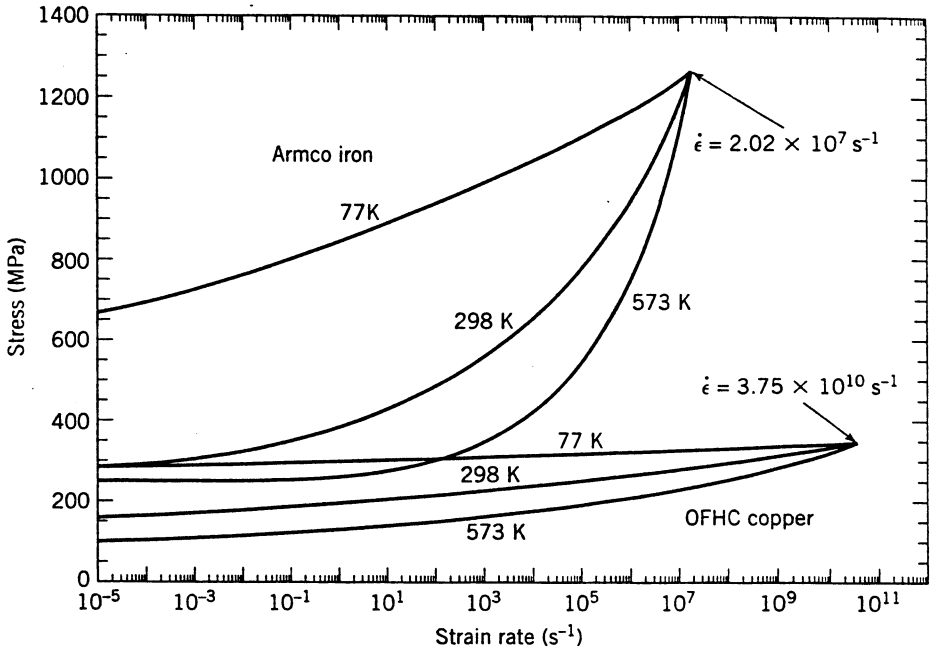

Figure 14.23 Zerilli–Armstrong prediction of temperature and strain-rate dependence of typical BCC (Armco iron) and FCC (copper) metals.

14.3.3 The Mechanical Threshold Stress Model

Another model that is commonly used, is the one developed by the group at Los Alamos; it is called the mechanical threshold stress (MTS) model. This shape of the barrier is determined by p and q that Kocks et al. [5] used to describe for a general barrier. The MTS model often uses p equal to $\frac{1}{2}$ and q is equal to $\frac{3}{2}$, since this provides a good fit to the experimental results for many metals.

$$\left(\frac{\sigma}{G(T)}\right)^p = \left(\frac{\sigma_0}{G(T)}\right)^p \left[1 - \left(\frac{kT}{Gb^3 g_0} \ln \frac{\dot{\epsilon}_0}{\dot{\epsilon}}\right)^{1/q}\right] \tag{14.88}$$

where we have the stress divided by the shear modulus, which is temperature-dependent. T is the temperature; g_0 is a normalized form of ΔG_0; and σ_0 is the threshold stress, which is the stress required to plastically deform a material at zero degrees Kelvin (in the absence of thermal activation).

We must discuss an additional complication now. If there were no strain-rate dependence of work hardening, we would have the situation depicted in Figure 14.24*a*. The flow stress, at a fixed strain γ_T, is a function of the strain rate only. If a test is carried out up to A at $\dot{\gamma}_1$, and the strain rate is changed to $\dot{\gamma}_2$, the flow curve will follow path BC, which is characteristic of $\dot{\gamma}_2$. A return to $\dot{\gamma}_1$

will bring the response back to D on the original stress–strain curve. On the other hand, if the work hardening is dependent on strain rate, the change in strain rate, at γ_T, will switch the response from A to B', and work hardening will proceed along $B'C'$ (see Fig. 14.24*b*). The strain hardening dependence of strain rate has been defined by Klepaczko [14] as

$$\lambda_n = \frac{\Delta\tau_h}{\log \left.\dfrac{\dot{\gamma}_2}{\dot{\gamma}_1}\right|_{T,\gamma_T}} \tag{14.89}$$

where λ_n is the strain-rate sensitivity of hardening, and expresses the fact that the material work hardens differently at different strain rates. If $\lambda_n = 0$, we have the situation of Figure 14.24*a*. The evolution of the structure is not the same at low and high strain rates. This strain rate dependence of microstructural evolution is related to the immobile and mobile dislocation densities. As the strain rate changes, the relative values of ρ_i and ρ_m (the immobile and mobile dislocation densities, respectively) change, leading to different total densities and, as a corollary, different flow stresses. Klepaczko [14] expressed the total dislocation density ρ as the sum of the mobile dislocation density ρ_m and the immobile dislocation density ρ_i:

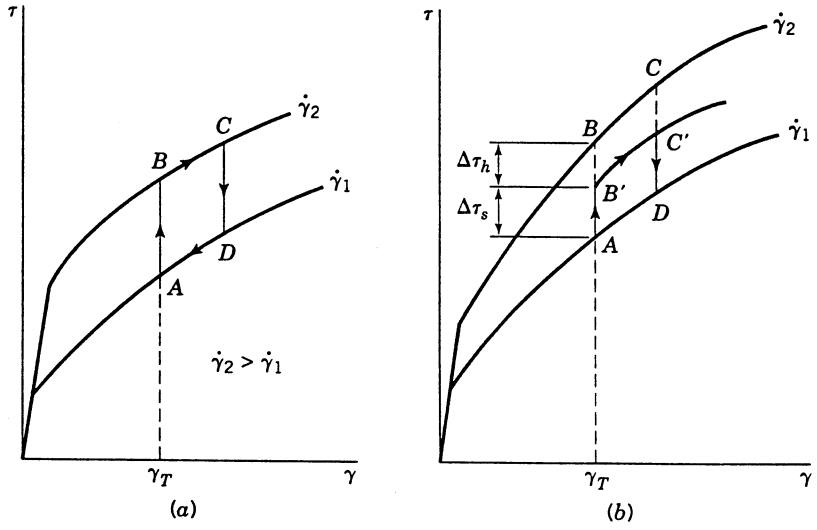

Figure 14.24 Effect of strain rate on strain hardening: (*a*) material exhibiting no strain-rate sensitivity of strain hardening; (*b*) material exhibiting strain-rate sensitivity of strain hardening.

$$\rho = \rho_i + \rho_m \tag{14.90}$$

Then, he expressed the total shear stress τ as the sum of the athermal and thermal components:

$$\tau(\dot{\gamma}, T, S_j)_\gamma = \tau_G[S_j(\dot{\gamma}, T)]_\gamma + \tau^*[\dot{\gamma}, T, S_j(\dot{\gamma}, T)]_\gamma \tag{14.91}$$

where the S_j are the internal variables, which are a function of strain rate and temperature. The principal internal variables are the mobile and immobile dislocation densities. The first (athermal) component of stress can be given by the Taylor equation:

$$\tau_G = \alpha_1 Gb(\rho_i + \rho_m)^{1/2}$$

For the thermal component of stress, on the other hand, the rates of dislocation generation and annihilation are strain-rate- and temperature-dependent. Klepaczko [14] developed analytical expressions for the change in mobile and immobile dislocation densities with strain, $\partial\rho_i/\partial\gamma$, $\partial\rho_m/\partial\gamma$, and incorporated these effects into the thermal component of the stress. This leads directly to predicted responses in line with the results of Figure 14.24. The MTS model takes the strain-rate dependence of microstructural evolution into effect and therefore represents, at this stage, the most advanced representation of the constitutive behavior of metals. The flow stress has to be established, at each level of plastic strain, with the proper evolution laws. One does not have a straightforward manner of obtaining the work hardening. It is a function of the prior evolution of the substructure, which is a function of ϵ, $\dot{\epsilon}$, and T.

14.4 MECHANICAL TWINNING

14.4.1 Mechanisms of Twin Formation

The crystallographic aspects of twinning will not be discussed here. It is known that mechanical twinning and slip are competing mechanisms and that mechanical twinning is favored at low temperatures and high strain rates. Mechanical twinning requires dislocation activity, and it is generally accepted that microslip is required for twinning to occur. There are a number of monographs exclusively devoted to mechanical twinning, including the reviews by Christian and Mahajan [25] and Reed-Hill et al. [26], which describe the phenomenon of twinning in great detail. In terms of the dislocation theory, several mechanisms have been proposed for deformation twinning formation. One very well-known mechanism is called the "pole mechanism." A partial dislocation approaches a tree dislocation that has, at least partially, a screw character. The atomic planes form a ramp around the screw or partially screw dislocation. The free disloca-

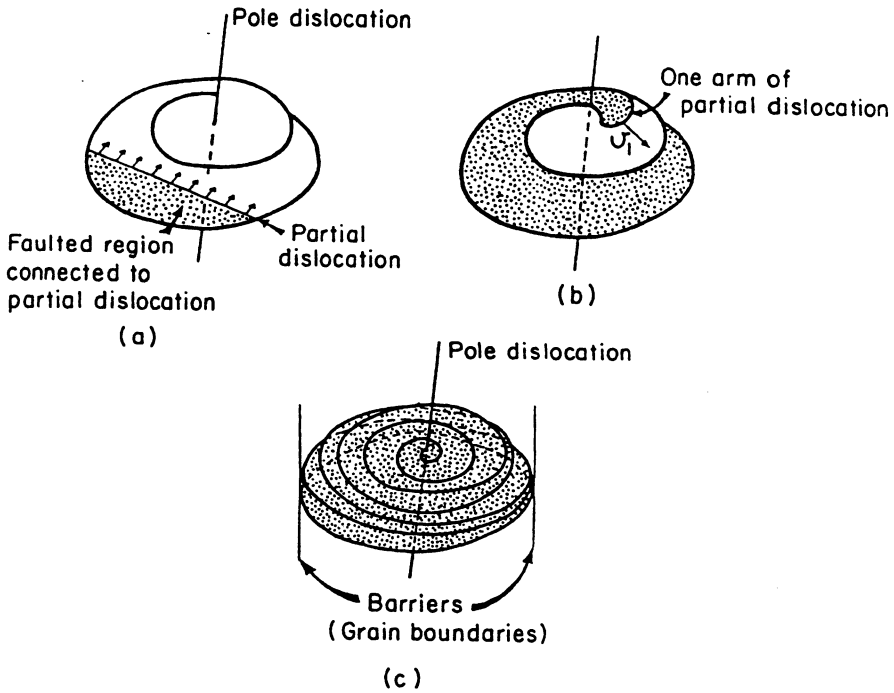

Figure 14.25 "Pole" mechanism for twinning.

tion serves as a pole for the spiral ramp. When the partial dislocation meets the pole dislocation, the leading partial dislocation will move a plane up (Fig. 14.25*b*), and the other arm will move a plane down. The two arms, thus, will move in spirals around the pole dislocation. Eventually, one will have moved a partial dislocation through all the planes in succession and, thus, one will have a deformation twin. Figure 14.25*c* shows the process, after the dislocation has spun around the pole several times. The length of the twin is limited by the lateral barriers (in this case, grain boundaries). One can therefore envisage how a lenticular twin is produced. Notice that the bottom portion of the twin in Figure 14.25*c* is produced in the same manner, except that the other arm of the partial dislocation produced it, rotating in the opposite sense. This is the pole mechanism proposed by Cottrell and Bilby [27] for BCC metals and extended by Venables [28] to FCC metals. The principal deterrent to the pole mechanism is the maximum rate of growth predicted by this model; it is of the order of 1 m/s. This is about three orders of magnitude below values reported by Bunshah [29] and Takeuchi [30]. Takeuchi found that a twin propagated at 2500 m/s in iron, and that this velocity was virtually independent of temperature in the interval −196 to +126°C. The latter observation is very important and indicative of the fact that growth is not a thermally activated process. Figure 14.26 shows the temperature dependence of the twinning stress for Fe, FeSi

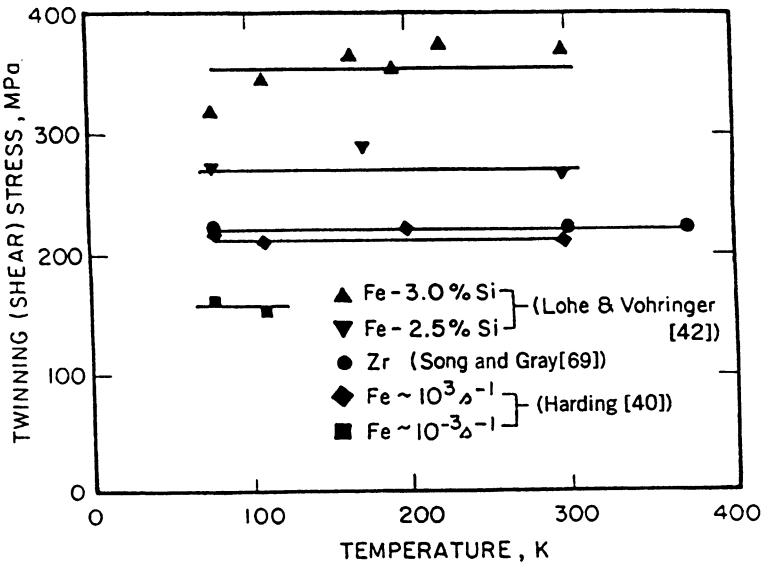

Figure 14.26 Illustration of low temperature sensitivity of twinning stress.

and Zr. The temperature has only a mild effect, in contrast with Figure 14.1. Two strain rates were used for iron: 10^{-3} and $\sim 10^{3}$ s^{-1}. This increase in the strain rate by six orders of magnitude resulted in only a 30% increase in the yield stress. In contrast, the yield stress (for slip) increases by over 80% in the same range. Takeuchi [30] measured the twinning propagation velocity in iron at 77, 301, and 400 K and found that it was insensitive to velocity and equal to approximately 2.5 mm/μs. This corresponds approximately to the velocity of shear waves along [110]:

$$v_{s1} = \left(\frac{C_{11} - C_{12}}{\rho}\right)^{1/2} = 2.47 \text{ mm}/\mu\text{s} \qquad (\zeta = [110])$$

$$v_{s2} = \left(\frac{C_{44}}{\rho}\right)^{1/2} = 3.70 \text{ mm}/\mu\text{s} \qquad (\zeta = [001]) \qquad (14.92)$$

Hornbogen [31] suggested that the propagation of twins in FeSi alloys occurs at such a rate as to generate shock waves. It is the velocity limitation that led Cohen and Weertman [32] to propose a much simpler model for FCC metals, involving the production of Shockley partials at Cottrel–Lomer locks and their motion through the material. The velocity of propagation of a twin is in this case simply established by the velocity of motion of the Shockley partials. Hirth and Lothe [33] proposed a yet simpler model in which the dislocations are simply homogeneously nucleated; while the stress required to homogeneously

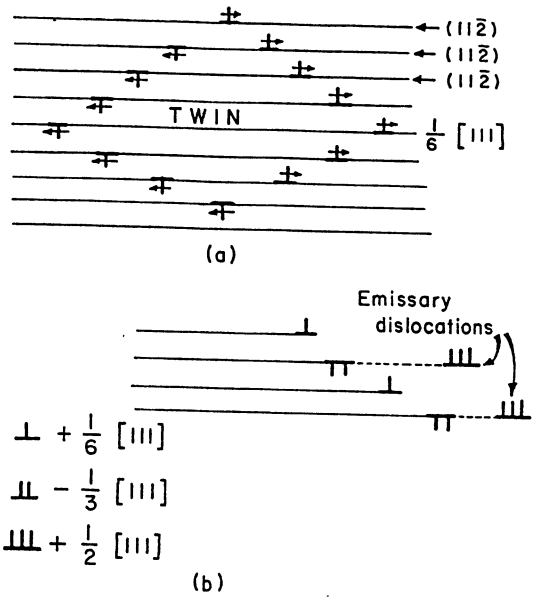

Figure 14.27 (*a*) Formation of twin in BCC crystal by successive formation of loops on (112) planes; (*b*) decrease of twin boundary energy by decomposition of dislocations and formation of emissary dislocation.

nucleate the first dislocation is of the order of 10% of the shear modulus, the subsequent loops would require stresses that are much lower (1% of G). This "homogeneous nucleation" concept was forwarded first by Orowan [34].

The mechanism of twin formation proposed by Sleeswyk [35] for BCC materials is phenomenologically identical to that of Cohen and Weertman [32] for FCC materials.

The mechanism proposed by Sleeswyk [35] is shown in Figure 14.27. Loops of $\frac{1}{6}$ [111] dislocations on successive {112} planes form, by their expansion, the deformation twin. The thickness of the twin increases by the creation of new loops along {112} planes. When the number of loops exceeds 40. dislocation reactions are thought to occur along every third {112} plane. The following dislocation reaction was postulated by Sleeswyk [35]:

$$\tfrac{1}{6}\langle 111\rangle \rightarrow \tfrac{1}{2}\langle 111\rangle - \tfrac{1}{3}\langle 111\rangle$$

The $\frac{1}{2}\langle 111\rangle$ dislocation is emitted ahead of the twin and becomes an "emissary" dislocation. These dissociations are shown in schematic fashion in Figure 14.27.

Mahajan [36] carefully studied the crystallography and dislocation configurations in twinned Mo/3.5Re alloy by transmission electron microscopy. His observations seem to support Sleeswyk's model over that of Cottrell and Bilby. The initiation of twinning seems to occur by the dissociation of a $\frac{1}{2}\langle 111\rangle$ screw

dislocations into three $\frac{1}{6}\langle 111\rangle$ dislocations on adjacent layers. The parallel movement of these dislocations produces a three-layer twin. The broadening (increase in thickness) is accomplished by additional dissociations on parallel planes.

14.4.2 A Constitutive Equation for Twinning

A simple, yet effective, constitutive description of twinning will be given here. It was proposed by Meyers et al. [37]. There are other equations, developed by Armstrong and Worthington [38] and Ogawa [39]. The key and common factor of these models is that a high local stress is required for the initiation of twinning. We will not use the term *nucleation* since it implies a thermodynamic process in which there is a change in chemical equilibrium. The dislocation pileup is recognized, by many researchers, as being capable of generating these stresses. We assume, further, that the critical rate controlling mechanism is the initiation stage. This is because propagation, as seen in Section 14.4.1, can occur at sonic velocities, and leads to times that are on the order of

$$t = \frac{d}{v} = \frac{50 \times 10^{-6}}{2.5 \times 10^{3}} = 2.0 \times 10^{-8} \text{ s}$$

where d is an estimated grain size (~50 μm). Except at the shock front, where the rise times of the wave is in the order of 10^{-8} s, we do not have such short time limitation imposed of twinning.

We consider the dislocation pileup, created by a Frank–Read or a Koehler source as shown in Figure 14.28. We apply the dislocation dynamics equation from Johnston and Gilman [Eq. (14.21)] to the individual dislocations forming the loops:

$$v = A\tau^{m} e^{-Q/RT} \tag{14.93}$$

The distance from the source to the barrier (in this case, a grain boundary) is L. The time required for an individual dislocation to travel from source to barrier is

$$t_1 = \frac{L}{v}$$

The number of dislocations required at a pileup to generate the stress initiation τ_i is n^*. Thus

$$\tau_i = n^* \tau_{AP} \tag{14.94}$$

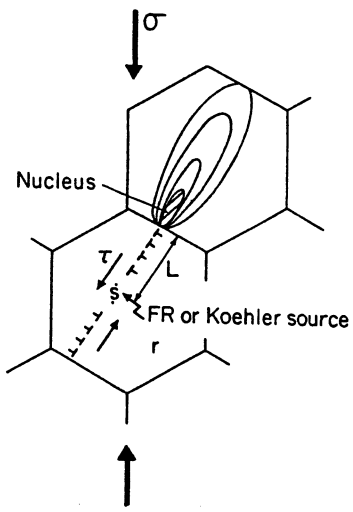

Figure 14.28 Nucleation of twin from stress concentration created by Frank–Read or Koehler dislocation source.

where τ_{AP} is the externally applied stress. Assuming, to a first approximation, that all dislocations in source travel the same distance (equal to L), and that only one dislocation is traveling at each instant we have

$$t = n^* t_1$$

Hence

$$t = \frac{n^* L}{A\tau^m} e^{Q/RT} \tag{14.95}$$

Twinning occurs when the material is loaded elastically. Assuming a loading configuration:

$$E = \frac{\sigma}{\epsilon} \quad \text{and} \quad \dot{\epsilon} = \frac{\sigma}{Et} \tag{14.96a}$$

Substituting Eqs. (14.93) and (14.95) into Eq. (14.96a) ($\sigma = 2\tau$ for an ideal orientation $\theta = \pi/2$ for twinning), we obtain

$$\sigma = 2\left(\frac{n^*LE}{2A}\right)^{1/(m+1)} \dot{\epsilon}^{1/(m+1)} e^{Q/(m+1)RT} = K'\dot{\epsilon}^{1/(m+1)} e^{Q/(m+1)RT} \quad (14.97b)$$

Since, obviously, twins can still be generated when the strain rate is very low, an athermal stress should be added to Eq. (14.96a).

14.4.3 Application to Iron and Copper

This constitutive equation is applied to the experimental data obtained by Harding [40] for monocrystalline iron. The dislocation dynamics parameters were obtained from Stein and Low [17] for Fe/3.5Si and are, for edge dislocations, Q = 51.66 kJ/mol, K' = 380 MPa, m = 36.

The results are plotted in Figure 14.29, where the temperature and strain-rate dependence of the twinning stress are well represented. For comparison purposes, the yield stress for slip is also shown in the same plot. Calculated values are continuous (or hatched) lines, and experimental results are given by points. The curves for slip were obtained from the application of the Zerilli–Armstrong constitutive equation [Equation (14.87)] for a monocrystal. It is clear that the temperature and strain-rate sensitivities for slip are much higher than those for twinning. From the curve plotted in Figure 14.29, it is possible to obtain the

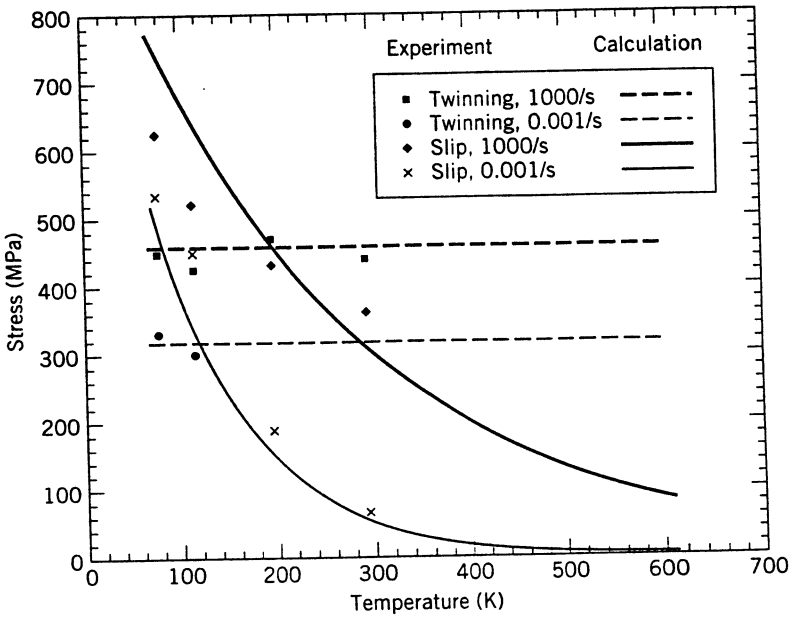

Figure 14.29 Comparison of calculated and measured slip and twinning stresses for monocrystalline iron. (From M. A. Meyers, O. Vöhringer, and Y. J. Chen [37])

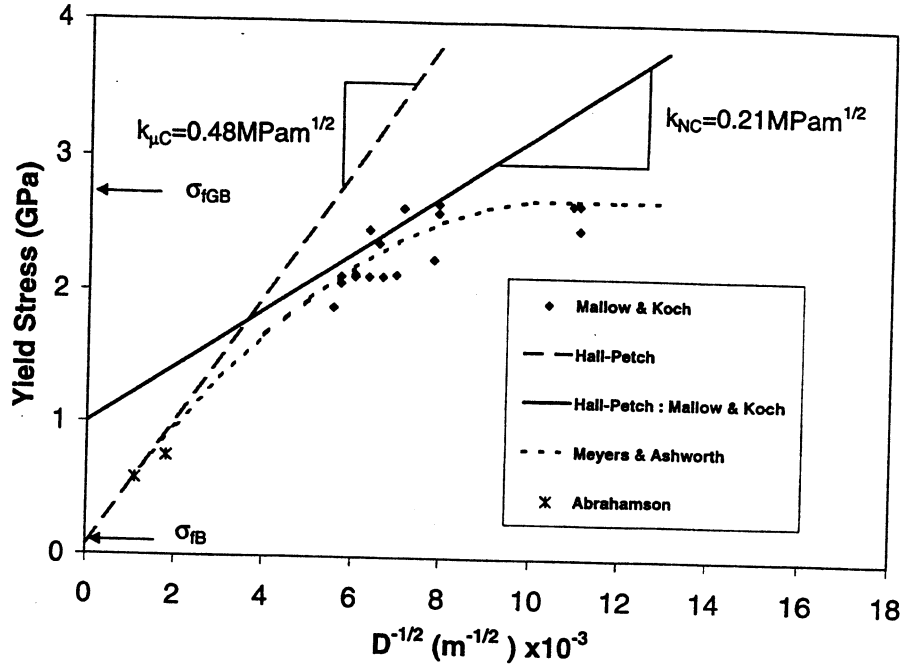

(*a*)

Figure 14.30 (*a*) Experimentally measured Hall–Petch and Meyers–Ashworth yield stress versus grain size response for iron (results from T. R. Malloy and C. Koch, Met. and Mat. Trans. A, *29A* (1998) 2285; E. P. Abrahamson, II, in *Surfaces and Interfaces*, Syracuse U. Press, 1968, p. 262); (*b*) Hall–Petch slopes for slip (as a function of strain rate) and twinning (assumed to be, to a first approximation, strain-rate-independent) for copper. (Experimental high-strain rate point from W. Tong, R. J. Clifton, and S. Huang, J. Mech. Phys. Sol. *40* (1992) 1251).

slip–twin transition for iron. The critical temperature rises from ~120 K at strain rates in the 10^{-3}-s^{-1} range, to 200 K, at 10^3 s^{-1}. This relationship breaks down at 1183 K, the $\alpha \rightarrow \beta$ transition temperature.

14.4.4 Grain-Size and Stacking-Fault Energy Effects

The grain size dependence of the twinning stress has been successfully described by a Hall–Petch-like relationship:

$$\sigma_T = \sigma_{0T} + k_T d^{-1/2} \tag{14.97a}$$

The Hall–Petch slope for twinning has been shown [38, 39, 41–43] to be considerably higher than the Hall–Petch slope for slip. The micromechanisms initiating twinning (dislocation pileups) and slip (arguably, the stress concentration

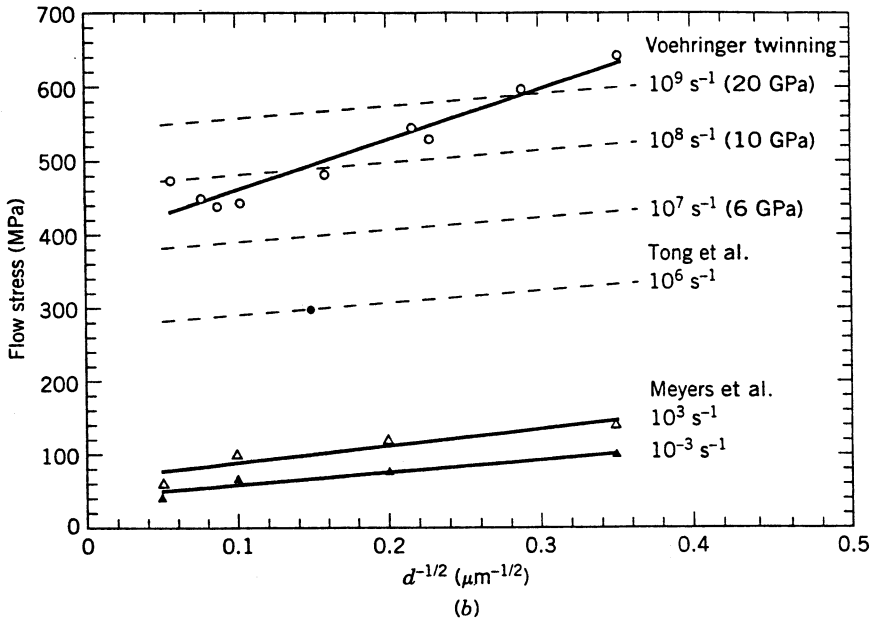

(*b*)

Figure 14.30 (*Continued.*)

at grain boundaries due to elastic anisotropy of metals, as proposed by Meyers and Ashworth [44]) are possibly quite different; this would explain the differences in slope. Meyers and Ashworth [44] proposed a mechanism based on the formation of a grain-boundary layer where the dislocation density is much higher than the grain interior. This layer is formed during the early stages of plastic deformation and is assumed to have a flow stress σ_{fGB}. This layer is the result of the elastic incompatibility between adjacent grains (elastic anisotropy), dislocation sources at grain boundaries, and the fact that the grain boundary is an obstacle for dislocation motion. The Meyers–Ashworth model provides a linkage to the nanocrystalline scale, where it is well known that the Hall–Petch slope is severely reduced. The material is envisaged as a composite, comprised of the grain interiors, with flow stress σ_{fB}, essentially equal to the monocrystalline value, and the grain-boundary work hardened layers, with flow stress σ_{fGB}. The Meyers–Ashworth equation is

$$\sigma_y = \sigma_{fB} + 8k(\sigma_{fGB} - \sigma_{fB})D^{-1/2} - 16k^2(\sigma_{fGB} - \sigma_{fB})D^{-1} \qquad (14.97b)$$

where σ_{fGB} and σ_{fB} are the flow stresses of the grain boundary and grain interior, respectively. It differs from the formulations presented in Chapter 10 by Armstrong because it is not based on a pileup. It provides a grain size dependence for iron, seen schematically in Figure 14.30*a*. The conventional Hall–Petch response breaks down at very small grain sizes with a decrease in

the slope, because of the third term in the equation. It should be noticed that it predicts no grain size sensitivity for tungsten, which has $E_{111} = E_{110} = E_{100}$. It is probable that both elastic anisotropy and barrier effects determine the grain size sensitivity. Hence, three principal factors contribute to the grain-size dependence of flow stress:

1. The grain boundaries act as barriers to plastic flow.
2. The grain boundaries act as dislocation sources.
3. Elastic anisotropy creates additional stresses in the grain-boundary surroundings.

The differences in Hall–Petch slope for slip and twinning lead to very unique strain-rate effects, that were pointed out, for the first time, by Meyers et al. [45]. This effect is clearly illustrated in Figure 14.30*b* for copper. The Hall–Petch dependencies for slip and twinning are both shown. It is assumed to a first approximation, that the Hall–Petch relationship for twinning is fixed and strain-rate-independent. The Hall–Petch relationship for slip is translated upward, as shown in Figure 14.30*b*, as the strain rate is increased. The differences between k_y and k_T lead to the intersection of the two lines, in the region $\sim 10^{-8}$ s^{-1}, for a grain size of 40 μm, marked in the figure. Copper specimens with grain size larger than 40 μm should twin before slipping, at 10^8 s^{-1}. On the other hand, specimens with grain sizes smaller than 40 μm slip before twinning at this strain rate. This effect seems to be prevalent in FCC (as shown for copper by Meyers et al. [45]), BCC, and HCP metals.

The effect of grain size on the slip-twinning transition for iron is shown in Figure 14.31. Figure 14.31*a* shows how the intersections of the slip and twinning equations, for a grain size of 100 μm, lead to transition points. Five points are obtained in Figure 14.31*a* and replotted in the temperature-strain rate plot of Figure 14.31*b*. By using the appropriate Hall–Petch parameters for slip and twinning (that are different), the curves for different grain sizes are developed. The effect of grain size on the slip-twinning transition is evident.

The stacking-fault energy, γ, has a significant effect on the twinning stress for FCC metals. The analysis carried out by Meyers et al. [37] is summarized here. The following expression is experimentally found:

$$\sigma_T = K_2 \left(\frac{\gamma}{Gb} \right)^{1/2} \tag{14.98a}$$

As an illustration of the effect of SFE on the incidence of twinning, the Cu-Zn system is analyzed. The SFE can be correlated to the concentration of solutes in copper alloys and the following expression can be written:

$$\ln \gamma = \ln \gamma_{Cu} + K_1 \left(\frac{C/C_{\max}}{1 + C/C_{\max}} \right)^2 \tag{14.98b}$$

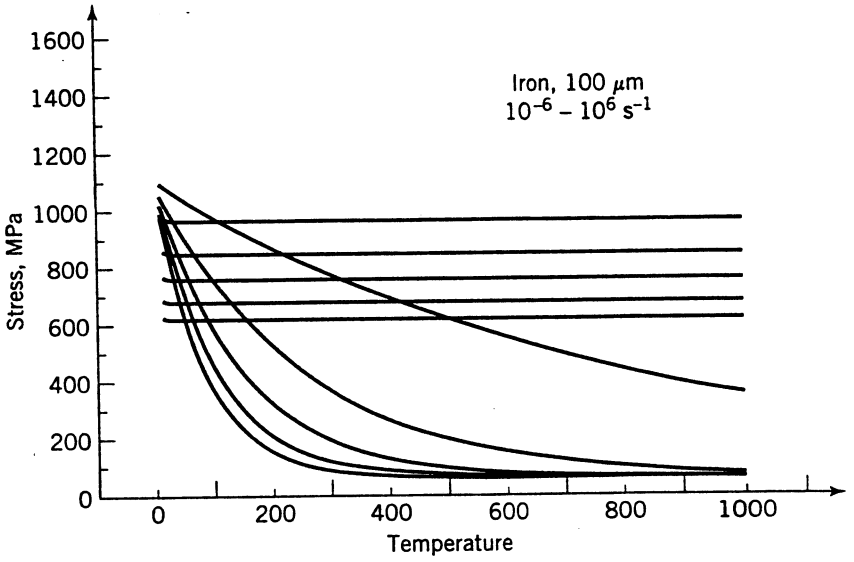

(*a*)

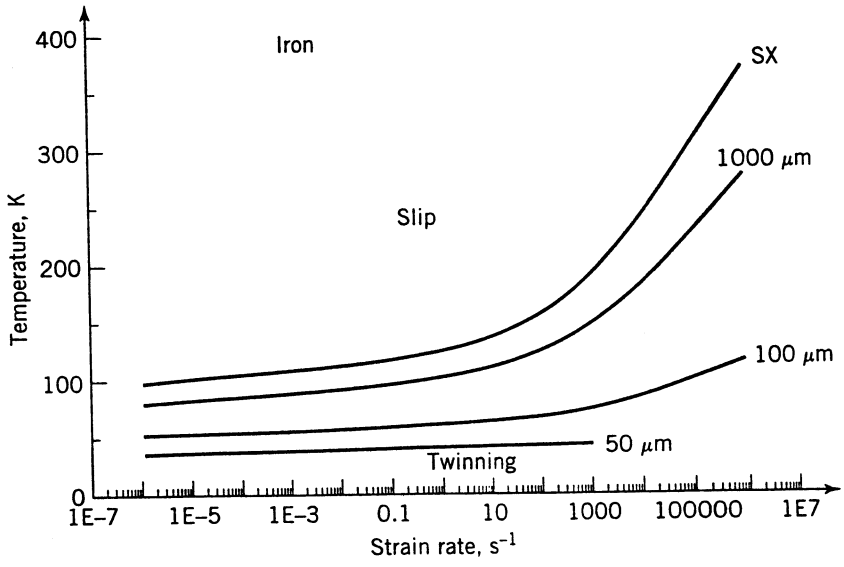

(*b*)

Figure 14.31 (*a,b*) Effect of temperature, strain rate, and grain size on slip–twinning transition for iron. (*c,d*) Effect of stacking-fault energy on the slip-twinning transition of brass (monocrystalline (*c*) and polycrystalline (*d*)) (from M. A. Meyers, O. Vöhringer, and Y. J. Chen, in "Advances in Twinning," TMS-AIME, 1999, p. 43).

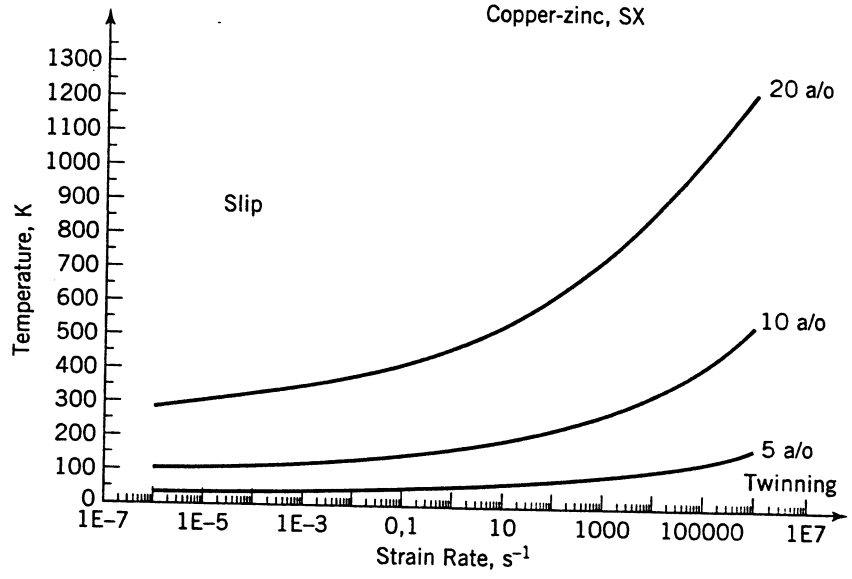

(*c*)

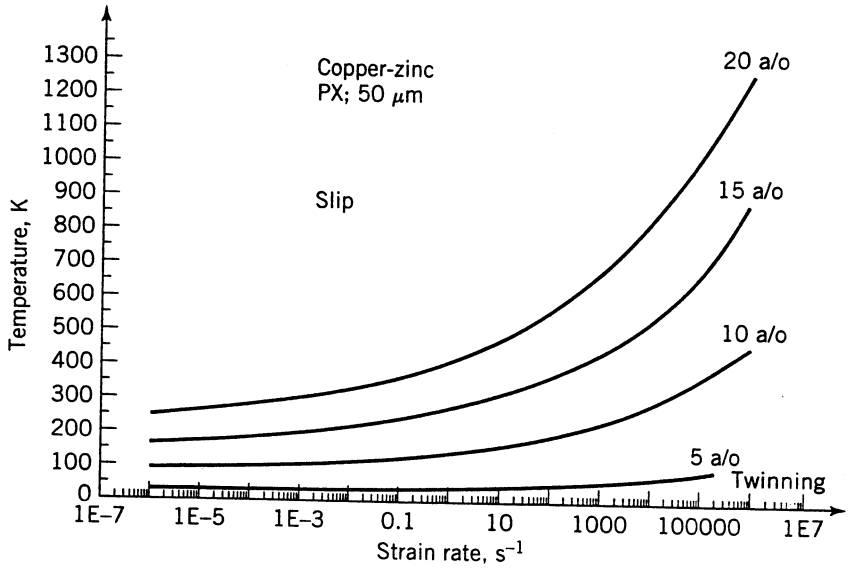

(*d*)

Figure 14.31 (*Continued.*)

where γ_{Cu} is the stacking fault energy for copper, C is the concentration of solute atoms, and C_{max} is the maximum concentration of the solute. The best fit was obtained with $K_1 = 12.5$; $\gamma_{Cu} = 57 \pm 8$ mJ/m^2; $K_2 = 6$ GPa.

Substitution of Eq. (14.98a) into Eq. (14.98b) yields:

$$\sigma_T = \frac{K_2}{(Gb)^{1/2}} \exp\left[\ln \gamma_{Cu} + K_1 \left(\frac{C^*}{1+C^*}\right)^2\right]^{1/2} \tag{14.98c}$$

The effect of solid solution (Zn, Ag, Al, Sn, Ge) atoms on the mechanical response of Cu has been carefully established; the effects of these solutes on the Hall–Petch equation has also been established. Vöhringer [168] proposed the following expression, which is used for the yield stress:

$$\begin{aligned}\sigma_s &= \sigma_G + \sigma^* + k_s D^{-1/2} \\ &= \sigma_0 + K_3 \epsilon_L^{4/3} C^{2/3} + \left[(\sigma^* + K_4 \epsilon_L C^{2/3})\left(1 - \frac{k \ln \dot{\epsilon}_0/\dot{\epsilon}}{\Delta G_0}\right)^{1/p} T^{1/p}\right]^{1/q} \\ &\quad + k_s D^{-1/2}\end{aligned} \tag{14.98d}$$

Eq. (14.98d) is based on the overcoming of short-range obstacles, that have the shape dictated by the parameters p and q. The effect of the solid solution atoms is manifested (both in the thermal and athermal components of stress) through the $C^{2/3}$ relationship and Labusch parameter ϵ_L, which has different values for different solid solution atoms. K_3 and K_4 are parameters, and $\dot{\epsilon}_0$ is a reference strain rate, that was taken by Vöhringer as 10^{20} s^{-1}.

The effect of work hardening can be incorporated into Eq. (14.98d) by adding the term $C_2\epsilon^n$ to the thermal component of stress, since work hardening increases, in FCC metals, the density of forest dislocations, which constitute short-term barriers.

The results of the calculations are represented in the slip-twinning transition plots of Figure 14.31, in which Eqs. (14.98c) and (14.98d) were used. These calculations were carried out for different Cu–Zn alloys: 5, 10, 15, and 20% at Zn. Figure 14.31*c* shows the results for monocrystalline brass, while Figure 14.31*d* shows the results for a grain size of 50 μm. It is clear that the addition of Zn increases the propensity for twinning, displacing the slip-twinning transition upwards. By using Eq. (14.98d) with the addition of the term $C_2\epsilon^n$ it is possible to establish the onset of twinning after different amounts of plastic deformation. Since Cu–Zn is FCC, the occurrence of twinning can occur after significant plastic deformation.

14.5 SHOCK-WAVE DEFORMATION: THE UPPER BOUNDARY FOR STRAIN RATES

As the strain rate is increased beyond 10^3 s^{-1}, it is increasingly difficult to ensure homogeneous stress state in the specimen. This is done by decreasing the specimen size or the plastic deformation region. Strain rates between 10^4 and 4×10^4 s^{-1} can be obtained in this fashion. Miniature Hopkinson bars, with specimens having ~1 mm dimension, yield these strain rates. By using very thin specimens, (down to a few micrometers) in a pressure–shear impact arrangement, Clifton and co-workers [46] were able to successfully generate strain rates of 10^5 s^{-1}. One problem in this configuration is that the specimen thickness is on the same order than the grain size, making the interpretation more difficult.

In the region 10^5–10^7 s^{-1}, it is virtually impossible to avoid plastic wave propagation effects, and we enter into the shock-wave region. The shock front is treated, in the simplified hydrodynamic approach, as a discontinuity in pressure, temperature, and density. In a real shock-wave propagation event there is a finite slope at the front, as illustrated in Figure 14.32*a*. The plastic wavefront is preceded by an elastic precursor. Swegle and Grady [47] took the slope of the plastic wavefront and calculated a strain rate by assuming a linear rise. They plotted these values for a number of materials as a function of the maximum stress. The results are shown in Figure 14.32*b* and, surprisingly, fall into straight lines (in the double logarithmic axes) with the same slope. This led them to propose the relationship

$$\sigma = K_5 \dot{\epsilon}^{1/4} \tag{14.99}$$

It is clear that conventional dislocation multiplication mechanisms leading to yielding at lower strain rates do not have sufficient time to be operative under the conditions imposed at the shock front. This led Meyers [48,49] to propose a mechanism for dislocation generation at the shock front that is based on an earlier idea by Smith [50], also known as the *Smith interface*. The Smith interface is not physically possible because the interface dislocations would need to move with the shock front, demanding supersonic speeds. Figure 14.33 shows the evolution of dislocation substructure as a shock front moves through an idealized crystal lattice, as envisioned by Meyers [48]. Dislocations form initially a Smith interface (Fig. 14.33*b*), disrupting elastic distortion, represented in Figure 14.33*a*. The shock front advances, and the dislocation interface is left behind (Fig. 14.33*c*). As this occurs, elastic deviatoric stresses build up. The initial calculations of resulting dislocation densities produced values orders of magnitude higher than the observed results. An improved calculation, carried out by Ravichandran and Meyers [51], predicts values that compare favorably with dislocation densities measured from transmission electron microscopy observations. At the interface as shown in Figure 14.34, several layers of interfa-

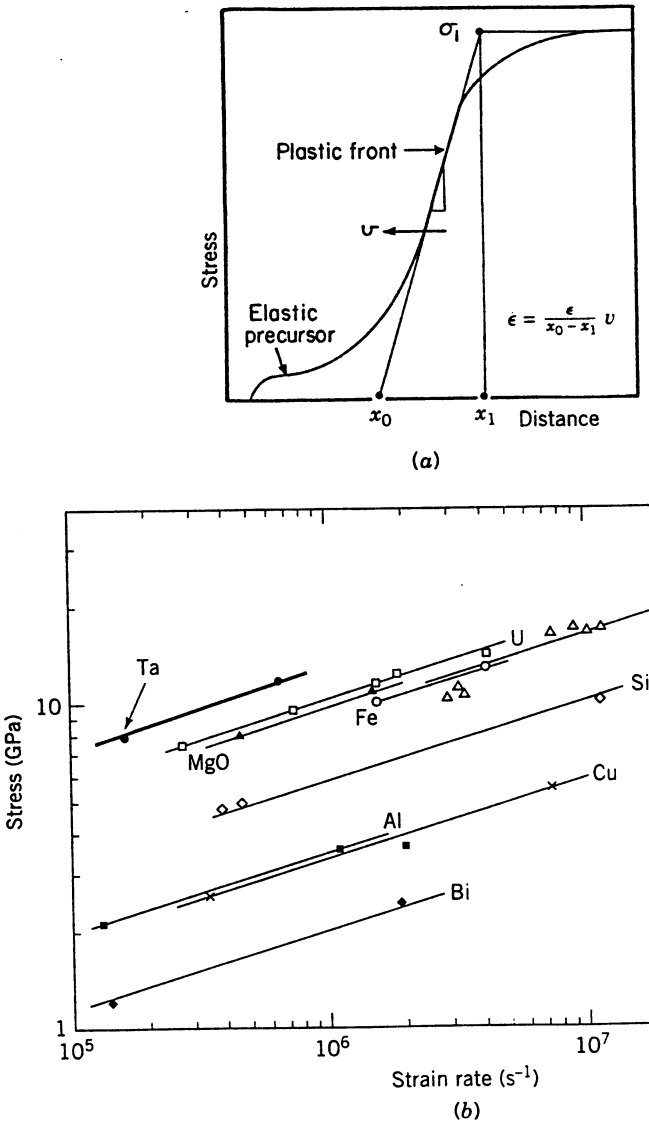

Figure 14.32 (*a*) Shock compression front and calculated strain rate; (*b*) experimentally observed relationship between strain rate and shock stress for a number of materials. (Adapted from J. W. Swegle and D. A. Grady, J. Appl. Phys. *58* (1985) 692).

cial dislocations were left behind by the shock front. Elastic distortion at the shock front is balanced by the stress fields due to the dislocation arrays. When the deviatoric elastic stresses at the front reach a critical level, dislocations are again generated. The dislocation spacing along the front, l_c, can be calculated from the lattice contraction. In order to calculate h, the superposition principle

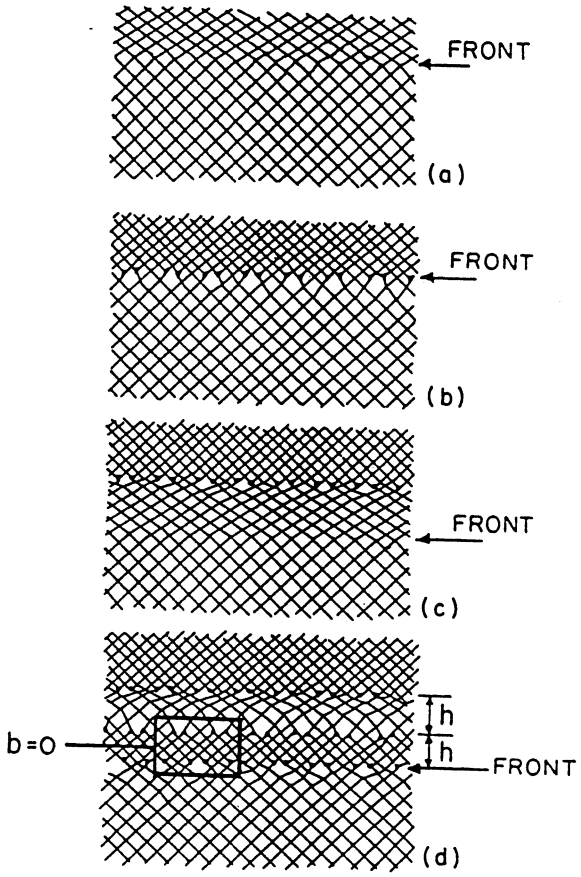

Figure 14.33 Homogeneous dislocation generation in shock compression. [Adapted from M. A. Meyers, Scripta Met. *12* (1978), 21.]

was applied and the total stress at a point on the front due to the dislocation array is estimated. Assuming edge dislocations only:

$$\sigma_{11} \sim \frac{Gb}{2\pi(1-\nu)} \frac{2\sqrt{2}}{n\ell} \quad \rightarrow \sum_{-\infty}^{\infty} \frac{1}{n} = 0$$

$$\sigma_{22} \sim \frac{Gb}{2\pi(1-\nu)} (-2h^2) \frac{2\sqrt{2}}{n^3\ell^3} \quad \rightarrow \sum_{-\infty}^{\infty} \frac{1}{n^3} = 0 \qquad (14.100)$$

$$\sigma_{12} \sim \frac{Gb}{2\pi(1-\nu)} \frac{2\sqrt{2}h}{n^2\ell^2} \quad \rightarrow \sum_{-\infty}^{\infty} \frac{1}{n^2} = \frac{\pi^4}{90}$$

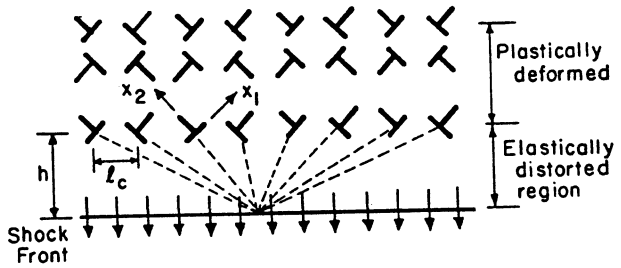

Figure 14.34 Computation of maximum thickness h of elastically distorted region in shock compression. (From G. Ravichandran and M. A. Meyers, unpublished results.)

where n is a positive integer designating the position of the dislocation ($n = 1, 2, 3 \cdots \infty$). The series converge and lead to the estimate of the stresses.

Thus:

$$\sigma_{11} \sim 0 \qquad \sigma_{22} \sim 0$$

$$\sigma_{12} \sim \frac{Gb}{\sqrt{2}(1-\nu)} \frac{\pi^3 h}{45\ell^2} \tag{14.101}$$

When the stresses at the front reach a level at which homogeneous dislocation nucleation can occur, then a new layer is formed. The dislocation density can be obtained from

$$\rho = [(l_c)^2 h]^{-1} \tag{14.102}$$

The stress for homogeneous nucleation of partial dislocation is:

$$\frac{\tau}{G} = 0.054 \tag{14.103}$$

Setting it equal to Eq. (14.101):

$$h \approx \frac{1-\nu}{b\pi^2} \ell_c^2 \tag{14.103a}$$

From Eqs. (14.102) and (14.103a) and the equation of state one can obtain the dislocation density as a function of shock pressure.

The calculated values as a function of pressure, for nickel, are shown in Figure 14.35. The calculated densities are significantly higher than measured values at low pressures and approach them at higher pressures. If additional considerations, such as dislocation motion and annihilation, are taken into consideration, a better fit to the data could be obtained.

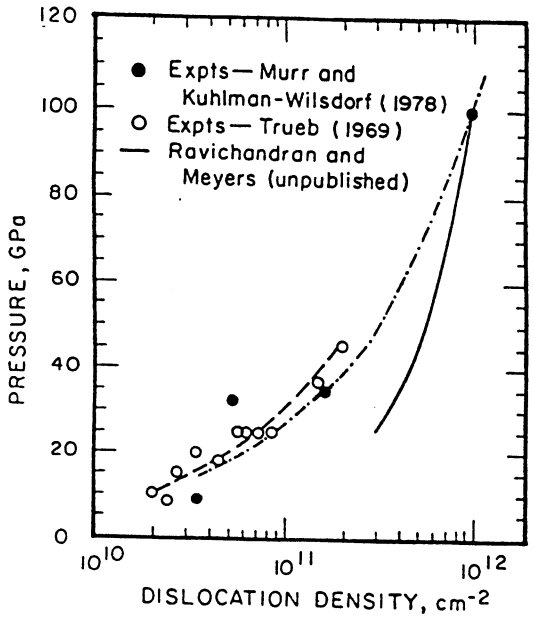

Figure 14.35 Measured and calculated dislocation densities as a function of shock compression pressure for nickel. (Data from L. E. Murr and D. Kuhlmann-Wilsdorf, Acta Met., *26* (1978) 847, and L. Trueb, J. Appl. Phys., *40* (1969) 2976).

Recent computational results by Holian and Lomdahl [52] and Bandak et al. [53] indicate that homogeneous dislocation nucleation behind the shock front does indeed take place and confirm the soundness of the Smith–Meyers mechanism. The dislocation structures observed by transmission electron microscopy confirm this: they tend to organize themselves into cells with loose walls, a very unstable configuration (e.g. Meyers [4]).

Application of the Swegle–Grady relationship [Eq. (14.100)] to the slip–twinning threshold enables the calculation of a threshold shock stress for twinning. This is shown by the relationship, which provides a rationalization for the experimental results, obtained by a number of investigators. It has been found that metals have different threshold stresses for twinning, that depend on stacking fault energy, grain size, and temperature.

Figure 14.36 shows the calculated threshold stresses for twinning in shock compression of tantalum. This threshold stress was obtained from application of the Zerilli–Armstrong equation [Eqs. (14.87) and (14.96b)] to the Swegle–Grady equation [Eq. (14.100)]:

$$K'(K_5\sigma_{sh}^4)^{1/(m+1)}e^{Q/(m+1)RT} - C_1e^{-(C_3 - C_4 \ln K_5\sigma_{sh}^4)T} + (k_T - k_S)D^{-(1/2)} - \sigma_G = 0$$

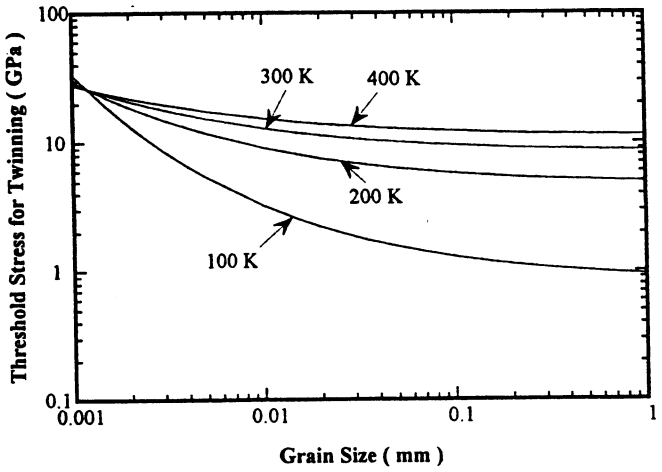

Figure 14.36 Calculated threshold twinning stress (in shock compression) for tantalum, as a function of grain size.

14.6 SHEAR LOCALIZATION

14.6.1 Mechanical Modeling

We emphasize again that a number of excellent reviews are available in the literature. The book by Bai and Dodd [4], review articles by Rogers [54], Stelly [55], and Dormeval [56], and the proceedings of a 1992 symposium on shear instabilities [57] contain a significant amount of information.

Clifton [58], Bai [59], and Molinari and Clifton [60] introduced analyses of shear instabilities that used the perturbation method together with the conservation equations. These analyses enable the prediction of the effect of perturbations on the onset of shear band formation and provide a guideline to the prediction of the evolution of a shear band. Clifton [58] improved the simplified criterion for instability proposed in the 1940s:

$$\frac{d\tau}{d\gamma} = 0 \tag{14.104}$$

Using an initial perturbation in temperature with wavenumber ξ, he obtained

$$\left[\frac{1}{\tau}\left(\frac{d\tau}{d\gamma}\right) + \frac{\alpha}{\rho C}\left(\frac{d\tau}{dT}\right)\right] m\dot{\gamma} + \frac{\lambda\xi^2}{\rho C} = 0 \tag{14.105}$$

where m = strain-rate sensitivity
ρ = density
C = heat capacity
α = heat-to-work conversion factor
λ = heat conductivity

The expression derived by Bai [59] is similar. Fressengeas and Molinari [61] introduced a new perturbation method, called the *relative perturbation method*, which accounted for the nonsteadiness of plastic flow. Leroy and Molinari [62,63] extended the analysis of shear instabilities by using a two-dimensional bifurcation method. They obtained variation in shear along the band and a patterning behavior.

One-dimensional models of shear bands have the limitation that the shear strain is constant along the length of the band. This is not a true realistic representation of shear bands which exhibit a front, such as a mode II or mode III crack, and shear strains that vary along the length of the band. This aspect was considered by Kuriyama and Meyers [64], who treated the shear band as having an extremity. They showed that the advance of a shear band proceeded by the softening of the material ahead of the tip of the band. Grady [65] developed a simplified two-dimensional model for the shear band that contained a process zone. In analogy with fracture mechanics, he developed an expression for the shear band toughness K_s as

$$K_s = \sqrt{2G\Gamma_s} \tag{14.106}$$

where G is the elastic shear modulus and Γ_s is the shear band dissipation energy. This shear band dissipation energy varies over a wide range, from 15 kJ/m^2 for uranium to 800 kJ/m^2 for copper.

14.6.2 Microstructural Aspects

At the microstructural level, the material is not a homogeneous continuum. The initiation of shear localization is a critical event, which can be triggered by either external, geometric factors, or internal, microstructural factors. External initiation sites are regions of stress and strain concentration; microstructural sites are regions that undergo localized softening by some mechanism. Figure 14.37 shows in a schematic fashion, a number of these mechanisms. Possible microstructural initiation sites are fractured second-phase particles (Fig. 14.37*c*); dislocation pileups are released as an avalanche or (Fig. 14.37*d*) as geometric softening resulting from the rotation of atomic planes toward orientations with a lower Schmid factor, and preferential slip paths produced by martensite transformation and twinning (Fig. 14.37*f*). Armstrong et al. [66] performed calculations indicating that the heat generated in a pileup release is sufficient to

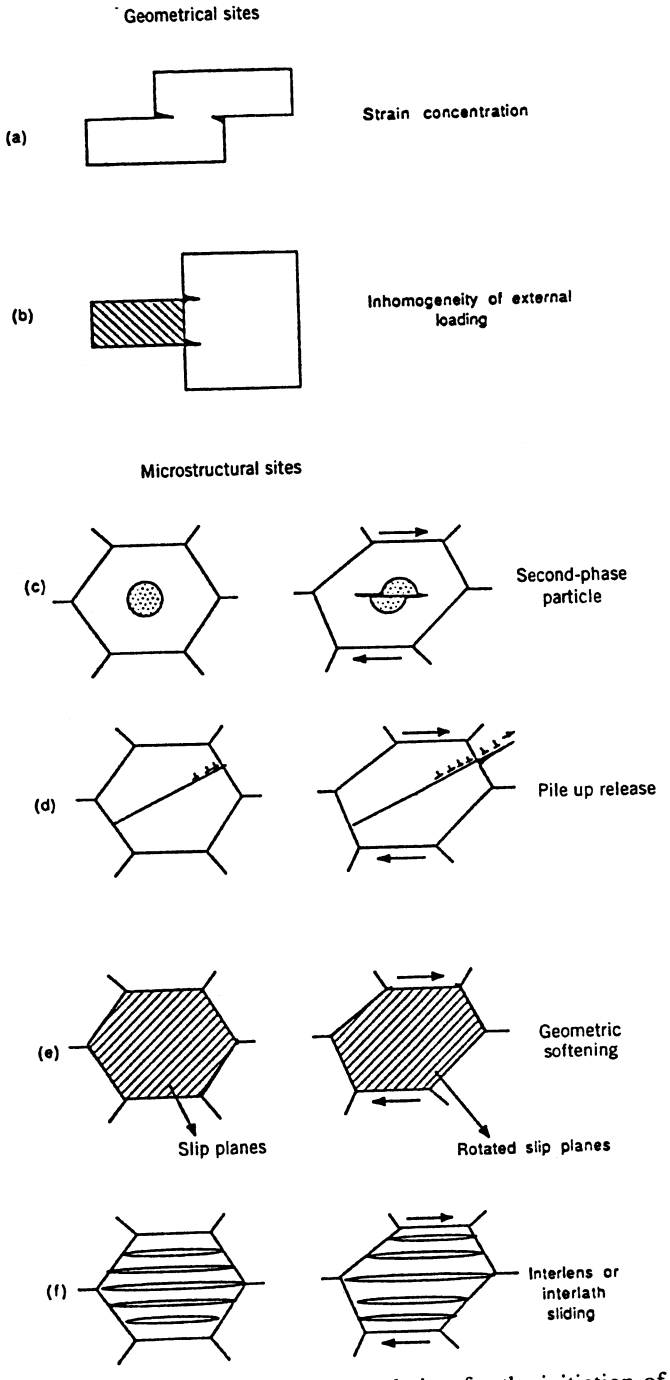

Figure 14.37 Geometric and microstructural sites for the initiation of shear bands.

initiate a shear band. Another very interesting mechanism was advanced by Weertman and Hecker [67], who proposed that local dislocation reorganization produced elongated dislocation-free regions that were initial shear bands. Meyers et al. [68] observed similar features on shock-loaded nickel subjected to subsequent tension. Localized regions (shaped like an oblate spheroid), virtually dislocation-free, were produced from the densely deformed material, leading to shear failure by a softening mechanism.

Adiabatic shear bands are the favorite sites for failure, either by ductile void nucleation, growth, and coalescence, or by cracking. The material within the shear band is heated to a high temperature and, therefore, has a lower flow stress than the surrounding matrix. Thus, tensile stresses will open voids at the shear band. Alternatively, after cooling, the material in the shear band can be harder and more brittle than the surrounding matrix. A number of examples of failure initiation at the shear bands are described by Grebe et al. [69], Wittman et al. [70], Meyers and Wittman [71], Beatty et al. [72], and Stelly et al. [73]. Figure 14.38 shows the formation of cracks and voids for four different alloys.

The microstructural evolution inside the shear band has been actively studied since the late 1980s, and it was independently discovered by Stelly and Dormeval [55,56] and Meyers and Pak [74] that the structure inside the shear band of titanium consisted of fine (<1 μm) recrystallized grains. Figure 14.39 shows these recrystallized grains for titanium [74] and copper [76]. Since 1986, a number of investigators have observed recrystallized structures inside shear bands. Of particular interest are armor steels, and Meunier et al. [75], and Beatty et al. [72] have found strikingly analogous results—the material within the shear band consisted of nanoscale grains (~50 nm). Figure 8 of Meunier et al. [75] and Figure 10 of Beatty et al. [72] are almost identical.

Often, the critical event governing localization is the attainment of the recrystallization temperature. Thus, the material can exhibit unstable behavior, specifically, a negative slope in the true stress–true strain curve, without shear band formation. Meyers et al. [8] observed this behavior for titanium and the results are shown in Figure 14.40. This figure shows the temperature as a function of strain for plastic deformation at 10^4 s^{-1}. Instability is reached much earlier than localization (clear shear band formation). Similar results were found for tantalum by Chen et al. [6]. The stress–strain curve shown in Figure 14.41, for a strain rate of 3500 s^{-1}, decreases steadily from $\epsilon = 0.1$ to $\epsilon = 0.7$, when the test was interrupted. This softening is due to the effect of temperature on thermally activated dislocation motion. The cross section of the resulting specimen shown in Figure 14.41 does not show any shear band. Localization was prevented by the temperature, which does not reach a sufficiently high level for recrystallization. The incorporation of constitutive equations that in turn incorporate a flow stress drop due to dynamic recrystallization should help the modelers create more realistic representations. Andrade et al. [9] proposed a modified Johnson–Cook equation with a flow stress discontinuity [Eq. (14.13)].

The microstructural evolution leading to dynamic recrystallization has been discussed by Andrade et al. [76], Chen et al. [6], and Meyers et al. [8]. It

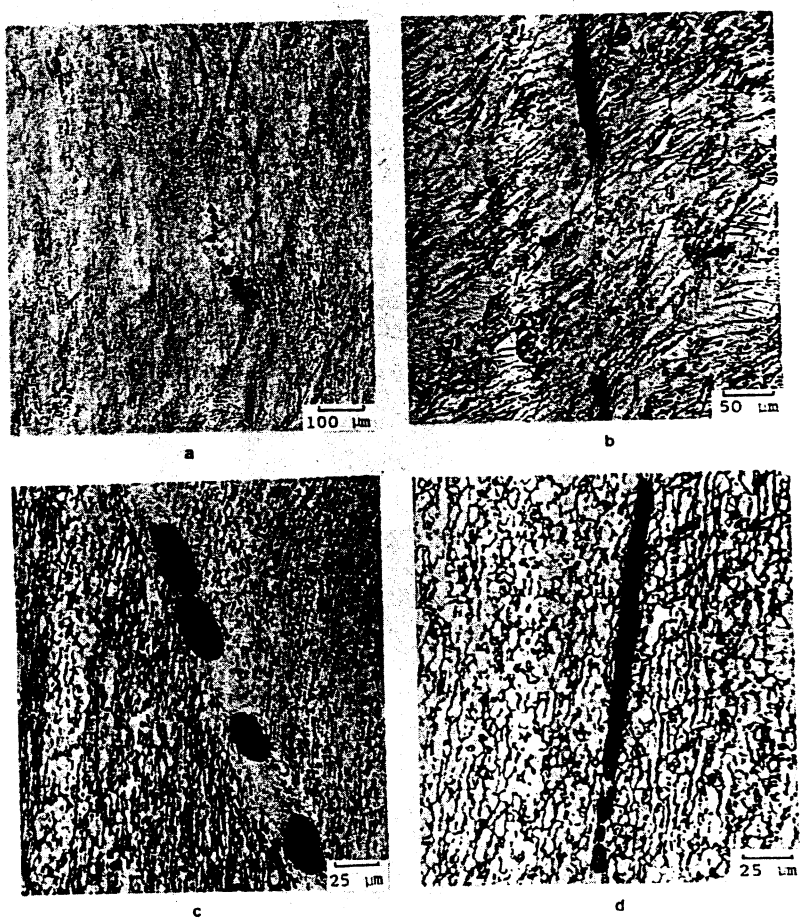

Figure 14.38 Crack and void formation along shear bands: (*a*) Ti; (*b*) TiAlV alloy; (*c*) AISI 1080; (*d*) AISI 4340 alloy.

seems clear that the short duration of the deformation–cooling time inhibits diffusional processes. Dynamic recrystallization has been classified by Derby [77] into migrational and rotational. The dynamic recrystallization observed by Andrade et al. [76] in copper is clearly of the rotational type, as evidenced by the total absence of recrystallization annealing twins that would necessarily occur in migrational processes. Similarly, results on tantalum confirm this process. Rotational recrystallization needs concurrent plastic deformation. It is well documented for geologic materials such as quartz, halite, marble, and sodium nitrate, and has recently been observed for copper by Andrade et al. [76]; observations within shear bands in titanium are also suggestive of this mechanism [8,74]. Figure 14.42 shows the primary features of the proposed mechanism.

(*a*)

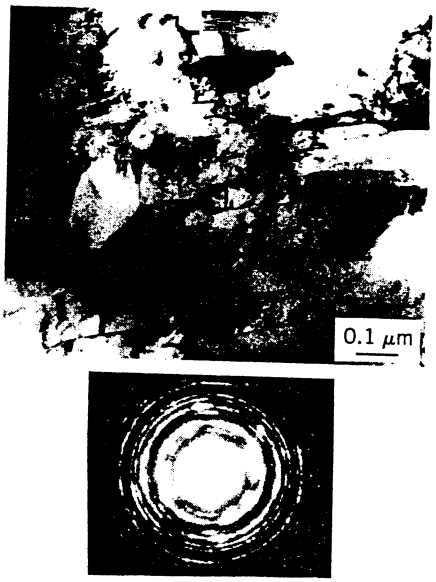

(*b*)

Figure 14.39 Recrystallized structure with grain diameters of 0.1–0.3 μm observed in (*a*) shear band in titanium [74] and (*b*) in copper [76].

For convenience, it was divided into four stages. Random dislocation distribution (stage 1) gives way to elongated dislocation cells (stage 2), which become elongated subgrains (stage 3) as deformation is increased. With further deformation, these subgrains break up into micrograins that are approximately equiaxed

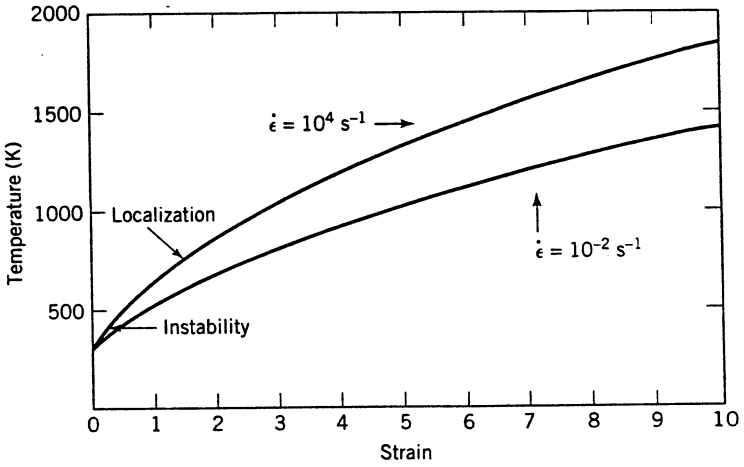

Figure 14.40 Temperature versus plastic strain for titanium; instability and localization temperature are indicated. (Adapted from M. A. Meyers, G. Subhash, B. Kad, and L. Prasad, Mech. of Matls., *17* (1994) 175).

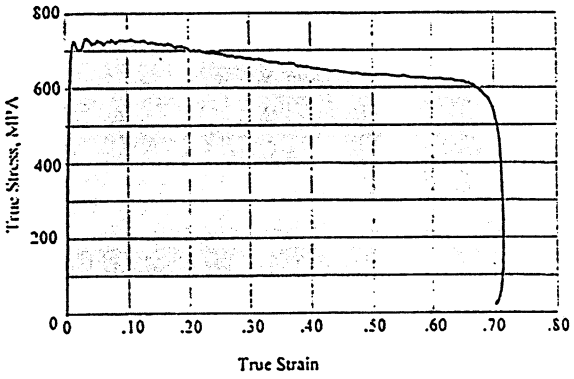

(a)

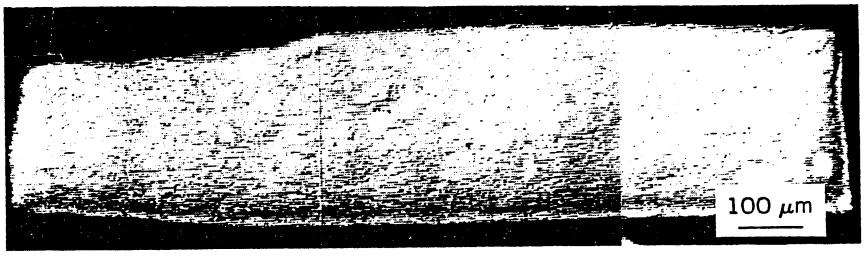

(b)

Figure 14.41 (*a*) True stress–true strain curve for tantalum at 3500 s^{-1}; (*b*) cross section of specimen, showing absence of localization.

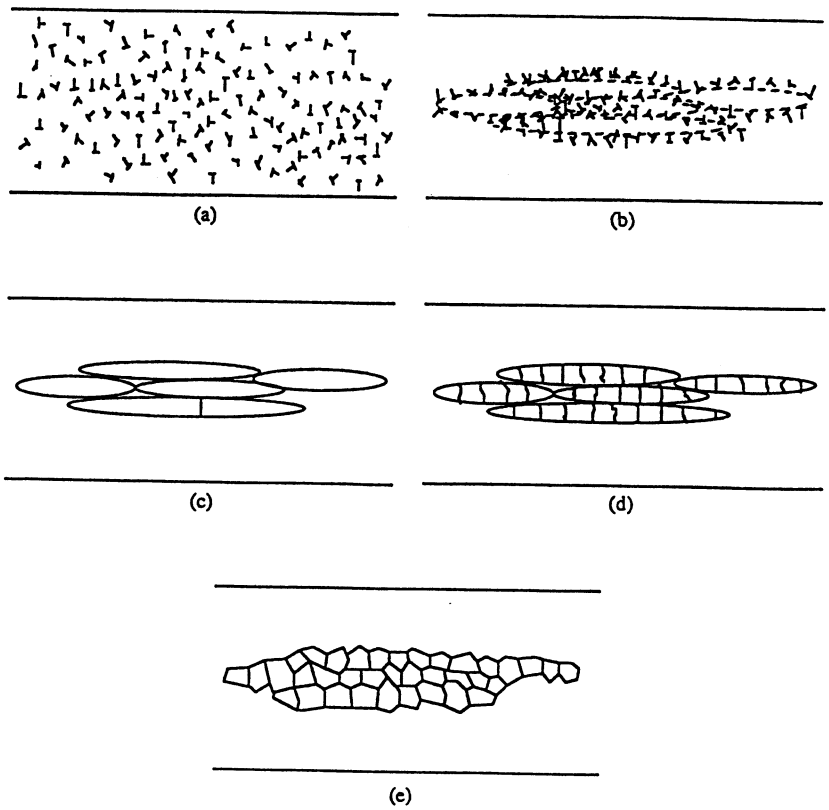

Figure 14.42 Microstructural evolution in high-strain-rate deformation: (*a*) uniform dislocation distribution; (*b*) elongated dislocation cells; (*c*) elongated subgrains; (*d*) elongated subgrain breakup (dynamical recrystallization; (*e*) dynamically recrystallizatized grains (size ~0.1 μm).

(stage 4) as a result of interfacial energy minimization. With continued deformation, these micrograins rotate. Takeuchi and Argon [78] suggested that the subgrain size resulting from high-temperature deformation was related to the applied stress by

$$\frac{\sigma\delta}{\mu b} = K \tag{14.107}$$

where σ = applied stress
δ = subgrain size
μ = elastic shear modulus
b = Burgers vector magnitude
$K \approx 10$ for metals

This is fairly similar to the expression obtained by Tungatt and Humphreys [79]. It is originally due to Sherby and Burke [80] and has its origin in low-temperature, high-stress creep. Derby [77] suggested that it could be applied to rotation recrystallization. For the tantalum used by Chen et al. [6], the parameters are σ = 500 MPa, μ = 69 GPa, and b = 0.2333 nm. This yields a subgrain size of 0.3 μm, consistent with the observations. Thus, one may conclude that dynamic recrystallization by a rotational mechanism takes place in restricted regions of intense deformation (i.e., shear localization regions).

It is possible to analyze the rotational dynamic recrystallization from an energetic viewpoint. The overall energy due to random dislocation distribution (stage 1), dislocation cell formation (stage 2), subgrain formation (stage 3), and micrograin formation (stage 4) can be evaluated. This is described by Meyers et al. [81]. Calculations predict a critical dislocation density, misorientation, and cell sizes, in agreement with experimental observations.

14.6.3 Self-Organization of Shear Localization

Most studies have been concerned with an isolated shear band, whereas the accommodation by internal plastic deformation in response to externally applied tractions takes place by the cooperative initiation and propagation of assemblages of shear bands. Some historical analogy with dislocations (the elementary carriers of plastic deformation at the microlevel) is suitable here. More recent efforts, dealing with self-organization and low-energy configurations of dislocations, are elucidating, in a quantitative manner, the plastic response of materials (e.g., see Kuhlmann-Wilsdorf [82] and Kubin [83]).

A recurrent topic in studies of damage in materials is the question of spacing between damage sites. The ability to predict and possibly control significant features of the failure patterns, such as numbers, sizes, locations, and velocities of residual particles, is dependent on fundamental and quantitative understanding of evolution laws for these localized damage sites. A first step in obtaining an answer would be to estimate the spacing of initial nucleation sites since damage tends to grow in specific places in the material. Of course, this leaves out such questions as secondary damage and subsequent interaction of damage sites, but it is still a crucial beginning.

The analyses carried out by Grady and Kipp [84], Wright and Ockendon [85], and Molinari [86] are theoretical efforts at elucidating the collective behavior of shear bands. The analysis by Grady and Kipp (GK) [84] is based on momentum diffusion as unloading occurs within the band, and the one by Wright and Ockendon [85] and Molinari [86] uses perturbation of rate-dependent homogeneous shearing.

The basic notion, used in the GK analysis, is that rapid loss of strength or ability to transfer shearing stresses across the developing shear band affects neighboring material by forcing it to unload. This concept is similar to the one proposed by Mott [117] in the fragmentation of shells. This unloading process is communicated outward by momentum diffusion, rather than by elastic wave propaga-

tion, and ultimately the minimum separation between independently nucleating bands arises from computing the distance traveled by the unloading front during the time required to unload as localization occurs. Their analysis also assumes that the width of the shear band adjusts itself so as to achieve a maximum growth rate, and that the growth rate of narrower bands are limited by thermal diffusion and that of wider bands by inertia. The details of the analysis are too complex to repeat here, but the predicted spacing, L_{GK}, given in their Eq. (23), with suitable changes in notation (thermal diffusivity χ has been replaced by thermal conductivity divided by density and heat capacity, k/pC), is

$$L_{GK} = 2\left(\frac{9kC}{\dot{\gamma}^3 a^2 \tau_0}\right)^{1/4} \tag{14.108}$$

In this formula the applied shear strain rate is $\dot{\gamma}$, and the relation between flow stress and temperature is assumed to be

$$\tau = \tau_0[1 - a(T - T_0)] \tag{14.109}$$

where τ_0 is the strength at a reference temperature T_0, and a is a softening term. Grady and Kipp did not include strain and strain-rate hardening in their analysis.

On the other hand, the Wright–Ockendon (WO) analysis [85] is based on the notion that shear bands arise from small, but growing disturbances in an otherwise uniform region of constant strain rate. Disturbances do not propagate in perpendicular directions, but simply grow in place, so the most likely minimum spacing is obtained by finding the fastest-growing wavelength. The problem is posed by first finding the uniform fields and then by finding differential equations for perturbations with the uniform fields taken as the ground state. Fourier decomposition of the perturbation equations is followed by an asymptotic representation of the solution. Then it is a simple matter of differentiation to find the wavelength that grows the fastest.

Wright and Ockendon [85] assumed the following constitutive equation, which has both termal softening and strain-rate hardening components:

$$\tau = \tau_0[1 - a(T - T_0)]\left(\frac{\dot{\gamma}}{\dot{\gamma}_0}\right)^m \tag{14.110}$$

where $\dot{\gamma}_0$ is a reference strain rate, m is the strain-rate sensitivity, and τ_0 is the flow stress at the reference temperature T_0 and strain rate $\dot{\gamma}_0$.

Wright and Ockendon [85] arrived at an expression for the wavelength providing maximum growth of the perturbation. This yields a shear band spacing L_{WO}, equal to

$$L_{WO} = 2\pi \left(\frac{kCm^3 \dot{\gamma}_0^m}{\dot{\gamma}^{3+m} a^2 \tau_0} \right)^{1/4} \tag{14.111}$$

The WO analysis was expanded by Molinari [86] by incorporating work hardening into the constitutive equation. This more elaborate analysis predicts shear band spacings that are lower than the ones for our ideally plastic material.

The foregoing analysis is given by Nesterenko et al. [87,88] who carried out experiments with titanium and stainless steel, using the symmetric radial collapse of a thick-walled cylinder at high strain rates (10^4 s^{-1}). The inner wall of the cylinder undergoes the highest strain, which decreases toward the outside. The results are surprisingly reproducible and clearly show the self-organization in the initiation and propagation of shear bands. The shear bands follow a logarithmic spiral trajectory, dictated by the maximum shear stresses. Figure 14.43 shows the regular spacing of shear bands; in Figure 14.43*a* an optical micrograph reveals the bands, whereas tracings are shown for titanium and 304 stainless steel (SS) in Figure 14.43*b*,*c*, respectively.

The experimental results are compared with predictions of two theories, and the experimentally obtained shear band spacings [1 mm (Ti)] are in good agreement with the predictions of Grady–Kipp [1.8 mm (Ti)] and Ockendon–Wright [0.3 mm (Ti)]. It is felt that the OW theory predicts better the shear band spacing if it is mainly determined by the initiation stage, whereas the propagation is affected by the momentum diffusion in the GK approach. Prior to the onset of localization, momentum diffusion is absent, and its role is fully felt only in the propagation stage. The trajectories of the shear bands have been modeled, enabling a prediction of the final configuration in good agreement with observations.

14.7 DYNAMIC FAILURE

Failure can he defined as the separation of a body into two or more parts. Separation requires tension so tensile stresses are important in the production of failure. Dynamic failure can be classified into two groups:

1. *Tensile Failure.* The state of stress and the dynamics of generation, propagation, and interconnection of flaws dictates the morphology. Under uniaxial strain conditions, this failure is called "spalling."
2. *Compressive Failure.* Under compressive traction, localized regions of tension form in the microstructure and cause failure. Pure FCC metals (gold, silver, etc.) are mostly immune to this type of failure, but ceramics, composites, and less ductile metals (e.g., tungsten, steel) can fail this way.

The rest of this chapter will explore the microstructural aspects of these two types of failure mentioned and a few of the mechanical models that have been

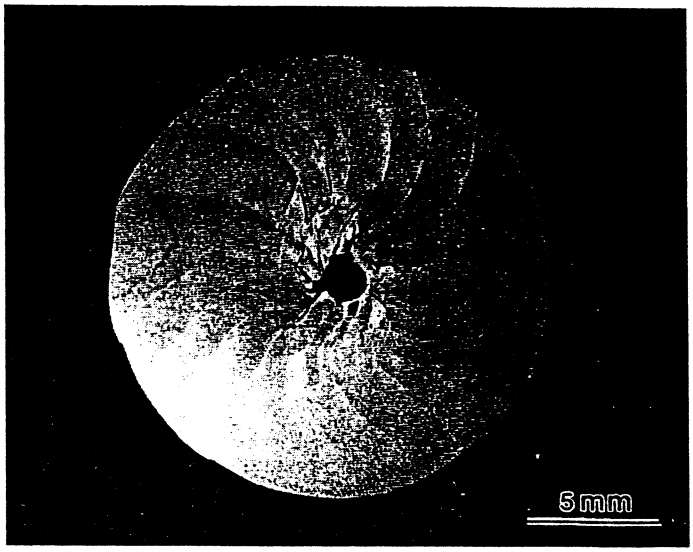

(a)

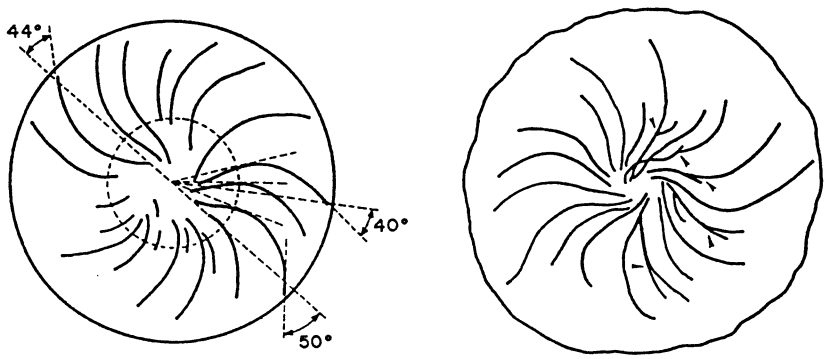

(b) (c)

Figure 14.43 Shear band patterns on cross section of collapsed cylindrical specimens: (*a*) optical micrograph for titanium; (*b*) tracing of shear bands for titanium; (*c*) tracing of shear bands for stainless steel.

developed. It is an impossible task to properly review this extensive field in only a few pages.

14.7.1 Dynamic Failure in Tension

14.7.1.1 Mechanical Modeling

Dynamic failure in tension involves high-velocity crack propagation in brittle materials and rapid void growth in ductile materials. Between a spherical void,

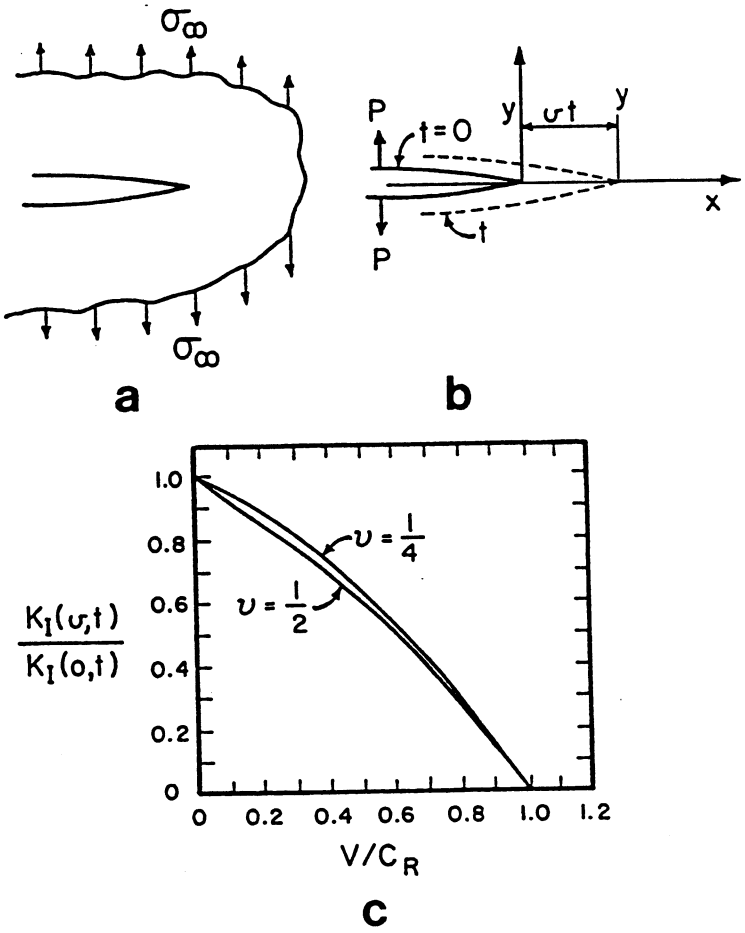

Figure 14.44 (*a*) Loading boundary conditions; (*b*) referential translation in Freund's dynamic crack propagation analysis; (*c*) normalized stress intensity factor as a function of normalized crack velocity (C_R is Rayleigh speed). (Reprinted from L. B. Freund, J. Mech. Phys. Solids, *20* (1972), p. 150, with permission from Elsevier Science.)

for a perfectly ductile material—and an infinitely sharp crack tip—for a brittle material—one can envisage an entire range of phenomena. The limiting velocity of a crack in a brittle material has been calculated by Mott [89], at an elementary level, and more completely by Yoffé [90], Broberg [91], Craggs [92], Baker [93], Achenbach [94], and Freund [3, 95–100]. These different studies use varying boundary conditions and crack sizes. Only the results of Freund's work will be illustrated here. Figure 14.44*a* shows the configuration calculated by Freund [96]: a semi-infinite crack growing at a constant velocity v under a time-independent loading σ_∞ in an elastic material. The solution involves integral equations, the Laplace transform, and the Wiener–Hopf technique, originally

developed for electromagnetic waves. The stress intensity factor at a velocity v, $K_I(v,t)$, is related to the stress intensity factor at rest, $K_I(0,t)$, by

$$\frac{K_I(v,t)}{K_I(0,t)} = \frac{1-(v/v_R)}{1-(v/2v_R)} \tag{14.112}$$

where v_R is the Rayleigh wave velocity. Figure 14.44*c* shows the results for two values of the Poisson ratio ν. The stress intensity factor drops to zero when $v = C_R$, so the Rayleigh wave velocity is the limiting crack velocity. This should be considered as an upper bound, and real materials are subjected to a series of complicating effects that decrease the maximum velocity:

1. Plastic deformation at crack tip, increasing work required for crack propagation
2. Grain boundaries and other barriers and crack-tip deflectors
3. Crack bifurcation at high velocities predicted from the calculations of Yoffé [90] because of the shifting of the maximum principal stress orientation with increasing velocity

Yoffé [90] predicted a shift in orientation with possible bifurcation at $0.5\ C_s < v < 0.8C_s$, where C_s is the shear wave velocity, while Congleton [101] and Shih [102] suggested a value of $0.7\ C_R$. Yoffé attributed the bifurcation of cracks to the compression of the stress field ahead of the crak at high velocities and to the generation of maximum principal tensile stress planes away from the plane of the crack. Ravi-Chandar and Knauss [103] conducted careful experiments that suggest another mechanism for the bifurcation of cracks. The interactions of microcracks in the process zone ahead of a major crack are responsible for bifurcation, according to them.

It is possible, in a unique loading situation, to produce supersonic crack propagation, and this was accomplished by Winkler et al. [104] by laser irradiation of KCl crystals. A plasma, driven down the crack opening, can produce velocities between 10^4 and 10^5 m/s.

The growth of voids involves considerable plastic deformation, and quasistatic void growth models have been developed by McClintock [105,106] and Rice and Tracey [107], among others. Additional efforts by Glennie [108], Rice and Johnson [109], and McMeeking [110] are also noteworthy.

Curran et al. [111] developed a physically based model involving the nucleation, growth, and coalescence of voids in a region undergoing tensile stresses (NAG model). Their approach involves the following expressions for the rate of nucleation N and the rate of growth, R of flaws:

$$\dot{N} = \dot{N}_0 \exp\left(\frac{\sigma - \sigma_{n0}}{\sigma_1}\right) \tag{14.113}$$

$$\dot{R} = \left(\frac{\sigma - \sigma_{g0}}{4\eta}\right) R \tag{14.114}$$

where σ_{n0} = tensile threshold stress
N_0 = threshold nucleation rate
σ_1 = stress sensitivity for nucleation
σ_{g0} = is the tensile stress threshold for void growth
η = crack-tip viscosity
R = crack/void radius

The yield surface for a material containing voids was modeled by Gurson [112] as

$$\frac{3}{2}\,\underset{\sim}{\sigma}' : \underset{\sim}{\sigma}' = \left[1 + \phi^2 - 2\phi \cosh\left(\frac{3P}{2\sigma_y}\right)\right] \sigma_y^2 \tag{14.115}$$

where ϕ = volume fraction of pores
$\underset{\sim}{\sigma}'$ = stress deviator
σ_y = yield stress of the material
P = hydrostatic stress (tensile or compressive)

When $\phi = 0$, it reduces itself to a J_2 flow criterion. Fyfe [113] used the Gurson model to predict dynamic failure by tension in metals. Johnson [114], on the basis of the Carroll–Holt [115] model, developed an analytical treatment for failure under tension and compared his predictions with spalling experiments in copper.

The treatments discussed above deal with individual cracks or voids. When the collective behavior of cracks is considered, different approaches have to be implemented. In spalling, a continuum model was developed by Davison and Stevens [116]. A damage parameter D was defined, varying from 0 (initial undamaged material) to 1 (final spalled material). This damage parameter was analytically expressed as a function of material parameters. For the case of fragmentation produced by tensile stresses, the early theory of Mott [117] was followed by the Grady-Kipp [118] and Grady [119] approaches, which led to the determination of fragment size as a function of strain rate. Bai, Ke, and coworkers [120–122] have developed a statistical model of microcrack generation, extension, and interconnection.

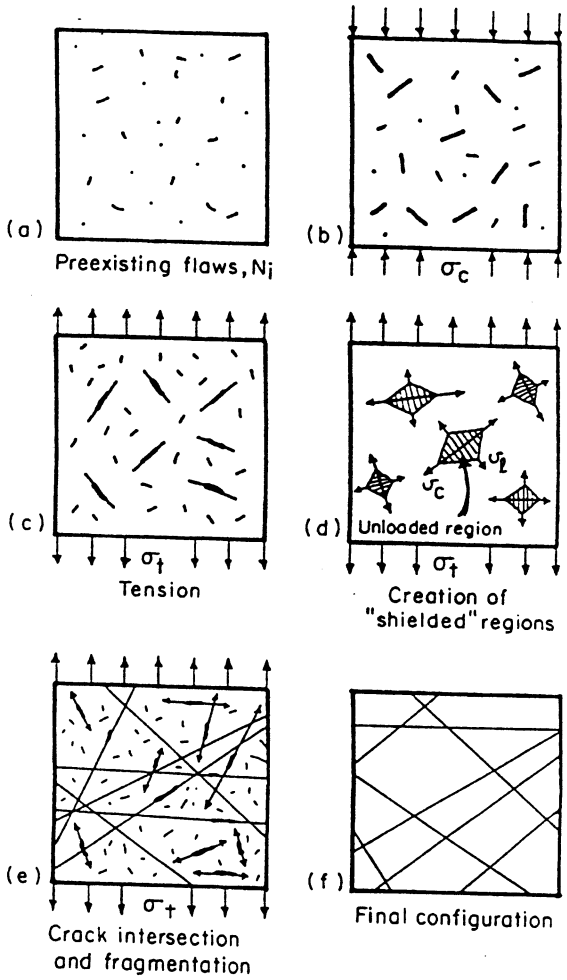

Figure 14.45 Different stages in fragmentation of brittle material due to stress wave loading: (*a*) initial, preexisting flaws; (*b*) compressive loading and stable growth of flaws; (*c*) tensile loading; (*d*) growth of cracks and intersection of free surfaces; (*e*) unloading of region surrounding crack growth.

Louro and Meyers [123,124], from observations in alumina, developed a model for the prediction of the fragment size in a specimen subjected to sequential compressive and tensile loading. The compressional portion of the loading pulse (and this will be discussed in Section 4) activates flaws and creates cracks, which then grow at high velocities during the tensile portion of the pulse. Figure 14.45 shows the four different stages of fragmentation. Existing flaws (*a*) are activated by compression, (with size $a > a_c$), and new flaws are generated (*b*). On tensile loading (*c*), the flaws will grow at velocities dictated by the crack

dynamics equations. These cracks intersect each other (*d*), forming fragments. Each growing crack generates an unloaded region (shown hatched in Figure 14.45*e*) in which no subsequent flaw activation takes place. A simplified analysis was developed by Louro and Meyers [124]. The crack velocity V_c was assumed to be limited by the Rayleigh wave velocity C_R as

$$V_c = C_R[1 - e^{\alpha(K_I^2 - K_{Ic}^2)}] \tag{14.116}$$

K_{Ic} and K_I are the critical and current values of the stress intensity factor, respectively. By considering flaws that were critical at the onset of tension, N_i, and flaws that were activated during tension, N_v, Louro and Meyers [124] developed a general expression for the crack surface per unit volume as a function of time, stress, and microstructure. The nucleation rate $\dot{N}_v$ was corrected continuously for the unloaded volume created by the growing cracks.

14.7.1.2 Microstructural Aspects

The microstructural aspects of dynamic fracture by spalling are extensively discussed by Meyers and Aimone [125] and Zurek and Meyers [126], among others. The response of materials is complex and is dictated by the existing microstructure and its evolution during shock loading and/or in high-strain-rate loading. A wide variety of effects occur, and some of them will be illustrated in this section. We will first review brittle materials, and then ductile materials. A very important aspect of damage is the level at which we are observing it; this level can be, somewhat arbitrarily, classified into microscale, mesoscale, and macroscale. Roughly, these scales correspond to observations as follows:

Microscale: scanning and transmission electron microscopy
Mesoscale: optical microscopy
Macroscale: naked eye

One phenomenon of great importance is the dependence of fragment size (for a brittle material) on the strain rate. Results by Field and co-workers [127] are shown in Figure 14.46 for a ceramic impacted at different velocities: 35.6, 46, 76.2, 97.4, and 138 m/s. As the impact velocity is increased, the fragment number increases. A simple Hertzian cone is produced at 35.6 m/s, whereas fine comminution results from the 138-m/s impact. These results are in accord with the Grady–Kipp [118], Grady [119], and Louro–Meyers [123,124] formulations, as well as a significant amount of additional experimental results. Figure 14.47 shows the formation of microcracks in alumina dynamically loaded in tension. In Figure 14.47*a* the cracks gave rise to the microcracks, whereas in Figure 14.47*b* these microcracks were formed at the grain boundaries and are marked by arrows. These results by Louro and Meyers [128] are consistent with experimental observations by Longy and Cagnoux [129] as well as Cosculluela et al. [130,131]. Figure 14.48 shows the effect of microstructural parameters, such as

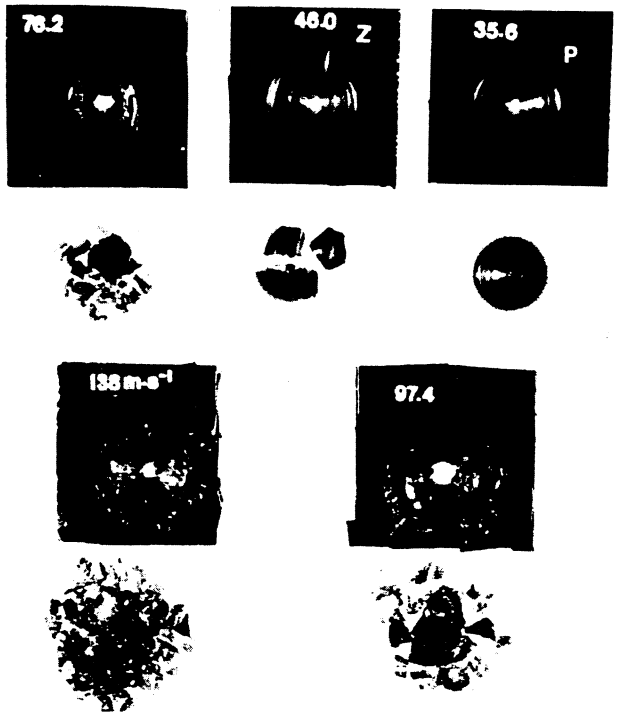

Figure 14.46 Formation of ejection cone and fragmentation due to impact of glass by spherical projectile at different velocities (marked in m/s). (From J. Field [127], Fig. 21.)

grain size, on dynamic fracture of alumina. Under identical loading conditions [53], alumina with a grain size of 24 μm exhibited less macrocracking than did alumina with a grain size of 4 μm. The interpretation given by Louro and Meyers [128] to this effect is that these were fewer grain boundaries in the 24-μm alumina; the grain boundaries (Fig. 14.48*b*) are sources of cracks.

In metals one can have both brittle and ductile fracture under tension, and the transition from ductile to brittle behavior in steels is dictated by both temperature and strain rate. This response is rooted in dislocation dynamics, as described by Meyers [2]. This transition has a very significant effect on the high-strain-rate fracture of steels, which occurs at a lower stress intensity factor than low-strain-rate fracture. The analysis by Follansbee and Zurek [132] addresses this effect. Another phenomenon of great importance in steels is the drastic change of morphology that occurs when shock pressure (which precedes spalling) exceeds 13 GPa. When this occurs, the spall morphology changes drastically. This phenomenon was first observed by Ivanov and Novikov [133]. Figure 14.49 shows low-magnification scanning electron micrographs of smooth [$P > 13$ GPa (*a*)] and rough [$P < 13$ GPa (*b*)] spalls. On visual observation,

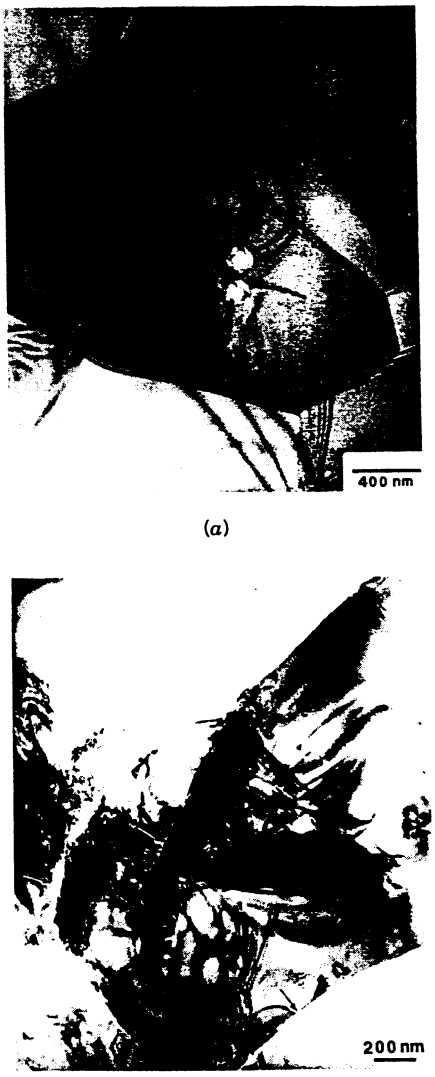

Figure 14.47 Flaws generated in Al_2O_3 subjected to dynamic tension: (*a*) cracks at voids; (*b*) cracks at grain boundaries.

the smooth spall appears as flat as a machined surface. A higher magnification observation of these two morphologies is shown in Figure 14.50 for an AISI 4340 steel. The fracture produced at 10 GPa is brittle. The fracture produced above the 13-GPa threshold is ductile. The explanation provided by Zurek et al. [125] for this phenomenon is that the preshocking of the material to $P > 13$ GPa generates a large concentration of defects, which can then nucleate voids

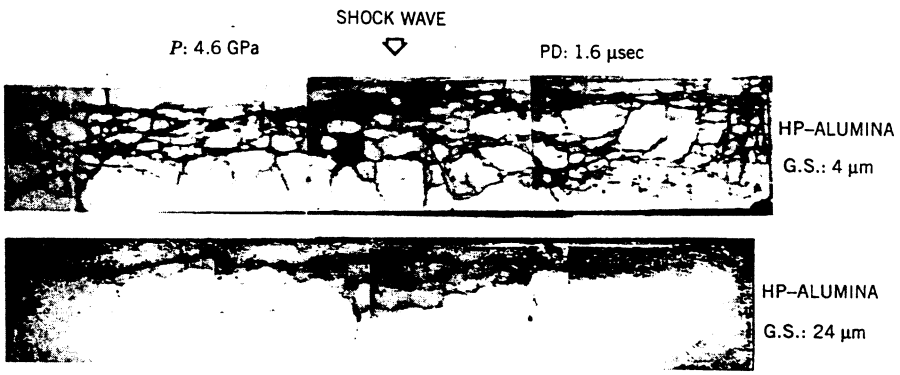

Figure 14.48 Cross sections of Al_2O_3 disks impacted by flyer plate technique encapsulated in Al containers; $P = 4.6$ GPa; pulse duration = 1.6 μs. (From Louro and Meyers [128].)

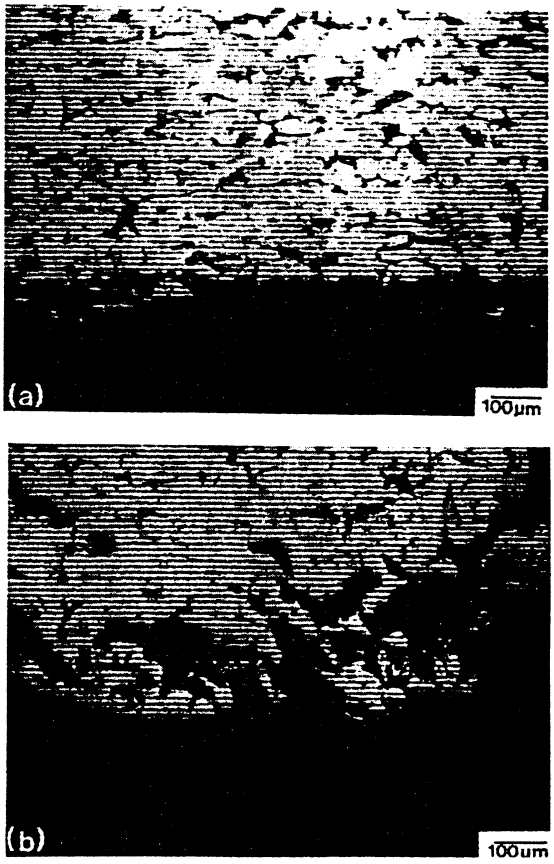

Figure 14.49 Scanning electron micrographs of spall surfaces in steel: (*a*) smooth spall; (*b*) rough spall. (From Meyers and Aimone [126].)

(*a*)
Brittle Fracture
10 GPa

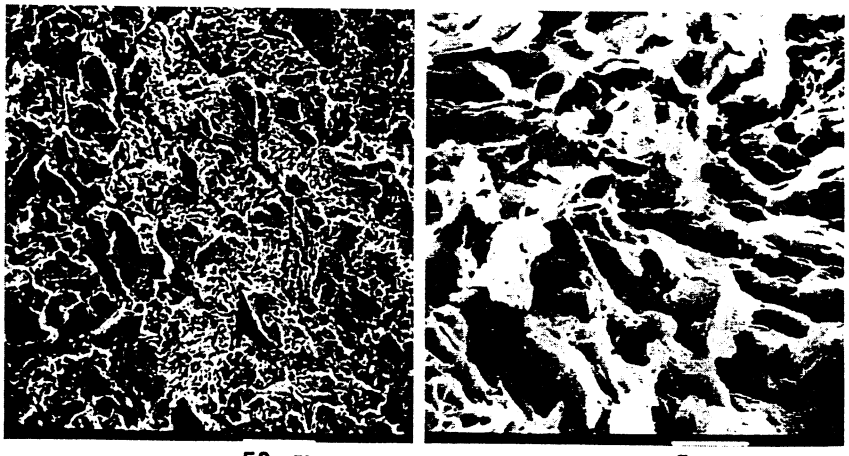

(*b*)
Ductile Fracture
15 GPa

Figure 14.50 Effect of impact pressure on morphology of spall fracture: (*a*) brittle fracture, P = 10 GPa; (*b*) ductile fracture, P = 15 GPa. (Courtesy of A. K. Zurek.)

on being subjected to the tensile pulse. The shift from brittle to ductile response in steels can be produced by a decrease in grain size, an analogous response.

The ductile response of metals involves considerable plastic deformation; Figure 14.51*a* shows a transmission electron micrograph of a void in copper [135]. It is surrounded by a large dislocation density evidenced by the dark region surrounding the void edges. This plastic deformation is necessary for void growth and is an intrinsic component of the plasticity models described in Section 14.2.1. Slip is also evident in Figure 14.51*b*, which shows an intergranular void and the dislocation activity associated with its growth. The nucleation

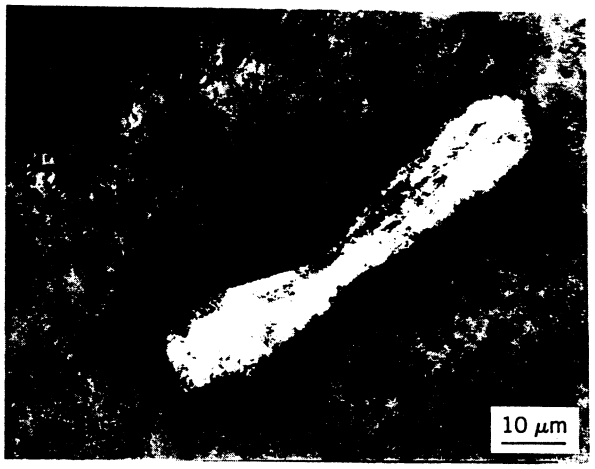

(*a*)

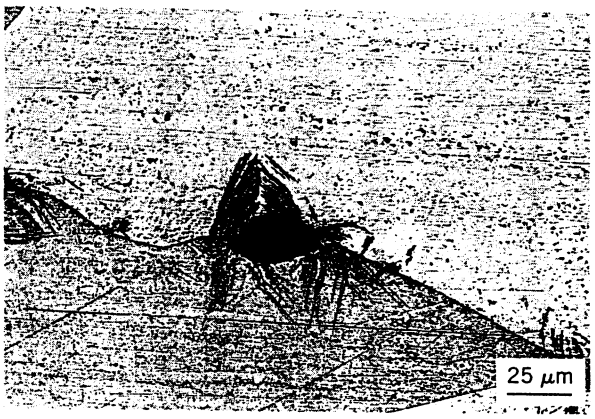

(*b*)

Figure 14.51 Voids in copper: (*a*) peanut-shaped void viewed by high-voltage (1-MeV) transmission electron microscopy; (*b*) grain boundary void with associated slip traces.

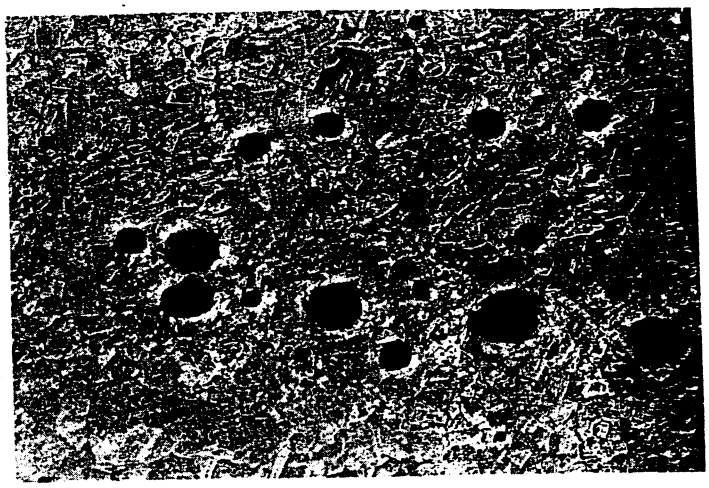

(*a*)

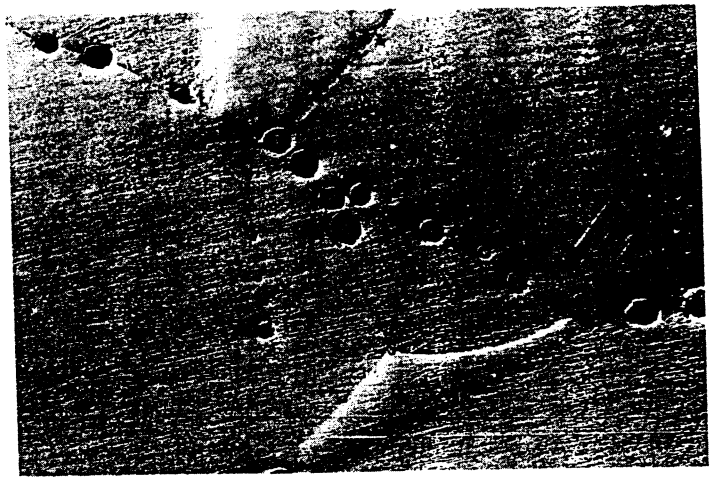

(*b*)

Figure 14.52 Effect of grain size on void distribution in copper: (*a*) specimen with grain size = 20 μm; (*b*) specimen with grain size = 250 μm.

of voids in copper is dependent on microstructural scale parameters. If the grain size is small (Figure 14.52*a*), the nucleation occurs homogeneously throughout the material. For large grain sizes, nucleation occurs primarily along the grain boundaries, yielding the characteristic morphology of Figure 14.52*b*. The section through a copper specimen subjected to a tensile pulse of 3 GPa is shown in Figure 14.53. The right-hand side of the figure shows the etched microstructures. The nucleation, growth, and coalescence of voids at grain bound-

Figure 14.53 Cross section of copper specimen impacted by planar–parallel flyer plate, generating pressure of 3.5 GPa: (*a*) unetched specimen; (*b*) etched specimen.

aries is obvious. Kanel et al. [136] showed that the spall strength of monocrystalline copper was higher than that of polycrystalline copper. This is contrary to their quasi-static properties and an indication that the threshold stress for grain boundary nucleation is lower than for homogeneous nucleation. These results show that the morphology of the fracture is determined by the density and spatial distribution of nucleation sites.

The flow stress of the matrix depends on strain rate, as discussed in Section 14.3. Nucleation of voids due to plastic deformation (at grain interior) and in the grain boundaries are competing processes; at low strain rates, the former dominates, while at higher strain rates, the latter becomes effective. The grain-boundary nucleation sites become more effective as the grain size increases; the total interfacial area decreases with increasing grain size, and, at a constant

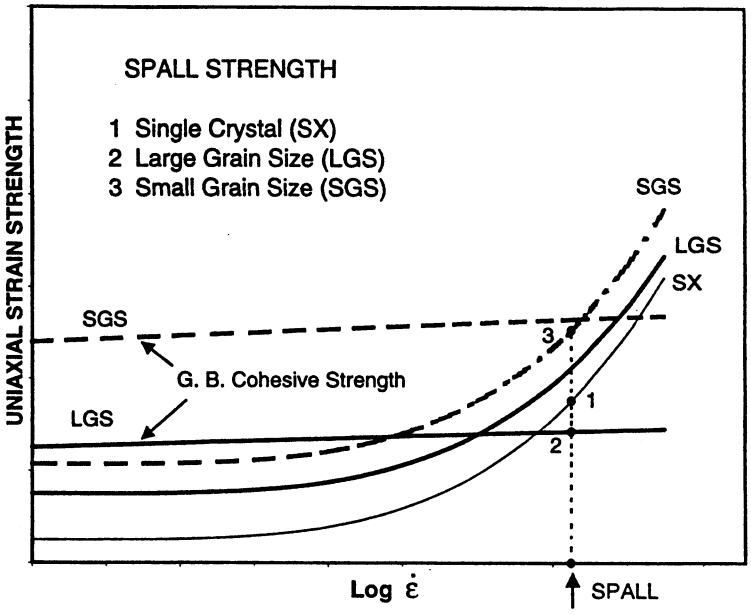

Figure 14.54 Qualitative explanation for anomalous effects observed in the spalling of copper.

impurity content, their concentration at the boundaries increases with grain size. Thus, the transgranular/intergranular transition, as the grain size is increased, in spalling of copper. Figure 14.54 shows schematically, the competing effects of the grain-boundary cohesive strength and flow strength of the matrix. This is also discussed in Section 14.7.2 (Compressive Strength of Tungsten). Impurities segregate at the grain boundaries, weakening them. This effect is more pronounced the larger the grain size: the impurity concentration being constant, its segregation at the grain boundaries increases with increasing grain size. There is no reason to believe that the grain boundary cohesive strength is highly sensitive to strain rates. The two plots, for a large-grain-sized (LGS) and a small-grain-sized (SGS) specimen are shown in Figure 14.54. At low strain rates, the plastic flow of the matrix, and the associated void-opening initiation (see Gurson) require less stress than grain-boundary decohesion. As the strain rate is increased, a reversal of roles occurs. At the strain rate characteristic of spalling, specimen LGS fails by grain-boundary separation, whereas specimen SGS fails by matrix flow. This is schematically shown in Figure 14.54, which also shows the spalling strength of the single crystal (SX), which has no grain boundaries. Hence, SX has a higher spall strength than LGS.

Another clear example of a material with preferential nucleation sites at grain boundaries is shown in Figure 14.55*a*. This Fe–30% Ni alloy contains a grain boundary precipitate (brittle carbide) that gives origin to debonding without

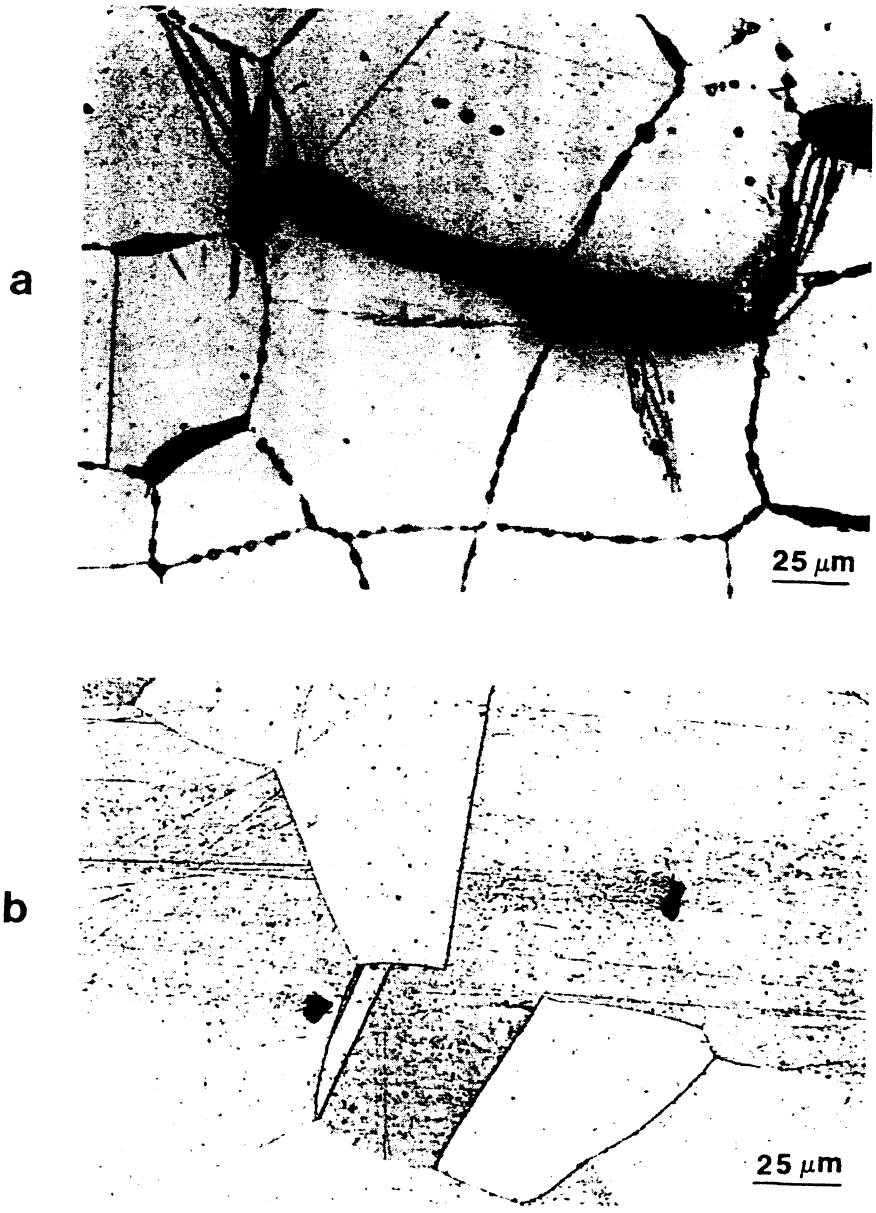

Figure 14.55 Incipient spalling in (*a*) Fe–30% Ni alloy, creating grain-boundary separation; (*b*) Ni, forming voids with facets.

appreciable plastic deformation. Figure 14.55*b* shows voids within the grains; they have geometric shapes that are due to the anisotropy of the flow stress (in this case, of Ni).

The morphology and breakup of voids in a dynamic tension region can lead to interesting morphologies, and one of them is shown in Figure 14.56*a*. The voids appear to circle a region that therefore undergoes a rotation. Benson [137] also obtained these "void sheets," which constitute boundaries for the domain. The evolution of one such a void agglomeration is shown in Figure 14.56*b*. This is the result of a hydrocode computation for AISI 4340 steel.

14.7.2 Dynamic Failure in Compression

14.7.2.1 Failure Mechanisms

Whereas ductile metals can undergo large compressive strain without failure, in brittle materials (ceramics, rocks, intermetallic compounds, and brittle metals such as cast iron) flaws are generated under compressive stresses. It should be clarified that the remote compressive tractions cause, by virtue of microstructural inhomogeneities, localized regions of tension, which in turn, lead to crack initiation. Thus, microstructural effects are responsible for cracking under compression. Examples of microstructural inhomogeneities that can nucleate cracks under compression are:

- Voids, around which tensile stresses are generated by compression. These voids can have all kinds of shapes, but spheres and ellipsoids are idealized configurations that lend themselves to mathematical analyses predicting localized regions of tension.
- Boundaries between grains in materials having elastic anisotropy in such a manner that elastic incompatibility stresses are generated.
- Brittle grain boundary phases that may fracture under shear resulting from compression. An example is the glassy grain boundary phase in commercial alumina. Ceramics often contain these phases, which are due to the sintering agents that are added to material to facilitate densification during processing.
- Second-phase particles that may have different compressibilities than the matrix, leading to crack nucleation at the interface.
- Destruction of coherency between the matrix and second phases due to differences of elastic properties.

Figure 14.57 shows the three principal mechanisms of compressive failure in a schematic fashion. Spherical voids lead to tensile stresses when loaded in compression. This problem was first solved analytically by Goodier [138], and the maximum normal tensile stress is equal to (for uniaxial stress loading):

(a)

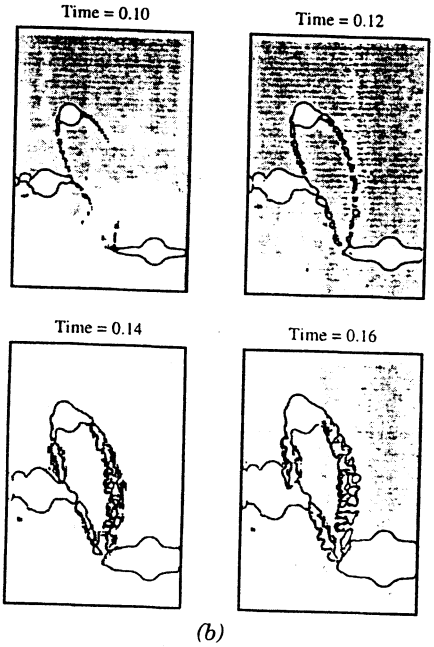

(b)

Figure 14.56 Void sheets forming circular features in spall region: (*a*) microstructural observation in copper; (*b*) hydrocode computation by D. J. Benson. (Courtesy D. J. Benson).

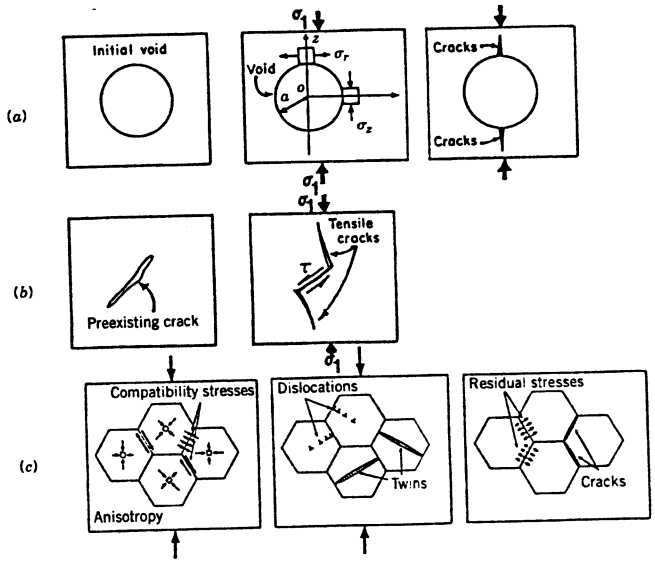

Figure 14.57 Different mechanisms for crack formation in compressive loading of brittle materials.

$$\sigma_{\theta\theta}^{0} = -\frac{3}{2}\frac{(1+5\nu)}{(7-5\nu)}\sigma_1 \approx -\frac{1}{2}\sigma_1 \tag{14.117}$$

where σ_1 is the compressive traction (which is negative). When lateral confinement is incorporated, the expression has to be modified. Sammis and Ashby [139] provide a detailed treatment. A generalization of the spherical void is the elliptical void, which represents a flaw of a more general shape. This was, apparently, first treated by Griffith [163], and analytical solutions are obtained by Brace and Bombolakis [140], Adams and Sines [141], Horii and Nemat-Nasser [142], and Ashby and Hallam [143]. Figure 14.57*b* shows this configuration (see also Fig. 14.65*a*). If ψ is the angle of the flaw plane with the compressive axis, and μ is the friction coefficient of the walls of the flaw, the maximum stress intensity factor at the tip of flaw can be expressed as [143]

$$K_I = -\sigma_1\left(\frac{\pi a}{3}\right)^{1/2}\left[\left(1-\frac{\sigma_3}{\sigma_1}\right)(1+\mu^2)^{1/2} - \left(1+\frac{\sigma_3}{\sigma_1}\right)\mu\right] \tag{14.118}$$

where σ_1 is the compressive traction (negative) and σ_3 is the lateral confinement. This maximum occurs for the orientation

$$\psi = \frac{1}{2}\tan^{-1}\frac{1}{\mu} \tag{14.119}$$

Nemat-Nasser and Deng [144] and Ravichandran and Subhash [145] considered an array of wing cracks (shown in Fig. 14.57*b*) in a ceramic subjected to compression. They obtained closed-form solutions for the ceramic, for dynamically growing interacting and noninteracting cracks, respectively. They applied a form of the above equation to these cracks, varying both the stress state (uniaxial stress and strain) and strain rate $\dot{\epsilon}$. Lateral confinement (represented by uniaxial strain) is very important and increases the compressive strength. The microstructural parameters were introduced through the crack length $2a$ and spacing $2w$. The failure stress, which was dependent on a, w, $\dot{\epsilon}$, and stress state, was observed to increase significantly in the 10^4–10^6 s^{-1} range.

The third mechanism of flaw formation due to compression is shown in Figure 15.57*c*. It is due to the anisotropy of elastic properties of grains, and to generation of dislocations and deformation twins, during loading. Internal stress gradients are generated by these effects. These stresses can generate cracks, on unloading, when the stress concentrations act on the grain boundaries.

In Chapter 1, Figure 1.3 shows a computation demonstrating how differences in stiffness can generate internal tensile stresses. Figure 14.58 shows the stresses predicted from a finite-element analysis performed, in plane strain, on a hexagonal grain and its surroundings. This configuration represents SiC, which has one hexagonal structure and effective Young moduli which vary between 375 and 475 GPa, depending upon the orientation. The hexagonal grain represents a compliant region (E = 375 GPa) whereas the material surrounding it represents the stiffest orientation (E = 475 GPa). The stresses parallel and perpendicular to the loading direction are shown in Fig. 14.58*b* and 14.58*c*, respectively. The stresses σ_{22} are compressive over the entire specimen and approximately equal to the applied compressive stress of 4 GPa. The stresses σ_{11}, on the other hand (Fig. 14.58*c*), vary considerably throughout the specimen. There is a region in which σ_{11} is tensile (>0); it is marked by hatching. Its maximum value is 0.2 GPa. This large stress can be responsible for the initiation of cracking. In the configuration shown in Fig. 14.58, a transgranular crack can be generated, as shown in Fig. 14.58*d*.

Figure 14.59 shows a dislocation pile up at a boundary and the subsequent incorporation of the dislocations into the boundary, forming a wedge-shaped crack; this type of crack is called a Zener-Stroh crack. In ceramics, the stress concentrations due to pile ups are not easily relieved by plastic deformation in other slip systems; additionally, the grain boundaries have often a lower strength than the grain interiors. Hence, the Zener-Stroh mechanism is prevalent in creating microcracks, which, upon continued loading, develop into intergranular cracks. Lankford [146] has shown that flaws can appear in ceramics when loaded to a fraction of the fracture stress. Louro and Meyers [126] have shown that dislocation activity was present in a small fraction of the grains in alumina,

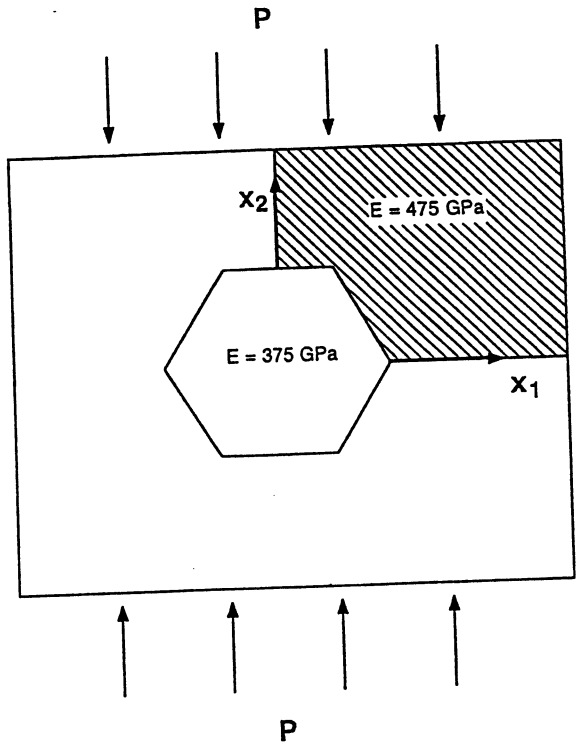

(*a*)

Figure 14.58 Finite element computation of stresses generated by compressive tractions on a representative volume element of a SiC polycrystal; (*a*) representative volume element and loading; (*b*) σ_{22}; (*c*) σ_{11}; (*d*) possible configuration for cracks. (From J. Shih, M. A. Meyers, V. F. Nesterenko, and Chen. Acta Mat. to be published, 1999).

when loaded below the Hugoniot elastic limit (HEL).

A dislocation pileup can generate high tensile stress at a grain boundary. Thus, when the material in unloaded, these tensile stresses can generate grain boundary fracture. The normal stress parallel to the Burgers vector of a dislocation is

$$\sigma_{11} = -\frac{Gb}{2\pi(1-\nu)} \frac{x_2(3x_1^2 + x_2^2)}{(x_1^2 + x_2^2)^2} \tag{14.120}$$

A pileup of n dislocations generates a stress, as shown by Eshelby [147] and Stroh [148], of $n\sigma_{11}$. This superdislocation is situated at $l/4$ from the pileup head, where l is the distance from source to head. If the grain size is D, the distance x_1 is $D/8$, and the tensile stress acting on the boundary is

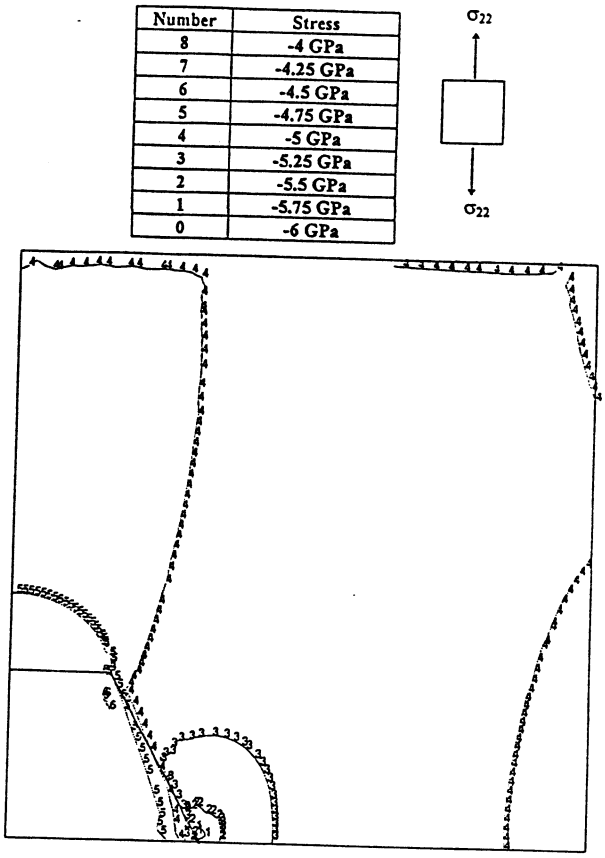

(*b*)

Figure 14.58 (*Continued.*)

$$\sigma_{11} = \frac{4nGb}{\pi(1-\nu)D} \tag{14.121}$$

Here, x_2 was assumed to be equal to $-x_1$. For alumina, a typical ceramic (G = 163 GPa; $\nu = 0.23$; $b = 0.476$ nm), and $D = 10\ \mu$m ($x_1 = 1.2\ \mu$m); thus the tensile stress is approximately $12.6n$ MPa. Hence, a pile up with thirty dislocations ($n = 30$) can generate a tensile stress of 380 MPa; this is the tensile strength of alumina.

Rocks can be envisaged as ceramics with large defects and considerable porosity. Micro, meso, and macrocracks abound, and two or more phases are often present. The grain sizes are characteristically in the mm range. Thus, the study of the dynamic behavior of rocks can elucidate fundamental mechanisms

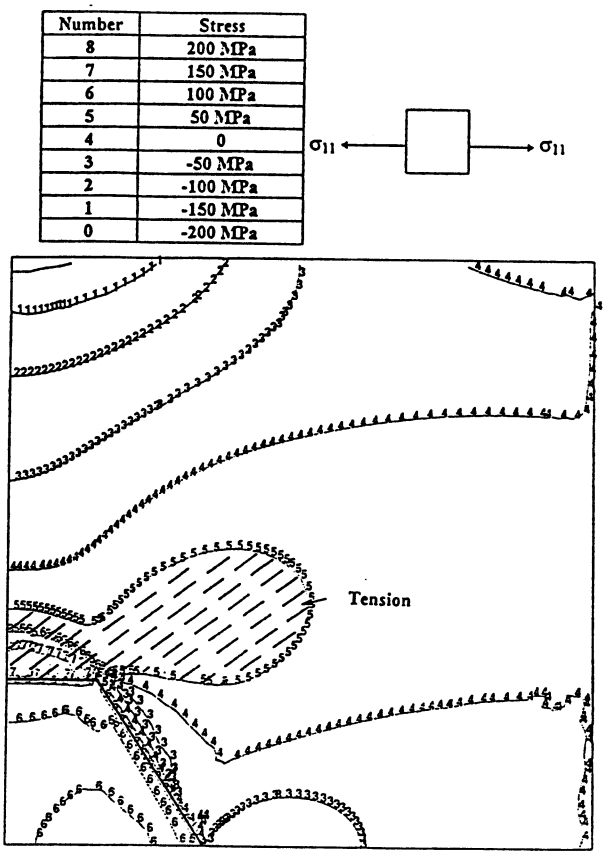

(c)

Figure 14.58 (*Continued.*)

of deformation and failure. A fundamental energy-based analysis was developed by Grady [149]: the basic precept is that there is a balance between the surface energy (generated by fragmentation) and the local kinetic or inertial energy. The following expression was obtained for fragment size, d:

$$d = \left[\frac{(20)^{1/2} K_{IC}}{\rho v_\ell \dot{\epsilon}} \right]^{2/3}$$

This expression was successfully applied to oil shale.

Experiments by Aimone, Meyers, and Mojtabai [150] on a quartz monzonite rock subjected to a uniaxial strain plane compression pulse showed that:

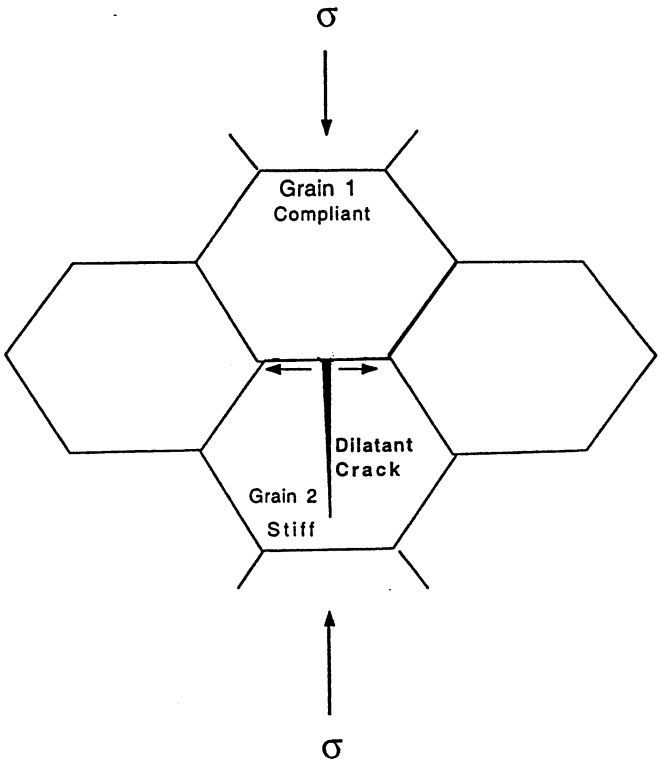

(*d*)

Figure 14.58 (*Continued.*)

1. The mean fragment size decreases with increasing pulse duration at constant pressure, and with increasing pressure at constant pulse duration. This is shown in Figure 14.60*a* for quartz monzonite copper porphyry subjected to different shock-wave pulses.

2. The internal damage generated in rocks by the passage of a shock wave is much larger than the damage simply observed by the fragments. The total surface area of cracks generated internally is higher, by at least one order of magnitude, than the surface area of the observed fragments. This can be verified by converting the internal damage into an "equivalent fragment size." This was accomplished by using the expression $D = 6/S_v$. Figure 14.60*b* shows the measured surface area per unit volume (total area of cracks). The "equivalent" particle size is shown in Fig. 14.60*c*. The differences in particle size between Figs. 14.60*a* and *c* are of the order of magnitude 10^2. Thus, a great portion of the damage remains hidden inside the fragments.

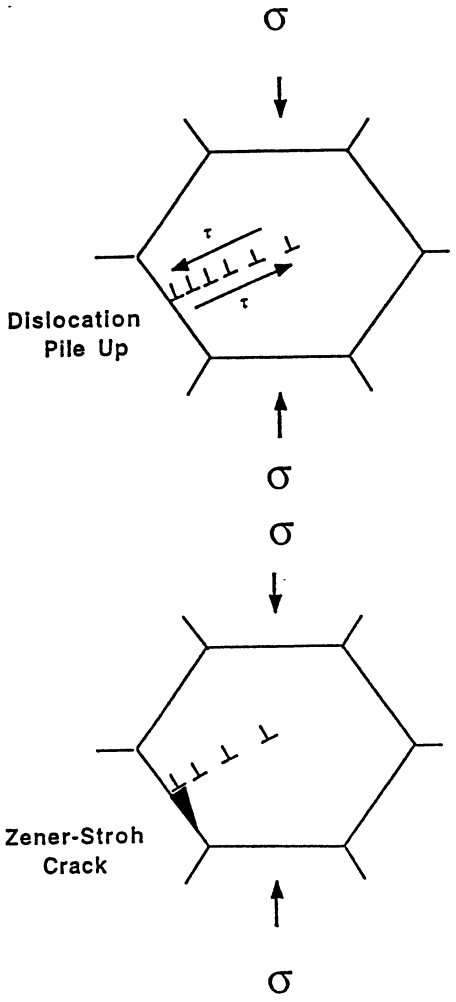

Figure 14.59 (*a*) Dislocation pile-up at a grown boundary; (*b*) pile-up incorporation into grain boundary and formation of Zener-Stroh crack.

The time dependent failure of rocks is consistent with the concepts of nucleation, growth, and coalescence. If a description of how a shock wave propagates through a rock is attempted, it has to incorporate these effects. The energy dissipated by the wave in the fragmenting rock or ceramic is associated with the following energy storage mechanisms: generation of cracks, possible phase transformation, twinning, interfacial defects, sliding of the crack surfaces, porosity collapse, and dislocation motion; of these, the energy expenditure associated with pore collapse is the highest dissipative component in rocks.

There have been reports of a failure wave propagating in glass and ceramics

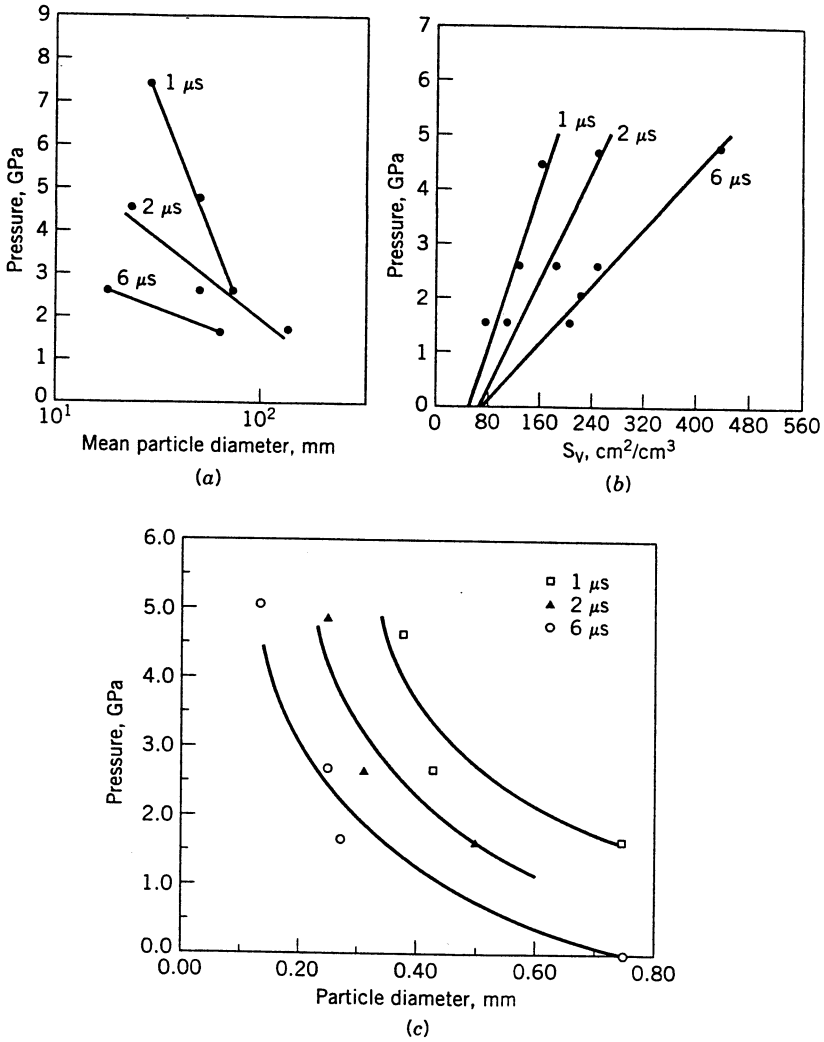

Figure 14.60 Effect of pressure and pulse duration on fragmentation of quartz monzonite loaded in compression: (*a*) mean particle diameter as measured by physical particle separation (sieving); (*b*) surface over per unit volume, S_v, measured from measurement of microcracks on sectioned specimens; (*c*) "virtual" particle diameter, obtained by converting S_v into a particle size through $d = 6/S_v$.

when impacted at high velocities. These reports by Kanel et al. [151] have been confirmed. Raiser and Clifton [152,153] observed the failure wave in glasses, Clifton [154] developed a theory. Experimental results by Senf and Strassburger [155] seem to indicate that this failure wave is the result of the activation of flaws by either the longitudinal or shear wave.

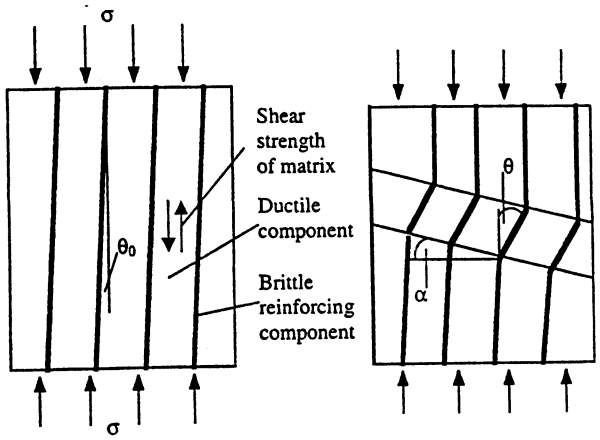

Figure 14.61 Plastic microbuckling (kinking) in composite subjected to compression along fiber/lamella axis (Adapted from Menig et al. [161]).

Johnson and Holmquist [156] and Cosculluela [130,131] have developed constitutive models that describe brittle materials under compressive loading.

The failure of composites under dynamic compressive loading has been discussed by Harding [154]. Composites have a complex response, which is not treated in this chapter because of lack of space.

Plastic microbuckling [158–160] is one important compressive failure mechanism in composites, when the fibers, or lamellae, are oriented with the compression axis. This phenomenon, first analytically modeled by Argon [158], is shown schematically in Fig. 14.61. The fibers undergo a "kinking" which reduces the overall deformation energy. Argon [158] developed a formalism for the calculation of the compressive strength of laminates based on kinking, or plastic microbuckling. The angle α (see Fig. 14.61(a)) is approximately 45°, and the strength of the composite is given by:

$$\sigma \cong \frac{\tau}{\theta_0}\left[1 + \frac{bG_c\Delta\theta}{2\pi a\tau(1-\nu)}\ln\left(\frac{2\pi a\tau(1-\nu)}{bG_c\Delta\theta}\right) + \frac{E_r\Delta\theta}{48\tau}\left(\frac{t_r}{b}\right)^2\right] \qquad (14.122)$$

where τ = shear strength of the matrix

θ_0 = angle between the reinforcement and the loading axis (see Fig. 14.61(a))

E_r = Young's modulus of the reinforcement

t_r = lamella thickness

G_c = shear modulus of the composite

ν = Poisson's ratio

and 2(a) and 2(b) are the kink nucleus dimensions. When $\Delta\theta \rightarrow 0$, at the onset of collapse, the second and third terms in Eq. (14.122) reduce to zero and the equation simplifies to:

$$\sigma \cong \frac{\tau}{\theta_0} \tag{14.123}$$

This analysis has been followed by significant advances due to Evans and Adler [159], and Fleck et al. [160]. This is one of the mechanisms of composite failure, and strain rate effects have not been investigated, heretofore. Menig et al. [161] observed this phenomenon in abalone shell subjected to compressional (both static and dynamic) testing.

14.7.2.2 Compressive Failure of Tungsten

The results obtained by Dümmer et al. [162] on tungsten subjected to compression loading are an excellent illustration of the dramatic effect that the strain rate can have on the failure mechanisms and ductility of a material. Tungsten is known to undergo a ductile-to-brittle transition as the temperature is lowered or the strain rate is increased. It will become clear, from the description presented, how this happens. Figure 14.62 shows representative areas from longitudinal sections for tungsten (annealed at 2600°C) and deformed quasi-statically (10^{-3} s^{-1}) to a strain of approximately 0.25 and dynamically to a strain of 0.052 at a strain rate of 10^3 s^{-1} (loading direction is top to bottom). The amount of damage accumulated within the specimen tested dynamically (Fig. 14.62*b*) is much higher than for the one deformed quasi-statically (Fig. 14.62*a*). Notice that the strain in the specimen deformed dynamically is one fourth of the quasi-statically deformed specimen. The damage occurs primarily as grain boundary debonding, which is caused by impurity segregation; primarily intergranular cracks characterize the annealed material. An axial macrocrack is indicated by arrow 1. The right of the image shows misaligned microcracks that are frequently related to twin-grain-boundary intersections (arrows 2). For the quasi-statically tested specimen, the shape of the stress-strain curves and the presence of low damage after straining above 0.20 indicates a typical ductile process. Figure 14.63 provides a quantitative analysis of crack density for the two strain rates. These results show that the damage by micro- and macrocracking increases with increasing strain and strain rate.

The evidence for a wing-crack formation mechanism in W is shown in Figure 14.64, taken from the longitudinal section of the sample that was deformed to a strain of 0.05 at a rate of 10^3 s^{-1}. Two grain-boundary debonds nearly parallel to the loading axis (marked by arrows 3) are linked by a third tilted debond (marked by 1). The step in the plane of the tilted crack (marked by 2) reveals the sliding displacement between the adjacent grains. It is noted that this displacement was initially prevented by the cohesive strength of the grain boundaries that finally separated. Furthermore, it is seen that the displacement

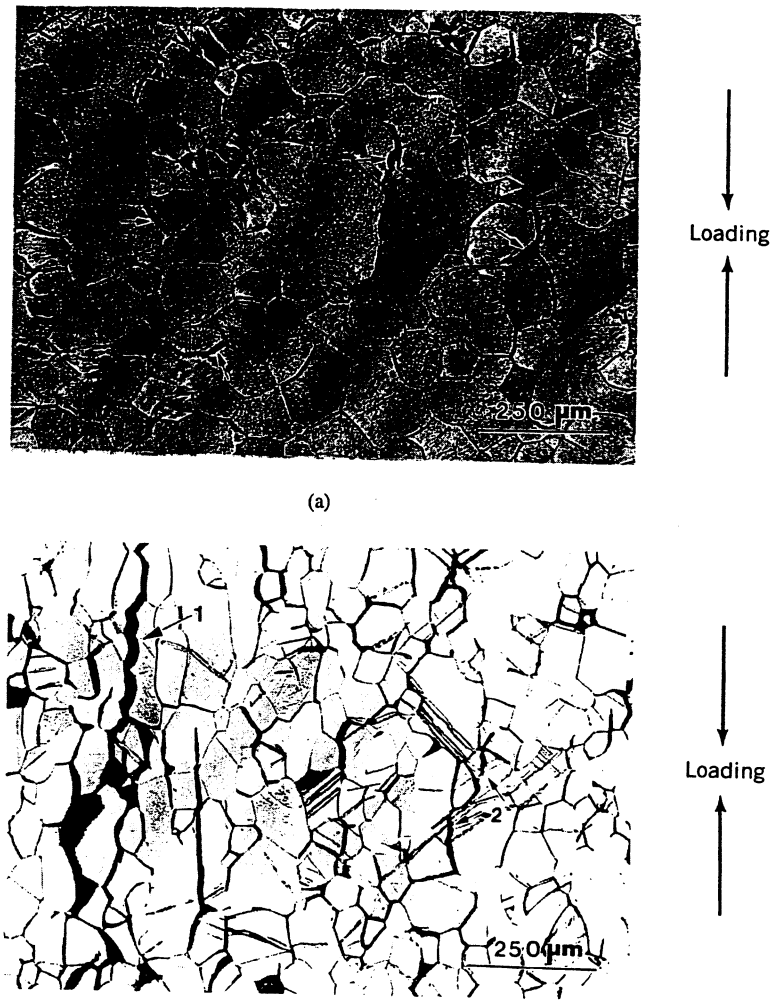

Figure 14.62 (*a*) Longitudinal section of W annealed at 2600°C, deformed to a strain of 25% ($\dot{\epsilon} = 10^{-3}\ s^{-1}$); (*b*) longitudinal section of annealed W at 2600°C, deformed to 5.2% ($\dot{\epsilon} = 4 \cdot 10^{3}\ s^{-1}$).

of the interfaces of this "sliding crack" created stress concentrations at its tips (marked by 3) producing tension at the points where these tips joined the grain boundaries that failed. It should be emphasized that the mechanism shown in Figure 14.64 is a departure from the classical "wing crack" model of Ashby and Hallam [143]. The directions of crack propagation are, in the present case, dictated by grain-boundary orientation and not, as in the former case, by the direction of the maximum principal stress. This will become evident when the

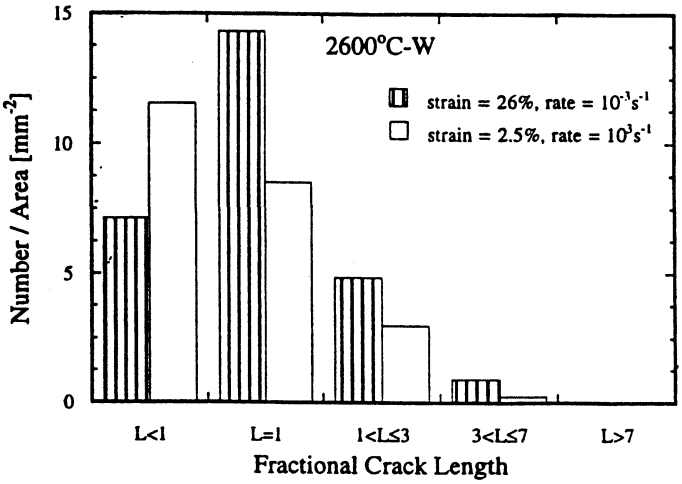

Figure 14.63 Damage in W annealed at 2600°C; showing a profound increase in damage, for increasing strain rates from 10^{-3} to 10^{3} s^{-1}. Note that strain at 10^{-3} s^{-1} is 26%, whereas at 10^{3} s^{-1}, it is equal to 2.5%. L is the size of a grain-boundary facet.

Ashby–Hallam equation is applied to the present case by setting the angle of crack propagation (ψ in Figure 14.65*a*) as the one for the grain boundaries, in an ideal arrangement.

Tension is necessary to initiate the vertical cracks perpendicular to the applied compressive load and gives rise to the mechanism that was first proposed by Griffith [163]. Due to the net shear stress sliding of the two crack surfaces

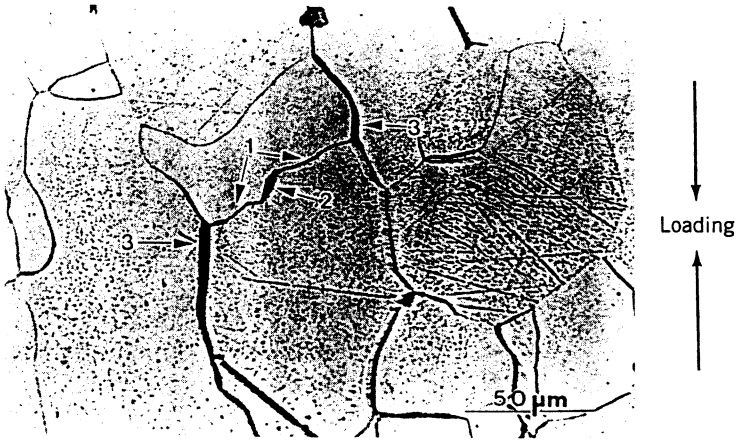

Figure 14.64 Intergranular cracks (3) that are produced by sliding of grain boundary (see offset 2).

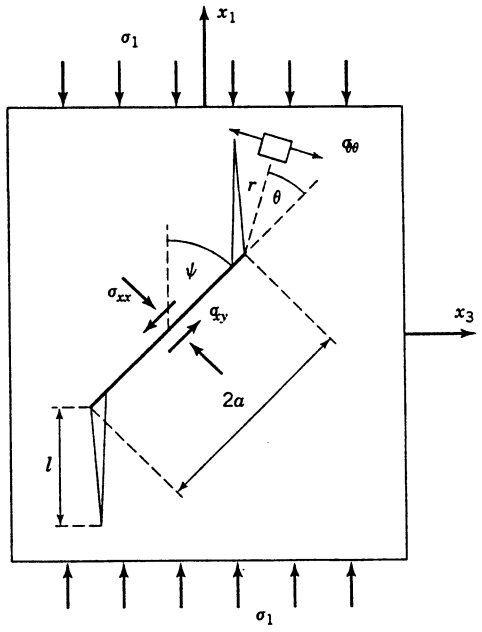

(*a*)

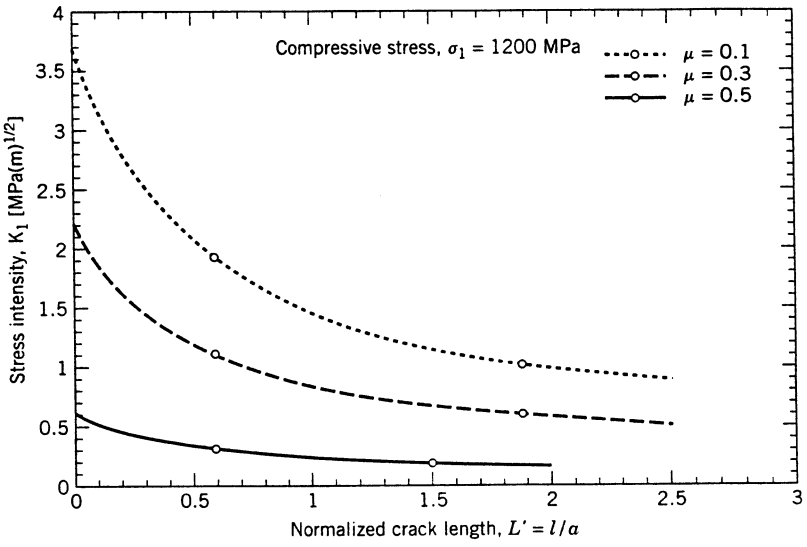

(*b*)

Figure 14.65 (*a*) Schematic of wing crack formation from the tips of a tilted sliding crack (*b*) K, acting at a wing crack tip vs. normalized crack length L', for friction coefficients μ = 0.1, 0.3, and 0.5.

will take place. This leads to a local tensile stresses at the tips of the microcrack that will, eventually, nucleate two wing cracks. The Ashby–Hallam [143] model describes the influence of the orientation (ψ) of the preexisting crack and its length 2a on the stress intensity factor K_I acting at the tip of a wing crack oriented at an angle θ to the sliding microcrack. In this model, the wing cracks are assumed to nucleate once the stress intensity factor at the tip reach its critical value, K_{Ic}. Figure 14.65*a* shows schematically how the wing cracks nucleate and grow from an initial sliding crack. Under uniaxial compressive loading and in the absence of a lateral stress (see Eq. (14.118)), the mode I stress intensity factor K_I acting at the tip of a wing crack can be written as,

$$K_I = \frac{2}{3}\sigma_1\sqrt{\pi a}\,[\mu(1-\cos 2\psi)-\sin 2\psi] \cdot \sin\theta\cos\frac{\theta}{2}\left\{\frac{\beta_n L' + (1+L')^{-1/2}}{(1+L')^{3/2}}\right\}. \tag{14.124}$$

where σ_1 = applied stress
μ = coefficient of sliding friction
L' = wing crack length
β_n = constant (= 0.4).

The frictional force due to the normal force (Coulomb friction) acting on the microcrack surfaces resists sliding and the resolved shear stress due to the external applied stresses acts as the driving force. The stress intensity factor K_I decreases with increasing wing crack length (l) suggesting stable crack growth with increasing load. The crack length 2a is taken to be 50 μm (equal to the grain facet size), and θ and ψ to be 60°. These angles are dictated by the geometry of the grain boundaries. The coefficient of friction μ for tungsten is taken to be 0.1, 0.3 and 0.5, which are typical sliding friction coefficients for hard metals. The values for 2a, ψ and θ were inserted into Eq. (14.24) to calculate the critical mode I stress intensity K_{Ic} at the tip of a representative sliding crack at crack initiation. Figure 14.65*b* shows the results for an applied compressive stress equal to 1,200 MPa. This is the stress at which microcracking by grain-boundary debonding starts. For $L' = 0$ (i.e., no preexisting cracks at flaw extremities) the value of K_{Ic} varies between 0.6 (μ = 0.5) and 3.7 MPa $m^{1/2}$ (μ = 0.1). The fracture toughness for the intergranular failure appears to be much smaller than transgranular failure in tungsten, typically 50 MPa $m^{1/2}$. This is due to grain boundary embrittlement.

Damage by nucleation wing cracks along the weak grain boundaries does not appear until the stress level reaches σ = 1,200 MPa. The quasi-static stress strain curve (Figure 14.66*a*) exhibits considerable hardening during early stages of deformation typical of annealed materials. Also, note that the material yields

around 0.75 GPa and does not develop damage until strains of approximately 0.25 and has hardened to stress level of 1.2 GPa. Beyond this stress level, the material fails by columnar splitting and microstructural characterization reveals that material fails by intergranular cracking (see Fig. 14.62). In the case of dynamic stress-strain response, it is seen that the material yields at around 1.2 GPa and material develops considerable damage even at very small strains of 0.02 (Fig. 14.62). This is readily verified by applying one of the constitutive equations presented in Section 14.3, Zerilli–Armstrong, MTS, or any equivalent model.

The experimental observations indicate that there are three competing deformation mechanisms in tungsten: slip, twinning, and grain-boundary decohesion. Due to the strain-rate sensitivity of the flow stress, twinning and grain-boundary decohesion are the favored mechanisms under high strain-rate conditions.

Under quasi-static loads the heat-treated tungsten exhibits a compressive strength of 0.75 GPa (Figure 14.66*a*). It is assumed that the grain boundary strength is strain-rate independent and approximately 1.2 GPa. Figure 14.66*a* shows these three effects in a schematic manner. The values σ_{ic} and σ_{fc} are the lower and upper boundary, respectively, which define a stress region in which damage is accumulated. At σ_{ic} damage initiates; at σ_{fc} the amount of damage reaches a level that leads to catastrophic failure of the specimen. Under quasi-static strain rates (10^{-3} s^{-1}), the level σ_{ic} is reached after plastic deformation to the strain of ϵ_{d1} (~15% in the present study). Up to this point the deformation is governed by plasticity. Under high strain rates (4×10^3 s^{-1}), the yield stress exceeds the stress level σ_{ic} thus, flow is initiated by damage initiation. Once the stress level σ_{fc} is exceeded the specimen fails catastrophically. The striking feature shown by Figure 14.66*a* is that increasing the strain rate reduces the strain at which damage is initiated from ϵ_{d1} to ϵ_{d2}.

The grain-size and strain-rate effects on the slip, twinning, and grain-boundary decohesion stresses render these three mechanisms competitive deformation mechanisms and affect significantly the material response. It is known that both the flow and twinning stress can be described by a Hall–Petch relationship as a function of grain size; this is seen in Section 14.4. Also, the grain-boundary decohesion stress decreases with grain size. Thus, the rates of change in slip, twinning, and grain-boundary cohesive stress with grain size dictate the actual deformation mechanism. The effect of grain size on the grain-boundary decohesion stress is due to the increase in impurity concentration (P, S, and O) at the grain boundaries. Due to the low solubility for interstitial atoms in tungsten, the total amount of embrittling grain boundary segregates is expected to be nearly the same in each heat treatment condition. The grain-boundary impurity concentration c_{GB} in mol/unit area then is inversely proportional to the grain boundary area per unit volume $A_V (A_V = 3/D)$. Thus,

$$c_{GB} = n \frac{D}{3} \tag{14.125}$$

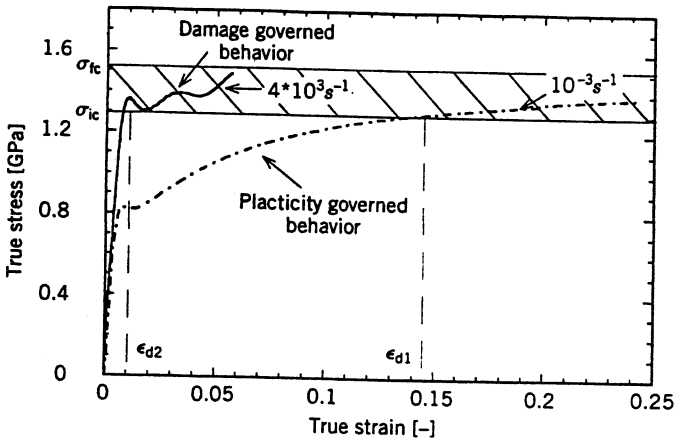

(a)

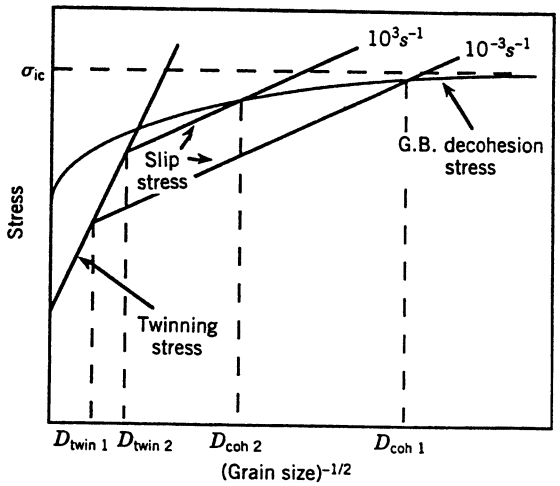

(b)

Figure 14.66 (*a*) Experimental compressive stress-strain curves at two different strain rates; σ_{ic} → initiation of damage; σ_{fc} → catastrophic failure of specimen; (*b*) schematic representation of different micromechanisms (slip, twinning and grain-boundary decohesion) as a junction of grain size and strain rate.

Where n is the impurity content in mol/unit volume and D is the grain size. A diminution in the grain-boundary decohesion stress $\Delta\sigma_{GB}(c_{GB})$ is caused by an increase in c_{GB}. For simplicity it is assumed that $\Delta\sigma_{GB}$ increases linearly with c_{GB}. The grain boundary decohesion stress σ_{GB} can be then described as:

$$\sigma_{GB} = \sigma_{ic} - \Delta\sigma_{GB}(c_{GB}) \qquad \text{and} \qquad \sigma_{GB} = \sigma_{ic} - \mathrm{k} \cdot D \tag{14.126}$$

Where σ_{ic} is the decohesion stress of a "clean boundary" and k is a constant. The slope k is given by the total amount of embrittling segregates and their embrittling activity. Figure 14.66*b* shows the grain-boundary decohesion stress σ_{GB}, the twinning stress and the slip stress in a common stress-versus-$D^{-1/2}$ plot. It is also well known that the strain-rate dependence for twinning is much less significant than for slip. Armstrong and Worthington [38] demonstrated that the Hall–Petch slope for twinning k_t is 2–5 times the Hall–Petch slope for slip in BCC metals. This leads to slip, twinning, and grain-boundary decohesion being competing mechanisms of flow/failure. In Figure 14.66*b* four transitions are marked by: $D_{\text{twin}\,1}$, $D_{\text{twin}\,2}$, $D_{\text{coh}\,1}$, and $D_{\text{coh}\,2}$. It is assumed for simplicity that grain-boundary decohesion and twinning are independent of strain rate. The strain-rate sensitivity of slip in BCC metals is schematically shown by the parallel lines at 10^{-3} and 10^{3} s^{-1}. Different regimes of response are obtained as a function of strain rate and grain size:

At $\dot{\epsilon} = 10^{-3}$ s^{-1} the deformation mechanism for grain sizes $D > D_{\text{twin}\,1}$ is twinning, for $D_{\text{coh}\,1} < D < D_{\text{twin}\,1}$ slip, and for grain sizes $D < D_{\text{coh}\,1}$ it is grain-boundary decohesion.

At $\dot{\epsilon} = 10^{3}$ s^{-1} twinning is the deformation mechanism for grain sizes $D > D_{\text{twin}\,2}$, slip for $D_{\text{coh}\,2} < D < D_{\text{twin}\,2}$, and grain-boundary decohesion for $D < D_{\text{coh}\,2}$.

There are complicating factors that affect this simple explanation; for example, twin-twin intersections lead to the initiation of transgranular fracture.

14.8 SUMMARY AND CONCLUSIONS

The observations reported in this chapter, as well as extensive information in the literature, indicate that microstructural aspects are of utmost importance in the dynamic deformation and failure of materials.

The mechanical models have progressed to the point where they incorporate the most important physical phenomena in dynamic deformation and failure. Advanced computational methods (especially finite elements, finite differences, and molecular dynamics codes) can capture the complex phenomenology of dynamic deformation and failure. In parallel, analytical, closed-form solutions have been developed for a large number of loading situations and microstructural configurations.

In dynamic deformation, dislocation and twinning dynamics can lead to realistic predictions of the plastic response of metals. In the shock-wave deformation regime, there still exists considerable uncertainty regarding the nature of the micromechanical processes due to the extreme difficulty of observation. The competition between slip and twinning is an important consideration in dynamic deformation.

Dynamic failure can be divided into three classes:

1. Dynamic failure by tension; spalling (uniaxial strain state) and uniaxial stress state.
2. Dynamic failure by shear; shear instability is the precursor to this failure mode.
3. Dynamic failure by compression; ceramics, rocks and brittle metals (cast iron, tungsten, intermetallic compounds) are especially prone to failure under compressive loading.

We summarize below the most important microstructural effects for these three classes of failure. All microstructural variables play a role in the dynamic failure of materials. The most important variables are

- Grain size
- Presence, density, morphology, and size and distribution of second-phase particles
- Texture (not mentioned in this chapter)
- Impurity atoms and their distribution (e.g., segregation at grain boundaries)
- Crystallographic structure (which can be changed by heat treatment, e.g., quenching of steel)
- Prestrain (e.g., annealed vs. shock-hardened material)
- Intergranular phases (e.g., glassy phase at grain boundaries of ceramic)
- Voids (e.g., porosity in the ceramics) and microcracks

We did not discuss in this chapter mechanochemical aspects, in which the interplay between chemistry and dynamic deformation can generate a surprising range of unexpected phenomena. Displacive phase transformations and exothermic chemical reactions are deeply affected by the stresses and strains and another chapter would be needed to discuss these effects.

A most important conclusion that can be derived, and is indeed illustrated, in this chapter is: The highly complex and varied microstructures observed in dynamic deformation and failure differ significantly from their quasi-static counterparts and are the result of competing deformation and failure processes that have different strain rate, stress state, and temperature sensitivities: slip, twinning, dynamic recrystallization, aging, displacive phase transformations, grain boundary decohesion, cleavage, void opening. These mechanisms compete; heat transfer and wave propagation also influence the sequence of processes.

ACKNOWLEDGMENTS

Many of the results presented here were obtained in research that was supported by the U.S. Army Research Office URI and MURI Programs, the National Science Foundation Grant MSS-9021671, The Office of

Naval Research (Contract N00014-96-1-0638), the Department of Energy (Grant DE-FG03-98DP00212), and the Center for Explosives Technology Research, New Mexico Tech. Collaborations and discussions with former students and colleagues, U. R. Andrade, R. W. Armstrong, D. J. Benson, S. N. Chang, H. C. Chen, Y. J. Chen, S. Christy, H. A. Grebe, J. Isaacs, B. Kad, L. H. L. Louro, F. Marquis, L. W. Meyer, A. Molinari, L. E. Murr, S. Nemat-Nasser, V. Nesterenko, G. Ravichandran, C. J. Shih, N. N. Thadhani, K. S. Vecchio, C. Wittman, T. W. Wright, and A. Zurek are greatly appreciated. Dr. Y. J. Chen made a number of plots and calculations presented here. Permission of G. Ravichandran to present unpublished joint work is gratefully acknowledged. Professor J. Wark, Oxford University, provided valuable assistance by patiently explaining to me the rudiments of statistical mechanics necessary to understand dislocation dynamics.

REFERENCES

1. H. Kolsky, *Stress Waves in Solids*, Dover, New York, 1963.
2. L. B. Freund, *Dynamic Fracture Mechanics*, Cambridge Univ. Press, Cambridge, U.K., 1990.
3. Y. Bai and B. Dodd, *Adiabatic Shear Localization*, Pergamon, Oxford, U.K., 1992.
4. M. A. Meyers, *Dynamic Behavior of Materials*, Wiley, New York, 1994.
5. U. F. Kocks, M. F. Ashby, and A. A. Argon, "Thermodynamics and Kinetics of Slip," *Prog. Mat. Sci.* **19** (1975), 1.
6. Y. J. Chen, F. Marquis, M. A. Meyers, and D. S. Kim, *Met. Trans.* **26A** (1995), 2493.
7. G. R. Johnson and W. H. Cook, *Proc. 7th Intl. Symp. Ballistics*, The Hague, Vol. 541, 1983.
8. M. A. Meyers, O. Subhash, B. K. Kad, and L. Prasad, *Mech. Mat.* **12** (1994), 175.
9. U. R. Andrade, M. A. Meyers, and A. H. Chokshi, *Scripta met. et mat.* **30** (1994), 933.
10. J. Litonsky, *Bull. Acad. Pol. Sci.* **25** (1977), 7.
11. R. W. Klopp, R. J. Clifton, and T. G. Shawki, *Mech. Mat.* **4** (1985), 375.
12. E. Orowan, "Dislocations and Mechanical Properties," in *Dislocations in Metals*, Vol. 103, AIME Monograph, New York, 1954.
13. F. J. Zerilli and R. W. Armstrong, *J. Appl. Phys.* **61** (1987), 1816.
14. J. R. Klepaczko, *Mat. Sci. Eng.* **18** (1975), 121.
15. (a) P. S. Follansbee and U. F. Kocks, *Acta Met.* **36** (1988), 81; (b) R. Becker, *Z. Physik*, **26** (1925), 919; (c) A. Seeger, *Z. Naturforsch.*, **9A** (1954), 758, 819, 856; (d) H. Conrad and H. Wiedersich, *Acta Met.* **8** (1960), 128.
16. W. G. Johnston and J. J. Gilman, *J. Appl. Phys.* **33** (1959), 129.
17. D. F. Stein and J. R. Low, Jr., *J. Appl. Phys.* **32** (1960), 362.
18. R. W. Rohde and C. H. Pitt, *J. Appl. Phys.* **38** (1967), 876.
19. J. J. Gilman, *Micromechanics of Flow in Solids*, McGraw-Hill, New York, 1969, p. 195.
20. L. W. Meyer, "Constitutive Equations at High Strain Rates," in *Shock-Wave and High-Strain Rate Phenomena in Materials*, M. A. Meyers, L. E. Murr, and K. P.

Staudhammer, eds., Marcel Dekker, New York, 1992, p. 49.
21. V. R. Parameswaran and J. Weertman, *Met. Trans.* **2** (1971), 1233.
22. J. Weertman, in *Response of Metals to High Velocity Deformation*, AIME Proc., P. G. Shewmon and V. F. Zackay, eds., Interscience, New York, 1961, p. 205.
23. F. J. Zerilli and R. W. Armstrong, *J. Appl. Phys.* **68** (1990), 1580; *Acta Met. Mat.* **40** (1992), 1803.
24. M. A. Meyers and K. K. Chawla, *Mechanical Behavior of Materials*, Prentice-Hall, Englewood Cliffs, NJ, 1998.
25. J. W. Christian and S. Mahajan, *Prog. Mat. Sci.* **39** (1995), 1–157.
26. R. E. Reed-Hill, J. P. Hirth, and H. C. Rogers, eds., *Deformation Twinning*, TMS-AIME Conf. Proc., Gordon and Breach, New York, 1965.
27. A. H. Cottrell and B. A. Bilby, *Phil. Mag.* **42** (1951), 573.
28. J. A. Venables, *Phil. Mag.* **6** (1961), 379.
29. R. F. Bunshah, cited in R. E. Reed-Hill, et al., [26], p. 390.
30. T. Takeuchi, *J. Phys. Soc. Jpn.* **21** (1996), 2616.
31. E. Hornbogen, *Trans. AIME* **221** (1961), 712.
32. J. B. Cohen and J. Weertman, *Acta Met.* **11** (1963) 997.
33. J. P. Hirth and J. Lothe, *Theory of Dislocations*, McGraw-Hill, New York, 1968, p. 364.
34. E. Orowan, *Dislocations in Metals*, AIME, New York, 1954, p. 116.
35. A. W. Sleeswyk, *Acta Met.* **10** (1962), 803.
36. S. Mahajan, *Acta Met.* **23** (1975), 671.
37. M. A. Meyers, O. Vöhringer, and Y. G. Chen, in "Advances in Twinning," *TMS-AIME*, 1999, p. 43.
38. R. W. Armstrong and P. J. Worthington, in *Metallurgical Effects at High Strain Rates*, R. W. Rohde, B. M. Butcher, J. R. Holland, and C. H. Karnes, eds., Plenum Press, New York, 1973, 401.
39. K. Ogawa, *Phil. Mag.* **29** (1965), 217–232.
40. J. Harding, *Mém. Sci. Rev. Métallurg.*, LXV, **15** (1968), 245–54.
41. O. Vöhringer, *Metall* **12** (1976), 1150.
42. D. Löhe and O. Vöhringer, *Z. Metallkunde* **77** (1980), 557.
43. M. J. Marcinkowski and H. A. Lipsitt, *Acta Met.* **10** (1962), 95.
44. M. A. Meyers and E. Ashworth, *Phil. Mag.* **46** (1982), 737.
45. M. A. Meyers, H. R. Andrade, and A. H. Chokshi, *Met. Mat. Trans.* **26A** (1995), 2881.
46. R. J. Clifton, *J. Appl. Mech.* **50** (1983) 941.
47. J. W. Swegle and D. E. Grady, *J. Appl. Phys.* **58** (1985), 602.
48. M. A. Meyers, *Scripta Met.* **12** (1978), 21.
49. M. A. Meyers, in *Strength of Metals and Allows*, P. Haason, V. Gerold, and G. Kostorz, eds., Pergamon Press, 1979, p. 547.
50. C. S. Smith, *Trans. AIME* **212** (1958), 574.
51. G. Ravichandran and M. A. Meyers, unpublished results, 1996.
52. B. L. Holian and P. S. Lomdahl, *Science* **280** (1998), 2085.
53. F. A. Bandak, R. W. Armstrong, and A. S. Douglas, *Phys. Rev. B* **46** (1992), 3228.
54. H. C. Rogers, *Annu. Rev. Mat. Sci.* **2** (1979), 283.
55. M. Stelly and R. Dormeval, in *Metallurgical Applications of Shock-Wave and High-Strain-Rate Phenomena*, L. E. Murr, K. P. Staudhammer, and M. A. Meyers, eds., Marcel Dekker, New York, 1986, p. 607.
56. R. Dormeval, in *Impact Loading and Dynamic Impact in Behavior of Materials*,

C. Y. Chiem, H. D. Kunze, and L. W. Meyer, Deutsche Gemanschaft fur Meta Informmationsgullschaft, 1988, p. 43.
57. R. W. Armstrong, R. Batra, M. A. Meyers, and T. W. Wright, *Mech. Mat.* **12** (1994), 83–328.
58. R. J. Clifton, *Material Response to Ultra-High Loading Rates*, Report No. NMAB-356, Natl. Materials Advisory Board, NAS, Washington, DC, 1979, Chapter 8.
59. Y. Bai, in *Shock Waves and High-Strain-Rate Phenomena in Metals: Concepts and Applications*, M. A. Meyers and L. E. Murr, eds., Plenum Press, New York, 1981, p. 277.
60. A. Molinari and R. J. Clifton, *C. R. Acad. Sci. Paris* **296** (1983), 1.
61. C. Fressengeas and A. J. Molinari, *Mech. Phys. Solids* **35** (1987), 185.
62. Y. M. Le Roy and A. J. Molinari, *Mech. Phys. Solids* **41** (1993), 631.
63. A. J. Molinari and Y. M. LeRoy, *C. R. Acad. Sci. Paris* **313** (1991), 7.
64. S. Kuriyama and M. A. Meyers, *Met. Trans.* **A1A** (1986), 443.
65. D. E. Grady, *Mech. Mat.* **17** (1994), 289.
66. R. W. Armstrong, C. S. Coffey, and W. L. Elban, *Acta Met.* **30** (1982), 2111.
67. J. Weertman and S. S. Hecker, *Mech. Mat.* **2** (1983), 89.
68. M. A. Meyers, K. C. Hsu, and K. Couch-Robino, *Mat. Sci. Eng.* **59** (1983), 235.
69. H. A. Grebe, H.-R. Pak, and M. A. Meyers, *Met. Trans.* **16A** (1985), 711.
70. C. L. Wittman, M. A. Meyers, and H.-R. Pak, *Met. Trans.* **21A** (1990), 707.
71. M. A. Meyers and C. L. Wittman, *Met. Trans.* **21A** (1990), 3193.
72. J. H. Beatty, L. W. Meyer, M. A. Meyers, and S. Nemat-Nasser, in *Shock Waves and High-Strain-Rate Phenomena in Metals*, M. A. Meyers, L. E. Murr, and K. P. Staudhammer, eds., Marcel Dekker, New York, 1992, p. 645.
73. M. Stelly, J. Le Grand, and R. Dormeval, in *Shock Waves and High-Strain-Rate Phenomena in Metals*, M. A. Meyers and L. E. Murr, eds., Plenum Press, New York, 1981, p. 113.
74. M. A. Meyers and H.-R. Pak, *Acta Met.* **34** (1986), 2493.
75. Y. Meunier, R. Roux, and J. Moureaud, in 72, p. 637.
76. U. R. Andrade, M. A. Meyers, K. S. Vecchio, and A. H. Chokshi, *Acta met. mat.* **42** (1994), 3183–3195.
77. B. Derby, *Acta met. mat.*, **39** (1991), 955.
78. S. Takeuchi and A. S. Argon, *J. Mat. Sci.* **11** (1976), 1547.
79. P. D. Tungatt and F. J. Humphrey, *Aca Met.* **32** (1976), 1547.
80. O. D. Sherby and P. M. Burke, *Prog. Mat. Sci.* **13** (1967), 325.
81. M. A. Meyers, J. C. LaSalvia, V. F. Nesterenko, Y. J. Chen, and B. Kad, in *Proc. ReX'96*, Monterey, CA, 1997, pp. 279–286.
82. D. Kuhlmann-Wilsdorf, *Met Trans.* **11A** (1985), 2091.
83. L. P. Kubin, *Phys. Stat. Solids* **135** (1993), 433.
84. D. E. Grady and M. E. Kipp, *J. Mech. Phys. Solids* **35** (1987), 95.
85. T. W. Wright and H. Ockendon, *Intl. J. Plast.* **12** (1996), 927.
86. A. Molinari, "Collective Behavior and Spacing of Adiabatic Shear Bands," *J. Mech. Phys. Solids* **45** (1997) 1551.
87. V. F. Nesterenko, M. A. Meyers, and T. W. Wright, in *Metallurgical and Materials Applications of Shock Wave and High-Strain-Rate Phenomena*, L. E. Murr, K. P. Staudhammer, and M. A. Meyers, eds., Elsevier, 1995, 397.
88. V. F. Nesterenko, M. A. Meyers, and T. W. Wright, *Acta Mat.* **46** (1998), 327.
89. N. F. Mott, *Engineering* **165** (1948).
90. H. Yoffé, *Phil Mag.* **42** (1951), 739.

91. K. B. Broberg, *Arch. Phys.* **18** (1960), 159.
92. J. W. Craggs, *J. Mech. Phys. Solids* **8** (1960), 66.
93. B. R. Baker, *J. Appl. Mech.* **22** (1962), 449.
94. J. D. Achenbach, "Dynamic Effects in Brittle Fracture," in *Mechanics Today*, S. Nemat-Nasser, ed., Vol. 1, Pergamon Press, New York, 1974, p. 1.
95. L. B. Freund, *J. Mech. Phys. Solids* **20** (1972), 129.
96. L. B. Freund, *J. Mech. Phys. Solids* **20** (1972), 141.
97. L. B. Freund, *J. Mech. Phys. Solids* **21** (1973), 47.
98. L. B. Freund, *Intl. J. Eng. Sci.* **12** (1974), 179.
99. L. B. Freund, "The Analysis of Elastic-Dynamic Crack Tip Stress Fields," in *Mechanics Today*, S. Nemat-Nasser, ed., Vol. 3, Pergamon Press, New York, 1976, p. 55.
100. L. B. Freund, *Dynamic Fracture Mechanics*, Cambridge Univ. Press, 1990.
101. J. Congleton, "Practical Applications of Crack-Branching Measurements," in *Dynamic Crack Propagation*, G. C. Sih, ed., Noordhof, Leyden, 1973, p. 427.
102. G. C. Sih, "Dynamic Aspects of Crack Propagation," in *Inelastic Behavior of Solids*, M. F. Kanninen, W. F. Adler, A. R. Rosenfield, and R. I. Jaffee, eds., McGraw-Hill, New York, 1970, p. 607.
103. G. Ravi-Chandar and W. G. Knauss, *Intl. J. Fract.* **26** (1984), 141.
104. S. Winkler, D. A. Shockey, and D. R. Curran, *Intl. J. Fract. Mech.* **6** (1970), 151.
105. F. A. McClintock, *J. Appl. Mech.* **35** (1968), 363.
106. F. A. McClintock, *Intl. J. Fract. Mech.* **4** (1968), 101.
107. J. R. Rice and D. M. Tracey, *Mech. Phys. Solids* **12** (1969), 201.
108. E. B. Glennie, *Mech. Phys. Solids* **2** (1972), 415.
109. J. R. Rice and M. A. Johnson, in *Inelastic Behavior of Solids*, M. F. Kanninen, W. F. Adler, A. R. Rosenfeld, and R. E. Jaffee, eds. McGraw-Hill, New York, 1970, p. 641.
110. R. M. McMeeking, *Trans. ASME, J. Eng. Mat. Techn.* **22** (1977), 290.
111. D. R. Curran, L. Seaman, and D. Shockey, in *Dynamic Failure of Solids, Phys. Rep.* 141 (1987), 253.
112. A. L. Gurson, *J. Eng. Mat. Technol.* **22** (1977), 2.
113. I. M. Fyfe, in *Material Behavior under High Stress and Ultrahigh and Ultrahigh Loading Rates*, J. Mescall and V. Weiss, eds., Plenum Press, New York, 1983, p. 309.
114. J. N. Johnson, *J. Appl. Phys.* **52** (1981), 2812.
115. M. M. Carroll and A. C. Holt, *J. Appl. Phys.* **43** (1972), 1626.
116. L. Davison and A. L. Stevens, *J. Appl. Phys.* **44** (1973), 688.
117. N. F. Mott, *Proc. Roy. Soc.* **A189** (1947), 300.
118. D. E. Grady and M. E. Kipp, *Intl. J. Rock Mech. Min. Sci.* **12** (1989) 147.
119. D. E. Grady, *J. Appl. Phys.* **55** (1982), 322.
120. F. Ke, Y. Bai, and M. Xia, *Sci. China* **33** (1990), 1447.
121. Y. Bai, F. Ke, and M. Xia, *Acta Mech. Sinica* **1** (1991), 59.
122. M. Xia, F. Ke, Y. Lu, and Y. Bai, *Sci. China* **34** (1991), 579.
123. L. H. L. Louro and M. A. Meyers, *J. Phys.* **42** (1988), C3–333.
124. L. H. L. Louro and M. A. Meyers, in *Shock Waves in Condensed Matter—1989*, S. C. Schmidt, J. N. Johnson, and L. W. Davidson, eds., North-Holland, Amsterdam, 1990, p. 465.
125. A. K. Zurek, P. S. Follansbee, and J. Hack, *Met. Trans.* **21A** (1990), 431.
126. M. A. Meyers and C. T. Aimone, *Prog. Mat. Sci.* **28** (1983), 1.

127. J. E. Field, *Investigation of the Impact Performance of Various Glass and Ceramic Systems*, Final Report, Contract DA, JA45-85-C-0221, Cavendish Laboratory, Cambridge, U.K., 1985; Q. Sun and J. Field, *Proc. Intl. Symp. Intense Dynamic Loading and Its Effects*, Chengdu, China, Sechuan Univ. Press, 1992, p. 384.
128. L. H. L. Louro and M. A. Meyers, *J. Mat. Sci.* **24** (1989), 971.
129. F. Longy and J. Cagnoux, *J. Am. Cer. Soc.* **L2** (1989), 971.
130. A. Cosculluela, J. Cagnoux, and F. Collombet, *J. Phys.* **IV** (1991), C3–109.
131. A. Cosculluela, Thesis, Univ. Bordeaux, 1992.
132. A. K. Zurek and P. S. Follansbee, in *Shock Compression of Condensed Matter—1989*, S. C. Schmidt, J. N. Johnson, and L. W. Davison, eds., North-Holland, Amsterdam, 1990, p. 433.
133. A. G. Ivanov and S. A. Novikov, *J. Exp. Theor. Phys.* (USSR) **40** (1961), 1880.
134. A. K. Zurek and M. A. Meyers, "Microstructure Aspects of Dynamic Failure," in *High-Pressure Shock Compression of Solids II*, L. Davison, D. E. Grady, and M. Shahinpoor, eds., Springer, 1996, pp. 25–70.
135. S. Christy, H.-R. Pak, and M. A. Meyers, in *Metallurgical Applications of Shock-Wave and High-Strain Rate Phenomena*, L. E. Murr, K. P. Staudhammer, and M. A. Meyers, eds., Marcel Dekker, New York, 1986, p. 835.
136. G. I. Kanel, S. V. Rasorenov, and V. E. Fortov, in *Shock-Wave and High-Strain-Rate Phenomena in Materials*, eds. M. A. Meyers, L. E. Murr, and K. P. Staudhammer, eds., Marcel Dekker, New York, 1992, p. 775.
137. D. J. Benson, *J. Mech. Phys. Solids* **41** (1993), 1285.
138. N. Goodier, *J. Appl. Mech.* **1** (1993), 39.
139. C. G. Sammis and M. F. Ashby, *Acta met.* **34** (1986), 511.
140. W. F. Brace and E. G. Bombolakis, *J. Geophys. Res.* **68** (1963), 3709.
141. M. Adams and O. Sines, *Tectonophysics* **42** (1978), 97.
142. H. Horii and S. Nemat-Nasser, *Trans. Roy. Soc. Lond.* **319** (1986), 33.
143. M. F. Ashby and S. D. Hallam, *Acta met.* **34** (1986), 497.
144. S. Nemat-Nasser and H. Deng, *Acta met. mat.* **42** (1994), 1013.
145. G. Ravichandran and G. Subhash, *Intl. J. Solids Struct.* **32** (1995), 2627.
146. J. Lankford, *J. Mat. Sci.* **12** (1977), 791.
147. J. D. Eshelby, F. C. Frank, and F. R. N. Nabarro, *Phil. Mag.* **42** (1951), 351.
148. A. N. Stroh, *Proc. Roy. Soc. Lond.* **A223** (1954), 404.
149. D. E. Grady, *J. Appl. Phys.* **53** (1982), 322.
150. C. T. Aimone, M. A. Meyers, and N. Mojtabai, in *Rock Mechanics in Productivity and Production*, C. H. Dowding and M. M. Singh, eds., AIME, 1984, p. 979.
151. G. I. Kanel, S. V. Rasorenov, and V. E. Fortov, in *Shock Compression of Condensed Matter*, S. C. Schmidt et al., eds., Elsevier, 1992, p. 541.
152. G. Raiser and R. J. Clifton, in *High-Pressure Science and Technology:* 1993, APS, 1994, p. 1039.
153. G. Raiser, J. J. Wise, R. J. Cliford, D. E. Grady, and D. E. Cox, *J. Appl. Phys.* **75** (1994), 3862.
154. R. J. Clifton, *Appl. Mech. Rev.* **48** (1993), 540.
155. H. Senf and E. Strassburger, Ernst-Mach Institute, private communication, 1994.
156. O. R. Johnson and T. J. Holmquist, in source cited in ref. 136, p. 1075.
157. J. Harding, in source cited in ref. 136, p. 21.
158. A. S. Argon, "Fracture of Composites," in *Treatise of Materials Science and Technology*, Academic Press, New York, 1972, p. 79.
159. A. G. Evans and W. F. Adler, *Acta Metallurgica* **26** (1977), 725.

160. N. A. Fleck, L. Deng, and B. Budiansky, *J. of Appl. Mech.* **62** (1995), 329.
161. R. Menig, M. H. Meyers, M. A. Meyers, and K. S. Vecchio, *Acta mat.* submitted (1999).
162. T. Dümmer, J. C. Lasalvia, G. Ravichandran, and M. A. Meyers, *Acta mat.* 17 (1998), 6267.
163. A. A. Griffith, *Proc. 1st Int. Congr. Appl. Mech.*, Delft, 1924, p. 55.
164. A. Seeger, *Phil. Mag.* **1** (1956) 651.
165. A. Seeger and P. Schiller, *Acta Met.* **10** (1962), 348.
166. K. Ono, *J. Appl. Phys.* **39** (1968) 1803.
167. F. C. Frank, *Proc. Phys. Soc.* **62A** (1949), 131.
168. O. Vöhringer, *Metall.* **11** (1972), 1119.
169. S. G. Song and G. T. Gray III, *Met. and Mat. Trans.* **26A** (1995), 2665.
170. J. Weertman and J. R. Weertman, in *Dislocations in Solids*, Vol. 3, F. R. N. Nabarro, ed., Elsevier/North Holland, NY, 1979, p. 1.